The effects of plasma and nuclear friction on heavy-ion fusion: an open quantum system perspective

I.G. Lee

Submitted for the Degree of
Doctor of Philosophy
from the
University of Surrey

Theoretical Nuclear Physics Group
Faculty of Engineering and Physical Sciences
University of Surrey
Guildford, Surrey GU2 7XH, U.K.

September 2023

Declaration

This thesis and the work to which it refers are the results of my own efforts. Any ideas, data, images or text resulting from the work of others (whether published or unpublished, and including any content generated by a deep learning/artificial intelligence tool) are fully identified as such within the work and attributed to their originator in the text, bibliography or in footnotes. This thesis has not been submitted in whole or in part for any other academic degree or professional qualification. I agree that the University has the right to submit my work to the plagiarism detection service TurnitinUK for originality checks. Whether or not drafts have been so-assessed, the University reserves the right to require an electronic version of the final document (as submitted) for assessment as above.

Iain Lee

September 15, 2023

Abstract

This thesis contains the theoretical work produced to achieve three goals. Firstly, by understanding the basics of density matrices and open quantum systems, the intricacies of the equations of motion could be understood and a new, key feature, the window operator, could be added to the coupled-channel density-matrix (CCDM) model. From this, the addition of quantum observable calculations such as entropy, energy dissipation and purity were made possible, but more importantly this permitted the calculation of energy-resolved fusion probabilities that were previously unobtainable with this fully quantum dynamical method.

The next step was motivated by the curiosity of heavy-ion fusion in hot, dense plasmas. A review of the potential effects of plasma on heavy-ion fusion reactions was conducted, and significant results were found for one attribute of the plasma: temperature. It is known that the higher-end of plasma temperatures in stellar environments become hot enough that heavy-ions with low-lying excited states are significantly populated prior to a nuclear reaction. However, this has not been applied to nuclear fusion and hence the CCDM model was employed to fill this void. Temperature was found to increase fusion probabilities compared to calculations that did not include temperature effects, and a short theoretical explanation of the increase was provided.

Finally, the CCDM model was applied in the context of nuclear friction. Using an adjusted phenomenological friction form factor introduced by Gross and Kalinowski, the effects of friction were included as an environment. The inclusion of friction resulted in increased fusion probabilities compared to frictionless calculations, and an improvement on the barrier distribution when comparing theory to experimental results.

Key words: Coupled-channels density-matrix, open quantum systems, sub-barrier nuclear fusion, quantum tunnelling, Lindblad dynamics, plasma environment, nuclear friction

Email: i.lee@surrey.ac.uk

Acknowledgements

I have had the privilege of meeting many people throughout my time at Surrey, and every experience has led me to my current pinnacle of academic achievement. In particular, I would like to thank my primary supervisor, Dr. Alexis Diaz-Torres for his support, wisdom and guidance. This project and its outcomes would be impossible without his expertise and patience. I thank my co-supervisor Prof. Paul Stevenson for his helpful insights and assistance throughout the PhD, in addition to the Theoretical Nuclear Physics research group for allowing me to discuss and explore ideas with like-minded people. I would like to acknowledge Dr. Gilbert Gosselin, for providing essential calculations and useful comments, and my viva supervisors, Dr. Daniel Doherty and Prof. Pierre Capel for their insightful questions and guidance.

The encouragement and support from Rachel Howard was more than I could have asked for, and I appreciate my housemates Max, Sean, Katherine and Billy for making the PhD not only bearable, but enjoyable. Acknowledgements must go to the administrative support team in the physics department for assisting with travel, conferences, opportunities and generally making life much easier. I thank the Leverhulme Trust for financial support (RPG-2019-325) and entrusting me to conduct this research.

Lastly I thank my mum and my sisters for being supportive throughout my life, and their confidence in me to take on difficult challenges such as this PhD. Thank you for everything.

Contents

Acronyms

BD	barrier distribution.
CCDM	coupled-channels density-matrix.
DICs	deep inelastic collisions.
DNS	dinuclear system.
EOM	equations of motion.
FFT	fast Fourier transform.
GDR	giant dipole resonance.
GK	Gross-Kalinowski.
HEDP	high energy density plasma.
LvN	Liouville-von Neumann.
MNT	multinucleon transfer.
NEEC	nuclear excitation by electron capture.
NEET	nuclear excitation by electron transition.
NPIs	nuclear plasma interactions.
TDCCWP	time-dependent coupled-channels wave packet.
TDHF	time-dependent Hartree-Fock.

TDSE	time-dependent Schrödinger equation.
TDWP	time-dependent wavepacket.
TISE	time-independent Schrödinger equation.

Chapter 1

Introduction

Nuclear fusion is considered one of the most important reaction mechanisms for stellar evolution and the production of heavy elements in the Universe. The idea that nuclear fusion was the source of power within stars was conceptualised by Eddington in the 1920's [1], following the discovery by Aston that the mass equivalent of four hydrogen atoms was heavier than one helium atom. With the theory of quantum mechanics being formalised around this time, researchers were quick to test this theory and it was Hund [2] who was credited as the first to apply 'penetration through a potential barrier' principles to molecular dynamics. The generalised mathematical theory of quantum tunneling was then developed by Gamow [3,4] and then independently and almost simultaneously by Gurney and Condon. The work by Bethe [5] was instrumental for establishing a cascade of reactions that lead to energy generation within stars, which is now known as Branch II of the proton-proton chain reaction. This paved the way for further stellar nucleosynthesis research [6].

To this day, much effort has been invested experimentally and theoretically to eventually gain a complete picture of stellar nucleosynthesis [7–10]. Nucleon interactions are fundamental for building theoretical frameworks and developing new experimental methods, both of which are essential for pushing the boundaries of research. This thesis aims to extend our theoretical knowledge of low-energy heavy-ion fusion reactions. The following sections provide a succinct historic review of the developments within heavy-ion fusion models, and the extension to literature from this work.

1.1 The one dimensional single barrier penetration model

If one considers only the most fundamental interactions between two nuclei, nuclear fusion calculations using simple models can be done using a real one dimensional potential barrier formed from *attractive* nuclear and *repulsive* Coulomb interactions [11]. The single dimension here is the distance between the centre of mass of each nucleus. The one dimensional potential barrier is the Coulomb barrier when the angular momentum $l = 0$, and one can assume that a nucleus fuses once it overcomes or tunnels through the Coulomb barrier and the loss of kinetic energy means it cannot escape the potential well. However, there is a limit to this assumption due to the strong repulsive Coulomb force when Z_1Z_2 increases, which leads to a shallow potential pocket that is easily escapable [12]. Quantum tunneling is the key mechanism that allows the fusion of nuclei at stellar energies [11, 12], and it is a relatively poorly understood phenomenon that is crucial in the study of low-energy nuclear fusion reactions [13]. For fusion to occur, the Coulomb barrier between a projectile and target must be overcome classically or 'tunnelled through'. Using purely classical mechanics, fusion would not occur for any incoming particle with an energy below the Coulomb barrier energy, V_B. Low-energy fusion reactions occur at energies well-below the height of the Coulomb barrier and as a result, the cross sections are often too small to be experimentally measured directly and models are needed to extrapolate the data [14].

Within the one dimensional single barrier potential models, the fusion cross section $\sigma(E_0)$ with a mean centre of mass energy E_0 can be calculated as a sum of partial waves [15],

$$\sigma(E_0) = \frac{\pi\hbar^2}{2\mu E_0} \sum_{l=0}^{\infty} (2l+1)\, T_l(E_0), \tag{1.1}$$

where μ is the reduced mass of the two-nuclei system, l is the partial wave number (angular momentum contributions) and T_l is the barrier penetration probability.

The early calculations of fusion cross sections were often based on classical mechanics, and semi-classical models became popular as quantum mechanics was better understood. A semi-classical model is a model where the system is treated with both classical and quantum mechanics, and these were used to reduce computationally intensive calculations but still include features of quantum mechanics. Hence early models were able to calculate below-barrier fusion cross sections by including quantum tunneling effects into classical calculations.

A common method was to use transport equations, and these assume that the important characteristics of dynamic fusion processes can be described by the main collective degrees of freedom. Typical equations that were used in models include Fokker-Planck, Langevin and master equations [16–19]. Classical microscopic methods such as time-dependent Hartree-Fock (TDHF) have also been used to investigate interactions between heavy nuclei, with some of these applied to fusion reactions [20–22]. However, the use of TDHF models was limited due to the significant computational resources required [23].

1.2 Building on the one dimensional single barrier penetration model

Comparison of experimental results to those of the single barrier penetration model using only the entrance (ground state) channel showed that the model calculations of fusion cross section agreed sufficiently with above-barrier incident energies, but found that the sub-barrier calculations were lower than the empirical fusion cross sections [24]. In general the discrepancy was minimal for light nuclei ($Z_1 Z_2 < 250$) collisions, and increased to a few orders of magnitude for medium-sized nuclei with a charge product of $250 < Z_1 Z_2 < 1600$. Above $Z_1 Z_2 > 1600$, the formation of a compound nucleus after the reduced mass traverses the Coulomb barrier (the capture process) is not guaranteed and additional considerations must be made [11, 12, 15]. These are problems that are faced by those interested in superheavy element formation.

The work in this thesis is focused on medium-sized nuclei. It was not immediately clear why there was an enhancement of fusion cross section at below-barrier energies for these medium-sized nuclei, but experimental results highlighted the internal structure as the cause of the enhancement [25]. This led to the development of coupled-channels formalisms, the details and assumptions of which can be found in Refs. [26–28]. The two intrinsic degrees of freedom which primarily influence fusion cross sections are deformations of the target and projectile (rotational) and low-lying collective excitations (related to surface vibrations).

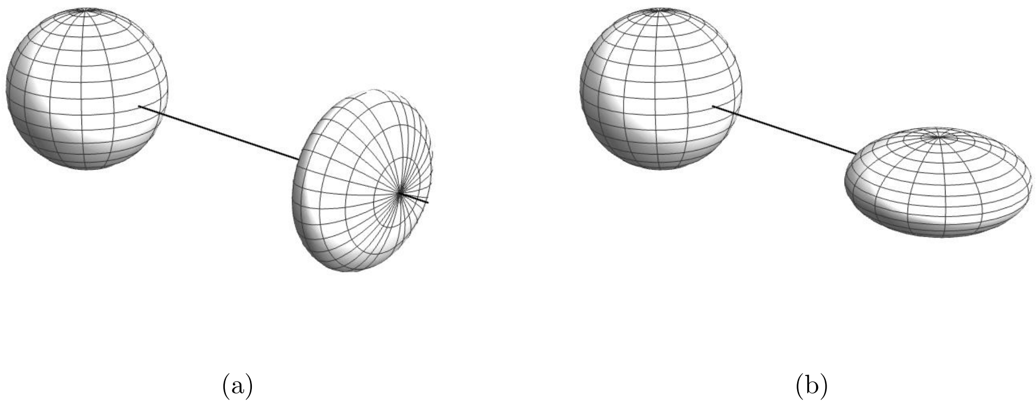
(a) (b)

Figure 1.1: A visual representation of a spherical projectile approaching a deformed nucleus at two orientations. In Fig.1.1a, the projectile approaches the shortest diameter of the deformed target. Fig.1.1b shows the projectile approach the largest diameter of the deformed target.

Both of these intrinsic degrees of freedom can be implemented in the calculations in this work, and this is demonstrated in the present work by the excited states in the targets of ^{144}Sm, ^{188}Os and ^{92}Zr. To visualise the effect of these intrinsic degrees of freedom, Fig.1.1 shows a spherical projectile approaching a rotationally deformed target nucleus at two orientations. It is expected that the resulting nuclear and Coulomb forces between the target and projectile for both cases would be different to that of two spherical nuclei.

By coupling the nuclear intrinsic degrees of freedom to the relative motion, the coupled-channels equations can be numerically solved to determine the fusion cross sections of the reduced system [11,12,29]. The coupled-channels equations have typically been constructed based on a stationary time-independent Schrödinger equation (TISE), which can be solved to provide fusion cross sections for couplings to all orders for a relatively large number of channels. The coupled-channels equations are given as [15,26],

$$\left[-\frac{\hbar^2}{2\mu}\frac{d^2}{dr^2}+\frac{J(J+1)\hbar^2}{2\mu r^2}+V_N^{(0)}(r)+\frac{Z_P Z_T e^2}{r}+\epsilon_n-E_{c.m}\right]\psi_n(r)+\sum_m V_{nm}(r)\psi_m(r)=0, \tag{1.2}$$

where r is the radial co-ordinate of the relative motion, μ is the reduced mass, $E_{c.m}$ is the total energy in the centre of mass reference frame and ϵ_n is the n$^{\text{th}}$ channel excitation energy.

$V_N^{(0)}(r)$ is the nuclear potential in the entrance channel where the superscript denotes the multipolarity ($0 =$ monopole), and $V_{nm}(r)$ is the coupling matrix consisting of Coulomb and nuclear components, where the higher order multipole information is contained. For heavy-ion reactions, the isocentrifugal approximation was shown to be valid for fusion reactions [30] and hence the orbital angular momentum usually present in Eq.(1.2) is replaced with the total angular momentum quantum number, J.

A user-friendly implementation of the coupled-channels equations was created by Hagino [31] and this led to the widespread use of the `CCFULL` code since its conception. Calculations from `CCFULL` are used to verify that the results from this thesis are in agreement with current literature for standard calculations that do not include novel effects, such as the effects from plasma temperature or nuclear friction. Further details on the coupled-channels TISE and the `CCFULL` code can be found in Ref. [31].

It is worth mentioning that the motivation to improve theoretical heavy-ion fusion models has been greatly influenced by research on the production of superheavy nuclei. The coupled-channels approaches have been key to modelling superheavy element formation, and have improved our knowledge on how couplings between nuclear intrinsic degrees of freedom and relative motion affect capture cross sections [32–34]. However, when dealing with heavy nuclear systems, there are additional considerations that must be included due to processes that occur when nuclei become large and the repulsive Coulomb force increases significantly, such as quasi-fission, fusion-fission and deep inelastic collisions (Fig. 1.2). The assumption that nucleons immediately form a singular compound nucleus once reaching a critical distance is no longer valid, and other reaction outcomes may occur instead. Models based on a dinuclear system (DNS) [35,36] were developed as an alternative way of describing the fusion mechanism. The DNS treats fusion as a nucleon transfer process between two touching nuclei, and uses mass (charge) asymmetry, neck formation and deformation factors as parameters in the calculations. It was found to agree well with experimental results for both cold and hot fusion reactions* [37].

A step toward the use of fully quantum dynamical models was the time-dependent coupled-channels wave packet (TDCCWP) [38]. This method combines the time-dependent wavepacket

---

*Cold and hot fusion reactions refer to the formation of a compound nucleus with energies of between $10-20$ MeV and $40-50$ MeV respectively.

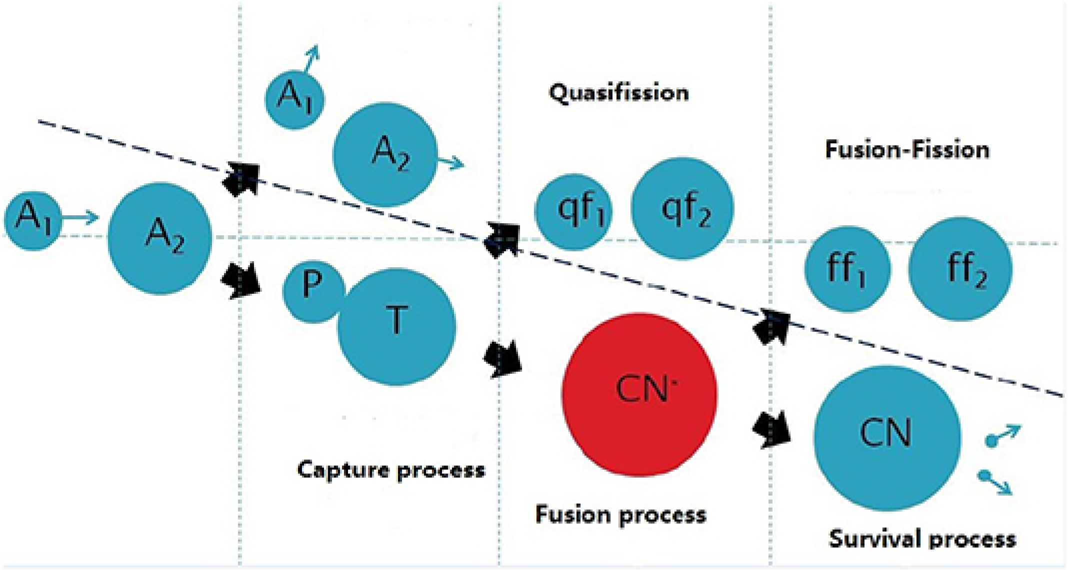

Figure 1.2: A schematic figure showing various outcomes of heavy-ion collisions. Figure from [37].

(TDWP) approach with the previously mentioned coupled-channels equations, and allows for the quantum treatment of radial motion and coupled the radial motion to intrinsic excited states. The TDCCWP was shown to calculate transmission coefficients in agreement with TISE calculations for a wide range of energies and angular momenta. However, in order to include environmental effects, this method would be difficult to use since there is no intuitive method to include decoherence since a wave function can only describe pure states.

1.3 The proposed development for heavy-ion fusion reactions

Constant advancements in technology have created an abundance of viable techniques that can be exploited for the modelling of increasingly specific mechanisms using the open quantum system approach [39–42]. Figure 1.3 gives a visual representation of the open quantum system, and more details are given in Section 2.2. Choosing the correct implementation is important to balance the amount of useful and accurate information produced from the model, the complexity of calculations and computational run time.

The technique used in this thesis is the coupled-channels density-matrix (CCDM) method

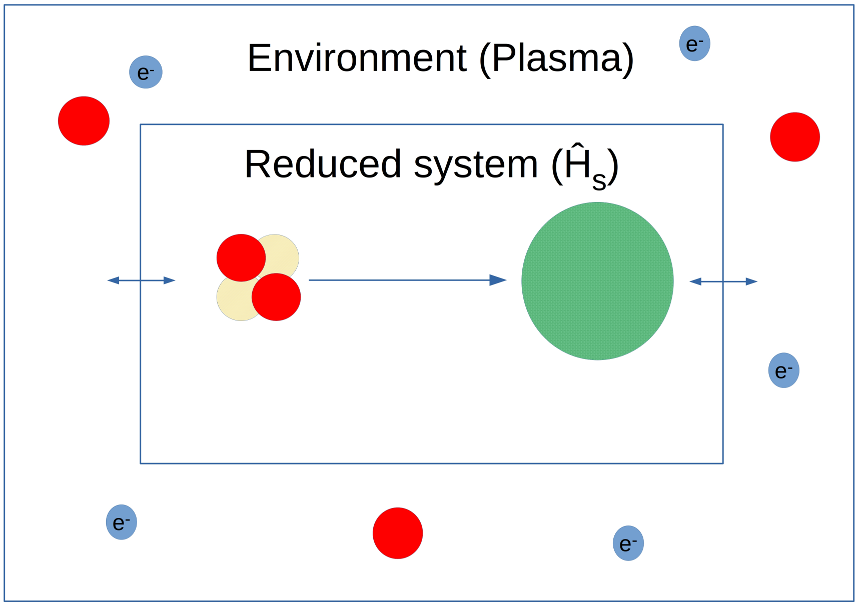

Figure 1.3: A graphic of an open quantum system. The reduced system contains the nondissipative dynamics whereas the environment is related to the dissipative dynamics. Note that this method is not restricted to a singular environment and many more can be included subject to numerical restrictions.

[43–45], using the Markovian Liouville-von Neumann (LvN) equation with Lindblad dynamics describing the dissipation to the environment. The LvN equation has been widely discussed and applied in quantum molecular dynamics [46–49] and the generality of its application allows for its rich literature to be used in this interdisciplinary physics research. The first uses of this method in the nuclear scale involved an investigation into dissipative quantum dynamics and the effects of quantum decoherence on reaction observables [50,51]. This was motivated by fusion measurements that did not agree with coherent coupled-channels approach calculations [52].

In the context of nuclear reactions, the CCDM method considers the excitation of both the projectile and target nuclei on a radial grid. A wave packet represents a distribution of incident energies for the projectile-target radial motion, which allows one to use a finite radial grid for computational simulations. The propagation in time is approximated using Faber polynomials [53], a polynomial expansion technique that significantly improves the computational run time compared to directly solving the LvN equation. This method preserves the trace of the density matrix and allows the observation of the interactions before, during and after fusion. The use of a dynamic approach, based on the LvN equation and using the CCDM, offers a range of additional information that could not be obtained before. For example, this method gives the ability to follow the time propagation and observe the density of probability at any time step, which is useful for visualisation and analysis of the dynamics.

The present work concerns new developments in heavy-ion fusion reaction theory. This involves the use of the aforementioned method to implement effects on heavy-ion fusion due to a surrounding environment, or due to couplings to the internal structure of the colliding nuclei (non-collective excitations). To do this, we first apply a test case nucleus that is well-studied and compare the CCDM method to TISE calculations. Then the path is clear to begin studying environmental effects. The ability to include these effects as part of the open quantum system formalism is the main improvement of our dynamic approach over the stationary approach. The report structure below gives a brief insight into each chapter within this thesis and chronologically describes the journey of this research project.

1.4 Report structure

The report is structured as follows. Chapter 2 introduces some relevant theoretical background including the construction of the initial density matrix and the equations of motion. In Chapter 3, the numerical methods are explained along with a short literature review of other methods that address similar problems. The coupled-channels density-matrix approach that is used throughout this thesis is described in detail in Chapter 4. Chapter 5 provides information on the window operator and how it is used to provide accurate energy-resolved fusion probabilites. Chapter 6 shows the model validation results of the $^{16}\mathrm{O}+{}^{144}\mathrm{Sm}$ collision and gives details of techniques used to enhance the model calculations. Chapter 7 describes the study of plasma effects on heavy-ion fusion reactions. Chapters 6 and 7 are extensions to a research letter and article, published by the author in the journals Physics Letters B and Physical Review C respectively [54,55]. Chapter 8 presents the background and results of the effect of nuclear friction on heavy-ion fusion. Conclusions and further work are given in Chapter 9.

Chapter 2

Theoretical Background

2.1 Basic density matrix theory

Nuclear physics has been described both classically and within the theory of quantum mechanics depending on the observable of interest. Observations of macroscopic interactions described using classical mechanics have been instrumental in the development of nuclear physics, famous examples being the discovery of Rutherford scattering by Rutherford, Geiger and Marsden [56, 57] and Bohr's theory of nuclear fission based on the liquid drop model [58]. The application of quantum mechanics to nuclear physics allowed refinements in calculations, so that individual nucleus interactions with a physical system could be described by a state vector, $|\psi\rangle$, for calculations where a pure state has been prepared [59],

$$|\psi\rangle = \sum_n c_n |v_n\rangle , \tag{2.1}$$

where c_n are complex coefficients and $|v_n\rangle$ are the eigenvectors of a particular operator, such as the Hamiltonian operator. Then the pure state density matrix is defined as

$$\rho_{\text{pure}} = |\psi\rangle \langle\psi| , \tag{2.2}$$

and the mean value of an operator $\hat{A}$ in matrix form $A_{mn} = \langle v_m| \hat{A} |v_n\rangle$, for a system in a pure state described above is given by,

$$\langle\hat{A}\rangle = \sum_{mn} A_{mn}\, c_m^* c_n. \tag{2.3}$$

In quantum mechanics, systems are often simplified and pure states are used to describe physical interactions. However, it is unlikely that a superposition of coherent pure states exists in nature due to the presence of environments that cause decoherence and dissipation [60]. Mixed states are used when we do not have the exact information on the quantum system and can be mathematically described using a density matrix.

The mean value of $\hat{A}$ for an incoherent superposition of many pure states $\psi^{(i)}$ can be described by statistical weights $p^{(i)}$ multiplied by the expected value of the operator for each pure state $\langle\hat{A}\rangle_i$ [61],

$$\langle\hat{A}\rangle = \sum_i p^{(i)} \langle A\rangle_i = \sum_{nm} A_{mn} \sum_i p^{(i)} c_m^{*(i)} c_n^{(i)}. \tag{2.4}$$

The mixed state density matrix can then be written as a weighted sum with $\sum_i p^{(i)} = 1$, of pure state density matrices,

$$\rho_{nm} \; = \sum_i p^{(i)} \left|\psi_n^{(i)}\right\rangle \left\langle\psi_m^{(i)}\right| \; = \sum_i p^{(i)} c_m^{*(i)} c_n^{(i)}, \tag{2.5}$$

and hence

$$\langle\hat{A}\rangle = \sum_{mn} A_{mn}\rho_{nm} = \mathrm{Tr}(\hat{A}\hat{\rho}), \tag{2.6}$$

since the trace of $\mathrm{Tr}(\hat{A}\hat{\rho})$ is the sum of the diagonal elements of the matrix $\hat{A}\hat{\rho}$. The concept of a density matrix can be used to describe the state of a quantum system in any circumstance, from a pure, coherent scenario to a mixed, incoherent scenario. It is the most general mathematical object to describe any quantum state. To quantify how mixed a state is, the purity $\mathcal{P}$ and von Neumann entropy S_{vn} are used and are given below,

$$\mathcal{P} = \mathrm{Tr}[\hat{\rho}^2], \tag{2.7}$$

$$S_{vn} = -\mathrm{Tr}[\hat{\rho}\ln(\hat{\rho})], \tag{2.8}$$

and for pure states $\mathcal{P} = 1$ and $S_{vn} = 0$. These quantities are useful for numerically describing the decoherence within an open system and the irreversibility due to energy dissipation to an environment. Further information on purity and entropy is provided later in this work.

2.2 Open quantum systems

An open quantum system is a quantum system that is coupled to an environment that may also be another quantum system. In a reduced density matrix, the full system is usually separated into two parts: the reduced system $\mathcal{S}$ and the environment[*] $\mathcal{B}$. The reduced system is the primary system of interest that may change from internal dynamics or interactions with the environment. Then the total, global Hamiltonian consists of 3 terms [62]

$$H = H_{\mathcal{S}} + H_{\mathcal{B}} + H_{\mathcal{I}}, \tag{2.9}$$

where $H_{\mathcal{I}}$ denotes the interaction Hamiltonian between the system and bath. The combined system and bath ($\mathcal{S} + \mathcal{B}$) is considered a closed system and follows unitary Hamiltonian dynamics [60], since we assume any further interactions, for example interactions of the environment with the environment's surroundings, are negligible. However, the state of the reduced system can be influenced by the interactions with its environment(s), and these system-environment interactions can lead to non-unitary Hamiltonian dynamics. In this work, a phenomenologically determined Hamiltonian is used and is described in Section 4.2. This is necessary due to the absence of a fully described microscopic model[†], which would have its own limitations due to memory and computational run time. In fact, the

---

[*] The environment can also be called a reservoir or heat bath depending on the thermal equilibrium conditions.

[†] The model being fully described by quantum mechanics.

main reason open quantum systems are used is due to the complications involved with creating a complete mathematical model for combined system dynamics.

In an open quantum system, the presence of an environment creates correlations between the states of the system and the states of the environment. This creates a statistical mixture of eigenstates from the initial coherent or partially coherent quantum state, which mathematically can be used to determine the degree of decoherence in the measured system, using Eq.(2.7) for example. The environment can also be thought as a quantum probe which performs an indirect measurement on the open system, causing the deterioration of superpositions of some states within the system, destroying quantum coherences [63]. There are still many answers to be found regarding decoherence, such as its role in determining the boundary between classical and quantum mechanics. The use of environment states provides the model with a method of removing probability from the density matrix, and therefore it is possible to make correlations between physical observables and decoherence.

The inclusion of an open quantum system environment is the primary improvement over previously conducted research. To demonstrate the capability of this method, a ‘fusion’ environment is used for describing dissipation to an environment using an open quantum systems approach. When nuclear fusion occurs, the newly formed compound nucleus has complex states that causes a loss of flux from the reduced system, in the form of energy and radial probability density. Hence the fusion environment is not a physical environment, but it is modelled as an environment to allow the measurement of the flux lost due to nuclear fusion, throughout the time propagation. This technique is used further for treating nuclear friction as an environment in the model. The nuclear friction environment represents the energy dissipation from the reduced system that could occur as a result of radially-induced non-collective excitations. More information about the friction environment is given in Chapter 8.

2.3 Equations to describe dissipation

To describe dissipation, quantum mechanical semigroups were introduced with the most general form given by Lindblad in 1976 [64, 65]. These semigroups are essentially a family of maps that have a few key properties, the most important for this research being complete positivity. The complete positivity condition for a density matrix means that all diagonal values in the density matrix are positive or zero. The probabilities related to the trace of the density matrix and the coherence information at intermediate time steps in the time propagation are therefore retained. More details about quantum dynamical semigroups can be found in Ref. [66].

While the Lindblad master equation is used in this work as an ansatz to form the equations of motion (EOM) (see Chapter 4), it is not the only method available for describing dissipation in quantum dynamical systems. Another well-known alternative is the Redfield approach [67], a method based on a Markovian master equation that has been used in works over the last 50 years [68–70]. The Redfield equations were created using a second order perturbative approach and it also uses the reduced density matrix formalism. Direct integration is achievable for small-medium problems, however the use of stochastic wave function methods is often necessary for scaling. Outside of the weak coupling limit, the Redfield equations become less useful as it is a perturbative method. Another key disadvantage of using the Redfield equations is the non-positivity of the density matrix, that is, the information in the density matrix no longer relates to physical properties. It is only when the average over all time steps is taken that the results are physical. In nuclear fusion reactions, the information from the density matrix can produce some interesting results at intermediate time steps during the time propagation [50], which makes the Redfield approach less useful than the Lindblad approach in this work.

Another alternative approach for describing dissipation to an environment is the Caldeira-Leggett model [71]. This model was developed in 1983 and describes a Brownian particle interacting with a bosonic bath. The quantum system is bilinearly coupled to an infinite bath of harmonic oscillators, which accounts for quantum Brownian diffusion. The coupling with the surrounding thermal bath induces dissipation and decoherence of the system. To achieve this, Caldeira-Leggett starts with the following ansatz: the bath is created with harmonic oscillators coupled to the reduced system, often based on the proximity of the particle and bath. It uses the Markovian approximation and assumes that the system does not affect the bath, i.e., as the bath is assumed to be infinitely large, any information imprinted on the bath by the system is immediately washed away. Although this model has been widely used, it makes some fundamental assumptions of the underlying spectral density, which describes the ‘noise’-spectrum of the bath and assumes a simple Ohmic distribution. However, we choose to use the Lindblad master equation since it is more general and versatile. For example, no assumptions about the spectral density need to be made, and the form of the environment-system interactions is less restricted.

The use of Lindblad dynamics for the evolution of the reduced system is justified due to weak coupling of the system to the complex environment. Additionally, the Markovian approximation is valid due to the adiabatic nature of the nuclei movements compared to the relaxation timescale of the environmental degrees of freedom. For example, once the projectile nucleus is within the fusion pocket, it is assumed that the compound nucleus is formed instantaneously. The complete positivity of the dynamical map means that real probabilities can be derived from diagonal elements of the density matrix at any discretised time step, and the small probabilities linked with tunnelling are well preserved in the auxiliary fusion state.

2.3.1 Applied uses of Lindblad dynamics

Davidsson and Koweleski [47] used the Markovian Lindblad master equation in a molecular dynamics scenario. The wave packet formulations previously employed were unable to record the photon decay which populate intermediate states that contribute to the molecular dissociation of a MgH^+ molecule. Additionally, they note that decoherence is an inevitability when observing photon decay processes and that pure state wavefunctions are unsuitable for modelling this process.

In nuclear physics, the use of Lindblad dynamics was first suggested by Săndulescu, Scutaru and Scheid [72] for describing dissipative deep-inelastic heavy-ion collisions. This was further developed by Isar [73] and it was shown that Lindblad theory could be used for modelling a one-dimensional damped harmonic oscillator and the time evolution of the density matrix was explored. This is relevant to various processes such as cold fission [74], quasifission reactions [75], giant resonances [76, 77] and in theoretical models of quantum optics [78, 79].

Recently, a recurrent neural network (RNN) approach has been used to reproduce the entire time evolution of a two-level atom reduced density matrix which obeys a Lindblad-like master equation by Burgess and Florescu [80]. Non-Markovian effects were generated by a divergence of the local density of states of the electric field at a photonic crystal band gap. The RNN was able to learn the Lindblad equation and thus was able to solve the dynamics of the system much faster than conventional techniques. The results showed that the RNN was capable of reproducing the non-Markovian effects of the environment, due to the implicit time dependence of the RNN architecture.

In quantum biology, an investigation into proton transfer along the hydrogen bonds in a base pair was conducted by Godbeer, Al-Khalili and Stevenson [81] due to the surface having the shape of an asymmetric double-well potential. Proton tunneling would then occur for some protons with less energy than the barrier potential. To measure the effect that quantum tunneling has on the creation of tautomers in DNA, Lindblad theory was used to describe transitions between energy eigenstates and the effect of an environment (water molecules) on energy eigenstate populations. The results showed that environmental couplings increased the tunneling probability in this model but the increase was negligible.

2.4 Summary

This chapter provides general theoretical background that is relevant for understanding key concepts within this thesis. The chosen topics reinforce the relationship between the wave function and a density matrix, provides some background on open quantum systems and how it is used in this work. The use of the Lindblad master equation is justified and a few cases where it has been used in literature are presented.

Chapter 3

The Numerical Methods

3.1 Literature review of numerical methods for time propagation

The Lindblad master equation [60] is composed of the LvN equation for the nondissipative system dynamics and a dissipative Liouvillian, $\hat{\mathcal{L}}_D$, for the dissipative dynamics,

$$\dot{\hat{\rho}}(t) = -\frac{i}{\hbar}\left[\hat{H}_S, \hat{\rho}(t)\right] + \hat{\mathcal{L}}_D\hat{\rho}(t). \tag{3.1}$$

Further details of the EOM used in the present method are given in Chapter 4, from Eq.(4.4) to Eq.(4.13). This section focuses on the numerical methods that are available to solve the Lindblad master equation.

Trying to solve Eq.(3.1) exactly is ideal but this is difficult for problems with large matrix sizes. The calculation of the exponential of an $M \times M$ matrix leads to a number of calculations of order $\mathcal{O}(M^3)$, and this is unsustainable when using a large radial grid, considering energy eigenstates of the projectile or target, and then calculating this over many time steps [82]. As a result, approximations via direct or indirect methods to compute the time evolution of the density matrix are commonly used. The direct methods directly propagate the density matrix and are theoretically more accurate since they contain fewer approximations and often the systematic error is lower [41, 83]. Indirect methods try to approximate the propagation of the density matrix by using many wave packets. These methods tend to be faster and require less memory than direct methods, but due to the approximations that must be made they are less accurate and struggle to be useful when small probabilities are required.

When using a direct approach, Eq.(3.1) must be solved via numerical integration and in matrix form given below

$$\boldsymbol{\rho}(\tau) = \exp(\tau \boldsymbol{\mathcal{L}})\boldsymbol{\rho}_0, \tag{3.2}$$

where $\boldsymbol{\mathcal{L}}$ is a $M \times M$ matrix representation of the Liouvillian, and $\rho(0) = \boldsymbol{\rho}_0$.

The direct approaches of Lindblad and Redfield [64, 67] create an exponential of a large matrix which must be approximated for problems with meaningful sizes. This is because the large matrix must be calculated for every time step which is computationally expensive. There are a few ways to do this including Runge-Kutta integration, split operator techniques, Lanczos methods and polynomial expansions [84–87].

While the Runge-Kutta method is relatively simple to implement and the direct integration was shown to be accurate for calculations in a open quantum system [88], it is relatively slow for large matrix calculations and instead it is often used as verification algorithm [89]. The polynomial expansion methods were found to be of interest due to the advantage of having useful accuracy and realistic propagation times. It is not explicitly known which technique is best for the integration, although one work [53] showed promising results and reasonable execution times for calculation of the time evolution operator on a density matrix, in addition to a relatively simple implementation. This is the technique that was used in this research, the Faber polynomial expansion method. A brief description of this numerical method and other interesting integration methods are given below, with an explanation of their key advantages and disadvantages.

3.2 Polynomial expansion methods

Polynomial expansion methods are a useful numerical tool which can be used to approximate the exponential of a large matrix, often to a sufficient degree of accuracy while maintaining reasonable computational run times. Polynomial expansion techniques have been used in literature for the propagation of a wavefunction [46, 84].

Two polynomial expansion methods that have been shown to be effective when using a density matrix are the Faber polynomials and the Newton interpolation method. The Newton interpolation has been used previously for density matrix propagation, whereas Faber polynomials have been shown to produce similar results, be easier to implement, have better numerical stability and have similar efficiency [53].

The following subsection gives an outline of the Faber polynomial expansion method used and the reasoning behind its use. For more information on the method, see Ref. [53].

3.2.1 Faber polynomials

The Faber polynomials used together with conformal mapping are given by the following recursion relation [53],

$$F_{k+1}(z) = z \cdot F_k(z) - \sum_{j=0}^{k} \gamma_j \cdot F_{k-j}(z) - k \cdot \gamma_k, \quad k \geq 1 \tag{3.3}$$

here γ_k are coefficients from the Laurent expansion of the wavefunction at ∞,

$$\psi(w) = w + \gamma_0 + \gamma_1 w^{-1} + \gamma_2 w^{-2} + \dots , \tag{3.4}$$

and they depend on the shape of the domain, G, which is elliptical for the Faber approximation. The specific conformal mapping is chosen to reduce the memory requirements of the system by maximising the number of non-zero terms in the Laurent expansion,

$$\psi(w) = w + m + \frac{d}{w}, \tag{3.5}$$

where w is a complex number that satisfies the normalisation condition $\lim_{|w|\to\infty} \psi(w)/w = 1$ and m and d are complex parameters that determine the ellipse shape and position. In matrix form, the recursion relation in Eq.(3.3) becomes a three-term recursion [53],

$$F_{k+1}(\boldsymbol{\mathcal{L}})\boldsymbol{\rho}_0 = (\boldsymbol{\mathcal{L}} - m \cdot \boldsymbol{I})F_k(\boldsymbol{\mathcal{L}})\boldsymbol{\rho}_0 - d \cdot F_{k-1}(\boldsymbol{\mathcal{L}})\boldsymbol{\rho}, \quad k > 1 \tag{3.6}$$

where the first three terms are given by,

$$\begin{aligned}
F_0(\boldsymbol{\mathcal{L}})\boldsymbol{\rho}_0 &= \boldsymbol{\rho}_0, \\
F_1(\boldsymbol{\mathcal{L}})\boldsymbol{\rho}_0 &= (\boldsymbol{\mathcal{L}} - m \cdot \boldsymbol{I})\boldsymbol{\rho}_0, \\
F_2(\boldsymbol{\mathcal{L}})\boldsymbol{\rho}_0 &= (\boldsymbol{\mathcal{L}} - m \cdot \boldsymbol{I})F_1(\boldsymbol{\mathcal{L}})\boldsymbol{\rho}_0 - 2d \cdot \boldsymbol{\rho}_0.
\end{aligned}$$

Using Eq.(3.6) with the parameters: $m = 0$ and $d = \frac{1}{4}$, the Faber polynomials F_k were found to be related to the normalised Chebyshev polynomials T_k by the relation $F_k(z) = 2^{1-k}T_k$ for $k \geq 1$ with the initial condition $F_0 = T_0$. Chebyshev polynomials are special Faber polynomials which have been shown to be useful due to their simplicity in a variety of situations for approximating functions [90]. However, their use cannot be applied to this work because these polynomials are not flexible with changes to the strength of dissipation, and the matrix values we use are typically complex whereas the Chebyshev approximation is suited to computing either real or imaginary eigenvalues.

The density matrix propagation in time is approximated accordingly [53],

$$\boldsymbol{\rho}(\tau) = \exp(\tau\boldsymbol{\mathcal{L}})\boldsymbol{\rho}_0 \approx \sum_{k=0}^{n} c_k(\tau)F_k(\boldsymbol{\mathcal{L}})\boldsymbol{\rho}_0, \tag{3.7}$$

where the coefficients $c_k(\tau)$ are solved using the conformal mapping term from Eq.(3.5),

$$c_k(\tau) = \frac{1}{2\pi i}\int_{|w|=1} \frac{\exp\{\tau(w + m + d/w)\}}{w^{k+1}}\, dw, \tag{3.8}$$

and then using the identity $\exp\Big\{z\frac{(x+1/x)}{2}\Big\} = \sum_k (x/i)^k J_k(iz)$, a contour integral can be used and the analytical solution is,

$$c_k(\tau) = \left(\frac{-i}{\sqrt{-d}}\right)^k \exp(\tau m)J_k(2\tau\sqrt{-d}), \tag{3.9}$$

where J_k is a Bessel function of the first kind. If the maximum modulus of the eigenvalues (λ) is known, then the optimal ellipse parameter, $m \in [-2, 0]$, can be determined using the following equation,

$$(1+r^2)m^3+(6r^2-2)m^2+12r^2m+8r^2=0 \tag{3.10}$$

where $r=\mathrm{Im}(\lambda)/\mathrm{Re}(\lambda)$. This sets a couple of constraints: $d=-(m+1)$, as this ensures the ellipse never enters the right part of the complex plane, and the scaling factor is defined as $\sigma=|\lambda/q|$ where $q=\sqrt{1+r^2}\,2rm(2+m)^2/(m^2+r^2(2+m)^2)$.

The Frobenius norm and the coefficients $c_k(n)$ are used to determine the stability of the recursion,

$$||\hat{A}||=\sqrt{\mathrm{tr}(\hat{A}^{\dagger}\hat{A})} \tag{3.11}$$

where $\hat{A}$ is $\mathrm{F}_n(\mathcal{L})\hat{\rho}_0$. The Frobenius norm is stable at approximately 1, and it is sensitive to the scaling of the eigenvalues of $\mathcal{L}$. The modulus of the coefficients is sensitive to the position of the domain, and it is correct when it decreases by many orders of magnitude as more polynomials are used until it becomes stable. Therefore, a local error estimate formed from these quantities can be used [53],

$$\epsilon_{loc}(k)=|c_k(n)|\sqrt{\mathrm{tr}(\mathrm{F}_k^*\mathrm{F}_k)}. \tag{3.12}$$

3.2.2 Newton interpolation

The complex Newton interpolation uses a uniform approximation of an analytic function, F, in a domain G. Interpolation is useful when the approximating function has known values at certain points. The method follows a sequence of steps to approximate a solution [41]:

1. A domain, G, is defined using conformal mapping
2. The interpolation points must be calculated either analytically or numerically
3. The value of the function F can then be calculated on these points
4. The divided difference sequence a_k is then constructed.

The Newton interpolation often uses a rectangular shaped scaled domain [91], however the shape of the domain is not restricted unlike in the Faber approximation. The conformal mapping relation for the Newton interpolation is given as,

$$\psi(w) = w + m - \frac{1}{(2w)^3}, \quad \text{where } m \in \mathbb{C}, \tag{3.13}$$

and this specifies a family of rounded rectangles centered at m. The interpolation sampling points z_k should be evenly spaced on the boundary of the domain and are often chosen to be the eigenvalues λ_n of the superoperator $\boldsymbol{\mathcal{L}}$. A 2 term recursion gives the Newton polynomials $\{\omega_k(\boldsymbol{\mathcal{L}})\boldsymbol{\rho}_0\}_{k\in\mathbb{N}}$ in matrix form,

$$\omega_{k+1}(\boldsymbol{\mathcal{L}})\boldsymbol{\rho}_0 = (\mathcal{L} - z_{k+1} \cdot \mathbf{I})\omega_k(\boldsymbol{\mathcal{L}})\boldsymbol{\rho}_0, \tag{3.14}$$

with the initial condition being $\omega_0(\mathcal{L})\boldsymbol{\rho}_0 = \boldsymbol{\rho}_0$.

The expansion coefficients a_k are calculated from the divided difference algorithm, the first two terms are given as an example: $a_0 = F(z_0)$, $a_1 = (F(z_1) - F(z_0))/(z_1 - z_0)$ [41].

By expanding an analytic function within the domain of G, $f(\boldsymbol{\mathcal{L}})\boldsymbol{\rho}_0 = \exp(\tau\boldsymbol{\mathcal{L}})\boldsymbol{\rho}_0$, the Newton interpolation of order n is given by the following

$$\exp(\tau\boldsymbol{\mathcal{L}})\boldsymbol{\rho}_0 \approx P_n^\tau(\boldsymbol{\mathcal{L}})\boldsymbol{\rho}_0 = \sum_{k=0}^{n} a_k \exp\left(\omega_k(\boldsymbol{\mathcal{L}})\right)\boldsymbol{\rho}_0, \tag{3.15}$$

After the interpolation points and divided difference coefficients are calculated, the error can be checked by testing a value of the polynomial $P_m(z_{test})$ and the function $F(z_{test})$. More polynomials should be included if the calculated error is too high. One disadvantage of this method is that the errors are not smooth due to the divided difference coefficients i.e. the error will oscillate as n increases.

A previous study conducted a review of the Faber approximation and Newton interpolation methods within a molecular dynamics setting [53], using a damped harmonic oscillator with weak dissipation and using a grid with 128 points. The overall finding was that both methods were similar in many respects – memory occupation, generation of coefficients, efficiency of their algorithms. The primary difference was that the Faber approximation is simpler to implement and was slightly more stable at higher polynomial orders.

3.3 Indirect methods

Indirect methods do not propagate a density matrix but instead the density matrix is represented as a function of wave vectors. These approaches are statistical and have the advantage of being numerically efficient which is important as numerical propagation of a density matrix is a limitation for direct methods. A few relevant methods that have been used in literature are discussed below.

3.3.1 Variational wave packet (VWP) method

This method used in Ref. [92] takes the reduced density operator and expands it into a basis of time-dependent wave functions,

$$\hat{\rho}(t) = \sum_{u=1}^{n} \sum_{v=1}^{n} \rho_{uv}(t) \left| \psi_u(t) \right\rangle \left\langle \psi_v(t) \right| , \tag{3.16}$$

where $|\psi_{u,v}(t)\rangle$ are the time-dependent expansion wave functions, $\rho_{uv}(t)$ are the time-dependent coefficients and n is the number of expansion wave functions used. For a dimension N in the relevant Hilbert space, the number of matrix elements for a density matrix is N^2. The density operator in Eq.(3.16) would use $n^2 + nN$ number of matrix elements. The number of expansion wave functions n can be much smaller than N and therefore computational resources needed for the time propagation of the density matrix could be greatly reduced.

The VWP method was tested using a three-mode vibronic coupling system, weakly coupled to a dissipative environment [92]. The conclusions stated that the computational expense was similar to that of a Monte-Carlo wave function propagation method, but their result for linear polarisation was closer to the converged result. This approach seemed effective for the investigation of coherent short time dynamics, but one limitation is that this method struggles to calculate expectation values of observables in the long time limit when the system dynamics become completely incoherent.

3.3.2 Monte Carlo Wave function (MCWF) method

An example of the Monte Carlo wave function (MCWF) method is given in Ref. [93], where it is used to study the fluctuation and dissipation as a result of quantum jumps in quantum optics. Instead of treating the dissipative coupling of a small system and a large reservoir with a master equation, the MCWF uses a non-Hermitian Hamiltonian and random quantum jumps, after which the wave function is renormalised. It was shown that the MCWF is equivalent to the LvN equation and that for sufficiently large n outcomes, one can calculate a quantum average via Eq.(3.17)

$$\langle A\rangle_{(n)}(t) = \frac{1}{n}\sum_{i=1}^{n}\left\langle\phi^{i}(t)\right| A \left|\phi^{i}(t)\right\rangle . \tag{3.17}$$

The equivalence is valid since the density matrix can be described as an ensemble of systems populating different states depending on probability. The efficiency of MCWF calculations is dependent on the type of operator used. In this example, local operators were less efficient than density matrix calculations, whereas global operators were equal or better than them provided that N (the number of levels involved) was larger than n (the number of wave functions required). One clear disadvantage is the loss of information due to the averaging that takes place, and therefore knowledge of the contribution from individual systems to an observable is lost.

3.3.3 Stochastic surrogate Hamiltonian Method

Another stochastic method which works by propagating many wave packets to replace the calculation of the time evolution of a density matrix is the stochastic surrogate Hamiltonian method [94]. This method solves the time-dependent Schrödinger equation (TDSE) instead of the LvN equation. An initial state is obtained by averaging many realisations of the system-bath wave packets.

The stochastic surrogate Hamiltonian method uses two baths, the second being a stochastic bath that has the same frequency spectrum as the primary bath. At random times, bath modes with the same frequencies are swapped, which reduces the recurrence time of the first bath considerably. This method is an improvement over the surrogate Hamiltonian method, since it allows for longer time propagation of the system-bath dynamics. Additionally, every realisation of the dynamics is unitary, linear and efficient propagation methods can be deployed. This method shares the problems with indirect methods, where the calculations contain too much noise and limits its ability to produce meaningful low-probability values.

While there are distinct advantages to using these indirect methods, for nuclear fusion reactions the direct methods are often favoured because of the high accuracy needed when using low energies well-below the Coulomb barrier. Chapter 4 gives an in-depth description of the approach used in this work.

3.4 Methods for calculation of the kinetic energy operator

3.4.1 Fourier grid method

The main method that is used for the action of the kinetic energy operator on the density matrix is the Fourier grid method. This method uses a combined forward and backward discrete Fourier transform to change the representation from configuration space to momentum space [41, 95],

$$\tilde{\rho}(k_p, k_q') = \frac{1}{2\pi N} \sum_{m=0}^{N-1} \sum_{n=0}^{N-1} \hat{\rho}(r_m, s_n) e^{2\pi i (\frac{-pm}{N} + \frac{qn}{N})}, \tag{3.18}$$

for N grid points, $p = 0, 1.., N-1$ and $q = 0, 1.., N-1$.

The advantage of this method comes from the simpler calculations required when using the kinetic operator $\hat{T}$ in momentum space,

$$\hat{T} = \frac{\hbar^2 \hat{k}^2}{2\mu} \qquad \hat{k} = -\frac{i}{\hbar}\frac{\partial}{\partial r}, \tag{3.19}$$

where μ is the reduced mass and r is the position on the radial grid. After the calculation, the inverse of this Fourier transform is used to change the representation back to configuration space. The potential energy matrix used is diagonal,

$$V_{ii'} = \delta_{ii'} V(x_i). \tag{3.20}$$

Although there are methods that reduce the computational cost of this calculation in configuration space (see DVR method), the calculations in momentum space were notably quicker provided that the Fourier transform does not take longer than the configuration space calculations. Since the Fourier grid method is able to take advantage of the fast Fourier transform (FFT) algorithm, it is much more favourable to use the Fourier grid method for the time propagation of the density matrix. Both the Fourier grid and DVR methods were tested and it was found that the accuracy of one method did not differ from the other.

3.4.2 The discrete variable representation method

The discrete variable representation (DVR) gives the kinetic and potential energy in grid point representation. This simple kinetic energy relation allows the kinetic energy to be calculated solely using the grid spacing, provided that the grid is equally spaced. In addition, the grid representation of the kinetic energy is a property of the grid itself and not dependent on any underlying basis set [96]. In one dimensional Cartesian coordinates for the end points of the grid $a = 1.5$ fm and $b = 150$ fm and grid size N, the grid point representation of the kinetic energy is given by Eq. (3.21)

$$T_{ii'} = \frac{\hbar^2(-1)^{(i-i')}}{2m\Delta r^2} \begin{cases} \pi^2/3 - 1/2i^2, & i = i' \\ \dfrac{2}{(i-i')^2} - \dfrac{2}{(i+i')^2} & i \neq i', \end{cases} \tag{3.21}$$

with $\Delta r = (b-a)/N$ and the potential energy matrix $V_{ii'}$ is the same as Eq.(3.20)

For in depth details on the method and the enhanced efficiency compared to a ‘full’ Hamiltonian matrix, see Ref. [96]. An example of a widely used DVR approach is the Lagrange-mesh method [97].

3.5 Summary

The time propagation of the EOM is essential for the work in this thesis, and the size of the matrix required for stable calculations is too large for exact methods to be used for the time propagation. The numerical methods available for the approximation of the EOM have been discussed and the use of polynomial methods, in particular Faber polynomials, proved to be an efficient, dependable and simple to implement method. The Fourier grid method for calculating the action of the kinetic energy operator is explained and it is the method of choice due to its accuracy and faster calculation time.

Chapter 4

The Coupled-Channels Density-Matrix (CCDM) Approach

The fundamental physics concept in the coupled-channels model is that the colliding nuclei are in a coherent superposition of intrinsic states, due to the coupling between the radial motion and intrinsic degrees of freedom.

The CCDM approach is based on three steps:

1. Definition of an initial density matrix
2. Time propagation
3. Analysis of the time-propagated density matrix

Steps 1 and 2 are presented in this chapter, with the numerical techniques for the time propagation discussed in the previous chapter. Chapter 5 is devoted to a specific technique — the window operator method, for step 3. This approach has previously been used in literature to quantify quantum decoherence effects on asymptotic observables [51], however the energy resolution of a density matrix using the window operator is a significant advancement in the present work.

4.1 The initial density matrix

For a system of two collision partners in their ground states, the radial components of the initial density matrix are formed by a wave packet that is a function of the radial grid position, r,

$$\rho_{11}^{rs}(t=0) = |r\rangle \langle s| \,, \tag{4.1}$$

where $|r\rangle$ and $\langle s|$ are position states on the radial grid, that allow for indexing across the radial space. The density matrix created from the wavefunction above would be correct if the target and projectile nuclei were to remain only in their ground states. However, for every position on the radial grid, the target and/or projectile could be in an excited state. Therefore the density operator is a tensor and is formed from a mixed basis of states: the radial position and intrinsic energy states,

$$\hat{\rho} = \sum_{i,j,r,s} |r\rangle \, |i\rangle \, \rho_{ij}^{rs}(t) \, \langle j| \, \langle s| \,, \tag{4.2}$$

where $|i\rangle$ and $\langle j|$ are energy eigenstates of the asymptotic (internal) Hamiltonian of each separate nucleus, and they describe the energy state of the system. There are some qualities that the density operator must fulfil in order to extract meaningful probabilities at each propagation time step. The density operator must be Hermitian and positive semi-definite[*] because the diagonal elements of the density matrix are the coefficients $\rho_{ii}^{rr}(t)$, which have the physical meaning of probabilities. More information on the reasoning behind this condition is given below in Section 4.2.

4.2 Equations of motion

4.2.1 Nondissipative dynamics

It is well-known that the TDSE describes the time evolution of a wavefunction [98],

---

[*] Positive semi-definite: all eigenvalues within the density matrix must be equal to or above 0.

$$i\hbar\frac{d}{dt}\left|\psi(t)\right\rangle = \hat{H}\left|\psi(t)\right\rangle . \tag{4.3}$$

The equivalent equation to describe the time evolution of a density matrix is the nondissipative Liouville-von Neumann (LvN) equation [41,99],

$$\hat{\mathcal{L}}_H\hat{\rho}(t) = \frac{\partial\hat{\rho}(t)}{\partial t} = -\frac{i}{\hbar}\left[\hat{H}_S,\hat{\rho}(t)\right], \tag{4.4}$$

where $\left[\hat{H}_S,\hat{\rho}(t)\right] = \hat{H}_S\hat{\rho}(t) - \hat{\rho}(t)\hat{H}_S$ is the commutator, and $\hat{H}_S$ is the reduced system Hamiltonian,

$$\hat{H}_S = \hat{H}_1(r) + \hat{H}_0(\xi) + V(r,\xi). \tag{4.5}$$

Further definition of the $\hat{H}_S$ components are described below:

1. The nuclear and Coulomb forces between the two nuclei, $\hat{H}_1(r) = \hat{T} + \hat{U}$, where $\hat{T}$ and $\hat{U}$ are the kinetic energy operator and the total bare nucleus-nucleus real potential respectively. Explicitly, $\hat{U}$ is the monopole interaction potential between two nuclei in their ground states.
2. The intrinsic Hamiltonian determined from the considered excited states of the target or projectile, $\hat{H}_0(\xi)$.
3. The total real coupling potential which determines how the radial motion affects the population of the internal energy spectrum, $V(r,\xi)$.

Here $\hat{U} = U_N(r) + U_C(r)$ where U_N is the strong force nuclear potential, which is modelled using the Woods-Saxon potential,

$$U_N(r) = -\frac{V_{\text{WS}}}{1+\exp\left(\dfrac{r-R_{\text{WS}}}{a_{\text{WS}}}\right)}, \tag{4.6}$$

where V_{WS} is the strength of the potential, $R_{\text{WS}} = r_{\text{WS}}(A_P^{1/3} + A_T^{1/3})$ is the range of the Woods-Saxon potential and a_{WS} is the diffuseness parameter. The Woods-Saxon constants used for the ^{16}O + ^{144}Sm system are given in Table 6.1. The Coulomb potential $U_C(r)$ is given by the Coulomb law for the electrostatic potential between two point charges,

$$U_C(r) = \frac{Z_P Z_T e^2}{r}, \tag{4.7}$$

where Z_P and Z_T are the unit charges of the projectile and target respectively. This approximation is adequate for the calculations in this work since we do not consider the dynamics of when the colliding nuclei overlap, similarly to the coupled-channels equations in Eq.(1.2). If one is interested in considering the dynamics of overlapping nuclei, detailed modelling of the colliding nuclei is required, and this can be achieved with models based on TDHF theory [22].

The model values of $\hat{U}$ and $V(r, \xi)$ for the test nuclei ^{16}O + ^{144}Sm are plotted in Fig. 4.1 to show the position and strength of these potentials, in addition to the Γ decay function, a function used to model fusion in these calculations. Plotting $V(r, \xi)$ shows the localisation of the coupling potential which is negligible until a position near the Coulomb barrier is reached. The coupling potential is composed of coupling matrix elements, V_{ij}^{rr}, that are functions of the radial position, β deformation parameter and energy level of the excited state. For the calculations in this work, we require the use of rotational and vibrational couplings, and these are implemented in the same manner as Ref. [31].

Including these terms and using the density matrix given in Eq. (4.2), the nondissipative dynamics are described by the following equation,

$$\begin{aligned}(\hat{\mathcal{L}}_H \hat{\rho})_{ij}^{rs} = -\frac{i}{\hbar} \Bigg\{ \rho_{ij}^{rs}\,(e_i - e_j) + \sum_{t=1}^{M} (T^{rt}\,\rho_{ij}^{ts} - \rho_{ij}^{rt}\,T^{ts}) \\ + \rho_{ij}^{rs}\,(U^{rr} - U^{ss}) + \sum_{\mu=1}^{N} (V_{i\mu}^{rr}\,\rho_{\mu j}^{rs} - \rho_{i\mu}^{rs}\,V_{\mu j}^{ss}) \Bigg\},\end{aligned} \tag{4.8}$$

where e_i and e_j are the eigenenergies of the intrinsic Hamiltonian $\hat{H}_0$, and M and N determine the maximum size of the radial grid and the number of energy levels included respectively. A derivation of Eq.(4.8) is given in Appendix A.

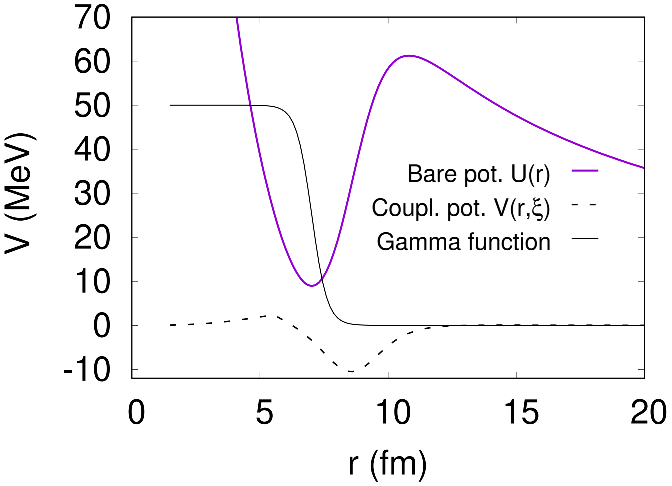

Figure 4.1: The potentials for the test collision ^{16}O + ^{144}Sm, as a function of internuclear radius, r. The thick purple solid line is the total, bare nucleus-nucleus potential $U(r)$ and the dashed line is the total coupling potential, $V(r, \xi)$, between the ground state and the 3^- vibrational excited state (1.81 MeV) of ^{144}Sm. This state is chosen since it was shown to have a greater effect on fusion than the low-lying 2^+ excited state [12]. The thin black solid line is the decay function Γ, a Fermi function that removes positional probability from the reduced system density matrix due to compound nucleus formation.

4.2.2 Dissipative dynamics

In nuclear fusion reactions, the formation of an excited compound nucleus leads to irreversible dissipation of energy that happens within the fusion pocket, located past the Coulomb barrier. For a nucleus to interact with the fusion environment and become an excited compound nucleus, it must have enough energy to overcome the Coulomb barrier or if the energy is near or below the barrier it can penetrate the Coulomb barrier via quantum tunneling. The latter interaction is more interesting since above-barrier calculations and experiments can be described classically and are relatively simple to conduct. When any part of the reduced mass wave packet is localised inside the fusion barrier, fusion is considered to happen instantaneously and a compound nucleus with its own nuclear states is formed. Another environment that has been considered is created by giant dipole resonances (GDRs) [100]. GDRs are the result of collective excitations of the nucleons within the nucleus, causing the protons and neutrons to oscillate, move collectively against each other and create a separation between the centre of mass and charge which generates an electric dipole moment [101]. The decay of the GDR is independent of the dynamical couplings and only non-collective excited states would be coupled to a GDR excitation, causing thermal excitations in the nuclei [102]. These two environments contain complex nuclear excitation modes which cannot currently be described within the reduced system Hamiltonian and a method of treating dissipation is needed. Note that the calculations in this work do not include the GDR environment, but it has been used successfully in literature [50,51].

The irreversible dynamics in this work are described using the dissipative part of the Lindblad master equation (also called the Gorini–Kossakowski–Sudarshan–Lindblad equation), which introduces quantum decoherence and dissipation through a dissipative Liouvillian:

$$\hat{\mathcal{L}}_D \hat{\rho} = \sum_{\alpha} \left(\hat{\mathcal{C}}_\alpha \, \hat{\rho} \, \hat{\mathcal{C}}_\alpha^\dagger - \frac{1}{2} \left[\hat{\mathcal{C}}_\alpha^\dagger \hat{\mathcal{C}}_\alpha, \hat{\rho} \right]_+ \right) \tag{4.9}$$

where $[...]_+$ denotes an anticommutator. The Lindblad operators, $\hat{\mathcal{C}}_\alpha$, are used to treat the dissipation of the system to the environment. These are often phenomenologically chosen depending on calculated relaxation rates. The probability of the transition between energy states $|j\rangle \rightarrow |i\rangle$ at a given radial position r is given by Γ_{ij}^{rr} and the Lindblad operator for a spontaneous decay can be rewritten as

$$\hat{\mathcal{C}}_{ij} = \sqrt{\Gamma_{ij}^{rr}} \, |i\rangle \, \langle j| \, . \tag{4.10}$$

To describe the decay to environmental states, the $|i\rangle$ basis is enlarged and replaced by $|k\rangle$, such that $|i\rangle \subset |k\rangle$. This allows the dissipation of energy from the ground state and excited states of the nuclei to these environment states, which are referred to as auxiliary states since they are not reaction channels but simply states that measure the dissipation of the reduced system [103]. Then the dissipative dynamics for the open system is explicitly described by the following equation

$$(\mathcal{L}_D \hat{\rho})_{kl}^{rs} = \delta_{kl} \sum_{\nu} \sqrt{\Gamma_{k\nu}^{rr}} \, \rho_{\nu\nu}^{rs} \sqrt{\Gamma_{k\nu}^{ss}} - \frac{1}{2} \sum_{\nu} (\Gamma_{\nu k}^{rr} + \Gamma_{\nu l}^{ss}) \rho_{kl}^{rs}, \tag{4.11}$$

where ν runs over all the $|k\rangle$ basis states and $\Gamma_{kk}^{rr} = \sum_{\nu \neq k} \Gamma_{\nu k}^{rr}$. This condition records the transitions from the $|k\rangle$ states to other states within the diagonal elements of the decay matrix Γ^{rr}_{kk} and is positive to keep the density matrix positive semi-definite [48]. Then the EOM describing the time evolution of the density matrix are separated into a density matrix for the reduced system given as

$$\begin{aligned}\dot{\rho}^{rs}_{ij} = -\frac{i}{\hbar}\Bigg\{\rho^{rs}_{ij}\,(e_i - e_j) + \sum_{t=1}^{M}(T^{rt}\,\rho^{ts}_{ij} - \rho^{rt}_{ij}\,T^{ts}) \\ + \rho^{rs}_{ij}\,(U^{rr} - U^{ss}) + \sum_{\mu=1}^{N}(V^{rr}_{i\mu}\,\rho^{rs}_{\mu j} - \rho^{rs}_{i\mu}\,V^{ss}_{\mu j})\Bigg\} \\ + \delta_{ij}\sum_{\nu}^{B}\sqrt{\Gamma^{rr}_{i\nu}}\,\rho^{rs}_{\nu\nu}\sqrt{\Gamma^{ss}_{i\nu}} - \frac{1}{2}\sum_{\nu}^{B}(\Gamma^{rr}_{\nu i} + \Gamma^{ss}_{\nu j})\rho^{rs}_{ij}, \quad (4.12)\end{aligned}$$

and the time evolution of the density matrix involving the environmental states is given below

$$\dot{\rho}^{rs}_{kl} = \delta_{kl}\sum_{\nu}^{B}\sqrt{\Gamma^{rr}_{k\nu}}\,\rho^{rs}_{\nu\nu}\sqrt{\Gamma^{ss}_{k\nu}} - \frac{1}{2}\sum_{\nu}^{B}(\Gamma^{rr}_{\nu k} + \Gamma^{ss}_{\nu l})\rho^{rs}_{kl}, \quad (4.13)$$

where B is the total number of excited states and environment states. In Eq.(4.13), either k or l must be different from the i (excitation channel) states, otherwise this equation would only be describing the reduced system dissipation. For example, if the $|i\rangle$ basis contains the $|1\rangle$ and $|2\rangle$ states and an environment state is described by $|3\rangle$, then $k = 3$ and $l = 1$ or $l = 2$ describes the dissipation from $|1\rangle$ or $|2\rangle$ to $|3\rangle$. The Γ function in Fig.4.1 determines the strength of the transitions between states or the absorption to an environmental state depending on the internuclear distance, r. Details of the derivation of the dissipative Liouvillian are given in Appendix B.

4.3 Collision dynamics of the present numerical method

In this model, conceptually there is a projectile nucleus (A_P) and a target nucleus (A_T) that are initially separated at a distance so that virtually no interactions between them are present (due to nuclear and Coulombic effects) and they reside in their ground states. The collision described is direct and it is assumed that there is no change in angular momentum ($L = 0$).

To record the dynamics between the two nuclei of interest, a wave packet is used to describe the relative motion of the nuclei. The wave packet describes the reduced mass moving forward in space and a visual representation is shown in Fig.4.2.

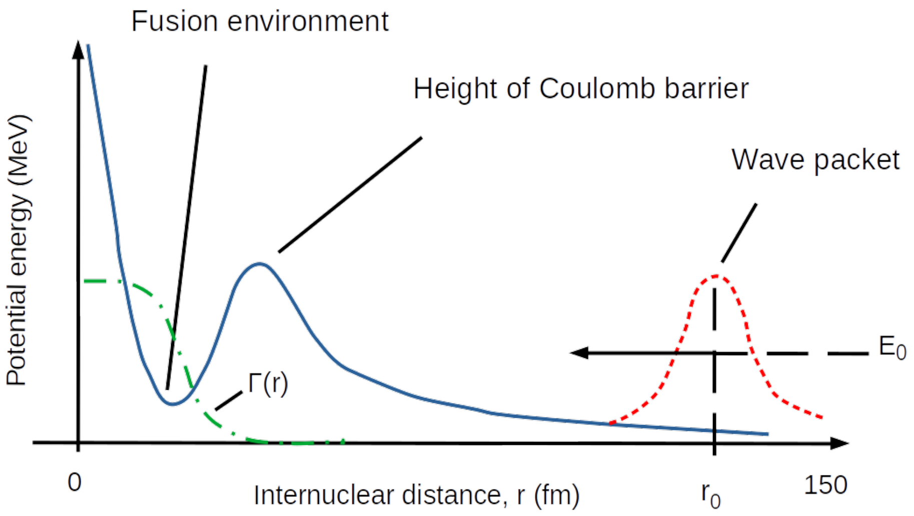

Figure 4.2: A visual representation of the propagation dynamics. The wave packet (red dashed line) with average energy E_0 and initial centroid position r_0 moves closer to the Coulomb barrier (blue solid line) in time steps of 10^{-22} s. The fusion environment is localised behind the Coulomb barrier in which fusion takes place when the wave packet encounters the Γ function (green dot dashed line).

Two wave packets were tested to examine the effects of different wave packet constructions on the dynamics. Firstly, an initial minimum uncertainty Gaussian wave packet in the centre of mass reference frame was used,

$$\psi(r, r_0, \sigma_0, k_0) = \mathcal{N}^{-1} \exp\left(-\frac{(r-r_0)^2}{2\sigma_0^2}\right) e^{-ik_0 r}, \tag{4.14}$$

here r_0 is the initial, central position of the Gaussian wave packet, r is the set of grid positions that the wave packet can occupy, k_0 is the average wave number and σ_0 is the spatial dispersion. $\mathcal{N} = (2\pi\sigma_0^2)^{1/4}$ is a normalisation constant. This wave packet is used to construct the radial part of the density matrix in Eq. (4.2).

The minimum uncertainty Gaussian wave packet initially implemented assumed an asymptotic free-particle Hamiltonian, H_0. It is thought that the small fusion probabilities associated with energies below $E_{\text{c.m.}}/V_B < 0.9$ could be affected by Coulomb interactions at relatively long distances [104, 105]. Hence, an alternative Coulomb wave packet was constructed, which considers the Coulomb interaction at large distances by replacing the plane wave in Eq.(4.14) by an incoming Coulomb wave $H^-_{L=0}$ [106],

$$\psi_{Coul}(r, r_0, \sigma_0, k_0) = \mathcal{N}^{-1} \exp\left(-\frac{(r-r_0)^2}{2\sigma_0^2}\right) H^-_{L=0}(k_0 r) \tag{4.15}$$

where the Coulomb wave argument $k_0 r$ is the product of the average wave number and the position on the radial grid. Theoretically, the initial position of the wave packet should no longer be affected by the 'tail' of the Coulomb barrier, and the propagation dynamics should be more accurate.

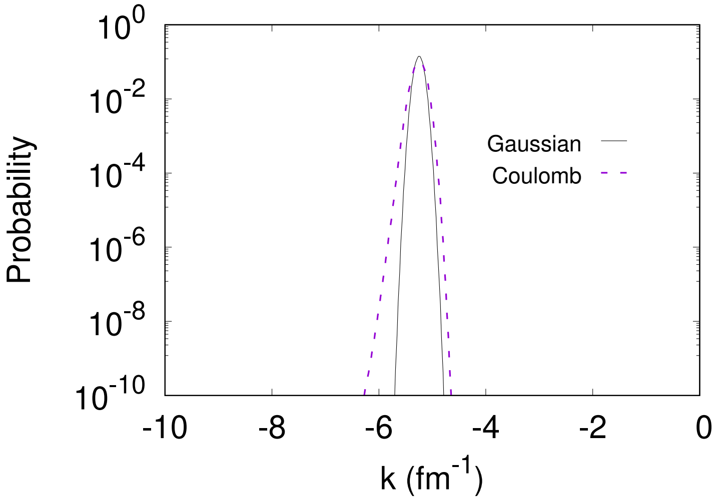

Figure 4.3: For the ^{16}O + ^{144}Sm system, an initial Gaussian wave packet (solid black line) was compared to an initial Coulomb wave packet (dashed purple line) in k space at $t = 0$ zs. Both of these wave packets had initial radial positions of $r_0 = 70$ fm and spatial dispersion $\sigma_0 = 10$ fm.

Testing this Coulomb wave packet showed that it could not describe fusion probabilities lower than those obtained using the Gaussian wave packet. However, it was better at describing the entire spectrum of energies than the Gaussian wave packet. This is useful when the Gaussian wave packet is only able to describe a narrow range of energy-resolved fusion probabilities. Inspecting the shape of an initial Coulomb wave packet compared to an initial Gaussian wave packet in Fig.4.3, the Coulomb wave packet had a broader peak toward higher k-numbers which could explain the worse resolution at low energies but wider range of correct energy-resolved fusion probabilities. Both of these wave packets are used throughout this study to benefit from their respective strengths.

As A_P moves toward A_T in coordinate space, the density matrix stores the interaction information for each discretised time step. The initial density matrix at $t = 0$ describes a pure, coherent state ($\mathcal{P} = 1$ and $S_{vn} = 0$), and it is represented in a mixed basis of states composed of: i) the eigenstates of the internal Hamiltonian of each individual nuclei and ii) a radial grid basis for their radial motion. The coupled-channels method uses a Hamiltonian that couples the target and projectile excitations with their radial motion so that induced excitation can occur. For the sake of simplicity and to reduce the computational time, in the studies with ^{144}Sm, only the ground state (0^+) and one excited state ($3^-, 1.81$ MeV) of the ^{144}Sm target are considered due to computational considerations. This limitation is not expected to affect the dynamics significantly because the probability of higher-level induced excitations above the first excited state is much lower. A similar constraint is applied to the calculations involving ^{188}Os. For the nuclear friction calculations using ^{92}Zr, two excited states with energies of 0.93 and 2.34 MeV are used. These are included since coupling to these states are non-negligible and studies in literature have included both excited states, and to demonstrate the handling of multiple excited states by the CCDM method. Nevertheless, future studies would benefit from the inclusion of higher level states for completeness, when the means to do so becomes available. Coupling to the ^{16}O projectile was neglected due to its first excited state being 6.13 MeV, hence the coupling to this state is negligible.

Lastly, a Woods-Saxon shaped potential is used for the Γ function within the fusion pocket, allowing positional probability to be removed from the reduced density matrix since the target and projectile will become a compound nucleus after fusion. This is represented by $\Gamma(r)$ in Fig. 4.2. The removal of probability is important for describing the irreversibility of fusion. The shape of the Γ function ensures that only wave packet components that reach the fusion well are absorbed. The numerical algorithm used for the time propagation of the EOM was the Faber polynomial expansion, explained in Chapter 3.

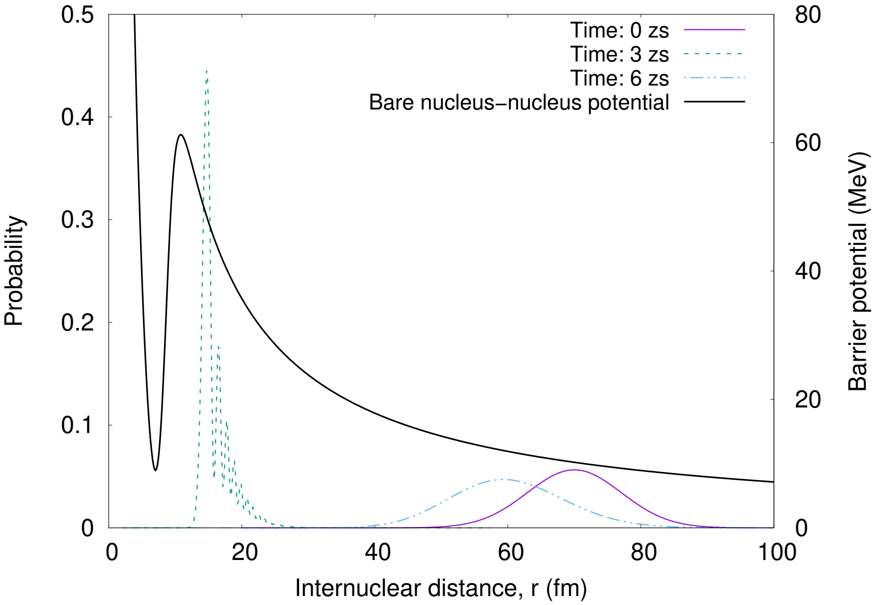

Figure 4.4: Snapshots of the diagonal elements of the density matrix (using an initial Gaussian wave packet shape) as a function of the internuclear distance for various times in the propagation: 0 zs (purple, solid line), 3 zs (green, dotted line) and 6 zs (blue, dotted and dashed line). The bare nucleus-nucleus potential for the test nuclei ^{16}O + ^{144}Sm is the thick black solid line. This figure shows the time evolution of the density matrix at significant times in the propagation, from the initial density matrix at $t = 0$ zs, to a point of near approach at $t = 3$ zs, to the reflected, reduced amplitude density matrix at $t = 6$ zs.

As stated earlier, one of the benefits of this approach is the ability to visualise the dynamics at any time step of the calculation as shown in Figure 4.4. The dynamics can be followed for every time step however three were chosen to highlight what happens to the density matrix during the time evolution. At $t = 0$ zs[‡], the initial density matrix with a minimum uncertainty Gaussian shape is positioned at r_0. At $t = 3$ zs, the nuclei are around their point of nearest approach, and hence the density matrix probability is strongly localised just outside the barrier and has begun to be reflected. Finally at $t = 6$ zs, the density matrix elements that did not encounter the fusion pocket are reflected back, retaining its Gaussian shape with a lower amplitude due to the loss of probability. It should be noted

---

[‡] 1 zs = 1×10^{-21} s

that a very similar result is obtained when using the Coulomb wave packet.

4.4 Summary

This chapter discusses two of the steps required to apply the CCDM method to heavy-ion reactions: defining an initial density matrix and describing the equations of motion that are used for the time propagation. The nondissipative and dissipative dynamics are presented, with the former describing the reduced system Hamiltonian and includes couplings between the internal excited states and the latter describing dissipation to environment states. This method uses a wave packet that propagates in time and there are two types that we consider, Gaussian and Coulomb wave packets. The strengths and weaknesses of both are discussed. Conceptual information is provided to assist the reader in visualising the collision dynamics.

Chapter 5

The window operator

By modelling the projectile and target as a wave packet moving in space, the wave packet has a distribution of energies, with average energy E_0. To calculate the fusion probability of the wave packet, the standard approach is to sum the fusion probability contributions from all energies within the wave packet, obtaining the total fusion probability for a fusion reaction. However, summing the contributions does not allow for the observation of small probability contributions from energies well-below the Coulomb barrier, since the higher energies dominate the fusion probability. Therefore, a method is needed to resolve the energies of the wave packet and calculate energy-resolved fusion probabilities to fully understand these low-energy contributions.

After time propagation of the EOM described in Chapter 4, the window operator is applied to the time-propagated density matrix to obtain the energy-resolved fusion probabilities. This chapter gives some background on how the window operator has been used in previous studies and the modifications conducted to apply the window operator to a density matrix.

5.1 Introduction to the window operator method

The window operator, $\hat{\Delta}$, is an operator that can be used to resolve the energy of the initial and final wave packets of the time propagation to obtain the probability ($P(E_k, n, \epsilon)$) of finding a projectile nucleus with initial energy E_k inside the fusion pocket [107]. It is an established method for calculations involving wave functions [38,108,109] and the equations for its use with a final-state wave function with a final-state Hamiltonian $\mathcal{H}$ is given below,

$$\hat{\Delta}(E_k, n, \epsilon) = \frac{\epsilon^{2^n}}{(\hat{\mathcal{H}} - E_k)^{2^n} + \epsilon^{2^n}}, \tag{5.1}$$

$$P(E_k, n, \epsilon) = \langle \psi_f | \, \hat{\Delta}(E_k, n, \epsilon) \, | \psi_f \rangle \, . \tag{5.2}$$

The window operator is dependent on three inputs: E_k as described above, ϵ which is effectively a resolution parameter and determines the width of the energy bins, and n is a parameter that determines the overlap of the energy bins, with higher values creating increasingly separated rectangular bins. Figure 5.1 plots the window function for a range of arbitrary E values above and below E_k. Using Eqs.(5.1) and (5.2), the meaning of the window function is clear from Eq.(5.3) where $P(E_k, n, \epsilon)$ is the sum over the projection onto all eigenstates $|m\rangle$ of $\mathcal{H}$ within the energy range $E_k \pm \epsilon$, multiplied by the window function,

$$P(E_k, n, \epsilon) = \sum_m | \, \langle \psi_f | m \rangle \, |^2 \frac{\epsilon^{2^n}}{(E_m - E_k)^{2^n} + \epsilon^{2^n}}. \tag{5.3}$$

Using the window function means that some contributions from energies outside the energy bin of interest will be included in the calculation of energy-resolved fusion probability for each E_k value (unless $n = \infty$), but at $n = 2$ these contributions are already insignificant. Figure 5.1 also demonstrates why the correct spacing between successive values of E_k is always 2ϵ, as it gives the optimal amount of overlap between successive window function operations and avoids misleading results.

When using $n = 1$, which would require the least computational resources, the overlap is too significant with a sharp peak resulting in poor separation of the energy bins. It was found that the overlap between bins was sufficiently small enough when $n = 2$, and higher n values decreases the overlap further but the additional accuracy did not increase [107]. For $n = 2$, successive linear equations can be solved to obtain a vector $|\chi_k\rangle$

$$(\hat{\mathcal{H}} - E_k + \sqrt{i}\epsilon)(\hat{\mathcal{H}} - E_k - \sqrt{i}\epsilon) \left| \chi_k^{(2)} \right\rangle = |\psi_f\rangle \, , \tag{5.4}$$

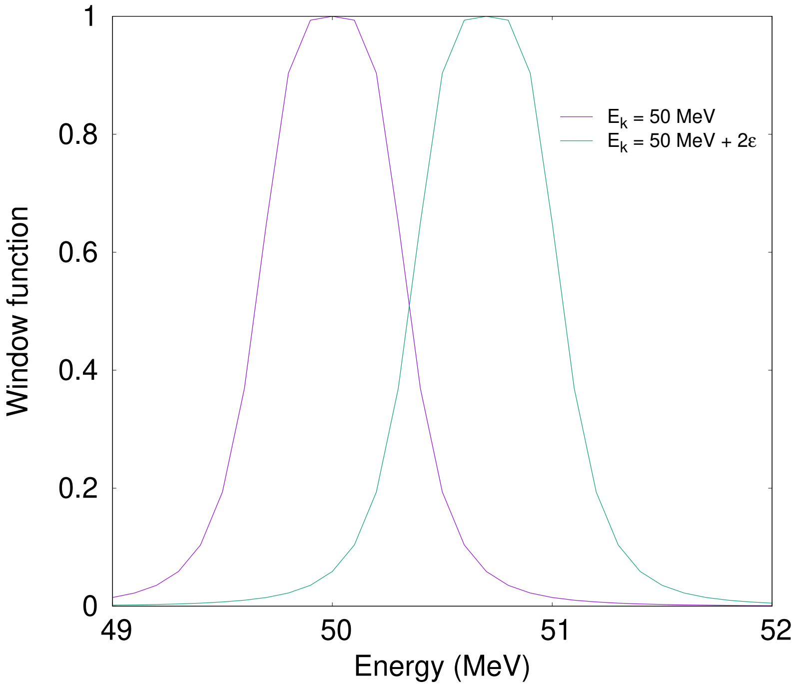

Figure 5.1: The two window functions, centred around energies E_k and E_{k+1}, with the spacing between energies being 2ϵ. The values of n and ϵ were 2 and 0.35 MeV respectively.

where $\left\langle \chi_k^{(2)} \middle| \chi_k^{(2)} \right\rangle = P(E_k, n, \epsilon)$. In the limit of $n \to \infty$, the window function is rectangular, and the evaluation of the window function becomes

$$\lim_{n\to\infty} \left[\hat{\Delta}(E_k, n, \epsilon)\right] = \begin{cases} 1, & \text{for } (E_k - \epsilon) \leq E_k \leq (E_k + \epsilon) \\ 0, & \text{otherwise.} \end{cases} \tag{5.5}$$

In this study we have applied the window operator to a density matrix, firstly using Eq.(2.6) to express $P(E_k, n, \epsilon)$,

$$P(E_k, n, \epsilon) = \mathrm{Tr}\left[\hat{\Delta}(E_k, n, \epsilon)\hat{\rho}_s\right]. \tag{5.6}$$

Adjustments must be made because we are propagating a density matrix with four dimensions and the simple complex conjugate vector $\left|\chi_k^{(2)}\right\rangle$ cannot be utilised, so therefore a different form must be used. By expanding for $n = 2$, the successive linear equations to obtain a density matrix ρ'_k can be written as

$$(\hat{\mathcal{H}} - E_k + \sqrt{i}^3\epsilon)(\hat{\mathcal{H}} - E_k - \sqrt{i}^3\epsilon)(\hat{\mathcal{H}} - E_k + \sqrt{i}\epsilon)(\hat{\mathcal{H}} - E_k - \sqrt{i}\epsilon)\rho'_k = \epsilon^4\rho_s \tag{5.7}$$

$$P(E_k, n = 2, \epsilon) = \mathrm{Tr}(\rho_k^{'}) \tag{5.8}$$

In general, the amount of work necessary scales as $2^n/\epsilon$. Here ϵ should be chosen to be larger than the eigenstate spacing, to avoid inaccuracies or misleading results. Therefore the choice of ϵ depends on the size of the numerical grid too, since the grid size determines the energy eigenvalues. This approach of direct energy resolution of a density matrix has not been demonstrated before in literature, as far as this author's knowledge. The accuracy of the energy-resolved parameters as a result of using the window operator method is given in Chapter 6.

5.2 Summary

The window operator was a key energy-resolving method that allowed the calculation of energy-resolved fusion probabilities using the CCDM method. An introduction to the window operator equations is provided, along with a simplification that can be used when choosing $n = 2$ for a wave function. The adaptation of the window operator to a density matrix is discussed, and the successive linear equations that must be solved to obtain energy-resolved fusion probabilities are presented.

Chapter 6

Model improvements, features and verification

6.1 Optimising hardware usage

The consideration of numerical methods is essential for the efficient running of programs and this is particularly important for density matrix calculations. This is because, like many computational projects, the limiting factor is often computational run time and hence the complexity of the model must be appropriate for the current hardware and methods available.

Parallelisation of a program is one method of fully utilising the available hardware and can be implemented simply if only a few subroutines need to be parallelised. OpenMP parallelisation was used for the calculations in this work due to the simplicity of the implementation and the structure of the code. It must be said that parallelisation cannot be applied to the entire program and it should only be used where computationally beneficial. Parallel programming should be included in structures in the code that have significant run time, in excess of the overhead cost that comes with parallelisation due to the internal communication between threads of a CPU. In addition, it can only be applied to blocks of code where the outcome of one parallel process would not affect any of the others. Message passing interface (MPI) parallel programming was considered because of the ability to not only parallelise through nodes, but also benefit from distributed memory and the capability to run on heterogeneous systems — collections of processors with distinct architectures [110]. This allows for much better scaling than OpenMP. However, the current difficulty and length of the problem would make MPI parallelisation excessive, and the time spent on implementation may not even provide savings in execution time due to the overhead time spent communicating between processors.

After profiling the code using GPROF and finding the most time intensive subroutines (see Appendix C), the top subroutines that uses the largest proportion of run time of 32.07% is the `cdft` subroutine. This subroutine is necessary for the fast Fourier algorithm, and unfortunately it cannot be parallelised, since `cdft` is already simple and optimised. Hence, parallelising this subroutine would take longer due to the overhead associated with parallelisation. A similar problem occurs for the `fft` subroutine. Hence, the next clear choice for parallelisation was the `Liouvillian_operation` subroutine, the subroutine that calculates the density matrix using the Faber polynomial approximation for each time step. Parallelisation is applicable here since the calculations within each time step do not depend on previous calculations.

The overall time saving for a single run was $10-15\%$ depending on the system used. Should the run time become > 24 hours, it could become favourable to take another profile of the code and further parallelise the code using OpenMP or MPI techniques. It should be noted that MPI parallelisation has great synergy with high performance computing clusters (i.e. EUREKA, University of Surrey, UK) and these should be utilised to maximise the benefit from this method.

6.2 Methods used to improve the numerical calculations

Prior to this work, only the total summed fusion probability was calculated for an initial centroid energy E_0 of the propagating wave packet. For low energy nuclear fusion reactions, this meant that the higher energy plane waves within the wave packet dominated the fusion cross sections and information at energies below the Coulomb barrier was lost or intangible. With this new method, energy-resolved fusion probabilities can be calculated and this allows one to compare results against TISE calculations implemented within the `CCFULL` code [31] and ensure that the results at sub-barrier energies are correct. The ability to calculate energy-resolved fusion probabilities could also be useful to experimentalists who practically use mono-energetic beams, and these measured values can be compared to quantum model calculations.

As stated earlier, the window operator method requires the input of two variables, the energy bin width ϵ and the overlap parameter n. From initial tests, it was found that there was agreement of the energy-resolved fusion probabilities with `CCFULL` for values up to $E_{\text{c.m.}}/V_B > 0.9$. However, investigating deep-sub barrier energies would require agreement further below the barrier. This section describes the various techniques that were explored in an attempt to improve the agreement of our results over a larger range of $E_{\text{c.m.}}$.

6.2.1 Alternative method of calculating the transmission coefficient

Firstly, we examined the current method of calculating the fusion probability, which involves calculating the reflection coefficient and simply using the relation given in Eq.(6.1),

$$\mathcal{T}(E_k) = 1 - \frac{\mathcal{P}_{final}(E_k)}{\mathcal{P}_{init}(E_k)}, \tag{6.1}$$

where $\mathcal{P}_{init}(E_k)$ and $\mathcal{P}_{final}(E_k)$ are the initial and final energy-resolved wave packet amplitudes for $\{E_k\}$. This method is useful since it does not require use of additional variables to calculate the transmission coefficient, and the reflection coefficient is calculated as a ratio of the initial and final energy-resolved wave packet amplitudes. However, it was thought that this method of calculating the reflection coefficient could cause instability errors when the values were below 10^{-10}.

In an attempt to improve the calculation of the transmission coefficient, alternative methods of calculating energy-resolved transmission coefficients were investigated and the following equation from Ref. [111] was implemented,

$$\mathcal{T}'(E_k) = \frac{-(8/\hbar\nu_k)\,\epsilon^4\,\mathrm{Tr}\left[\hat{\rho}_s \cdot \mathrm{Im}(\hat{W})\right]}{\mathcal{P}_{init}(E_k)}, \tag{6.2}$$

where $\nu_k = \sqrt{2E_k/\mu}$ and $\mathrm{Im}(\hat{W}) < 0$ denotes a strong, imaginary Woods-Saxon potential used to remove probability from the density matrix.

This was used to successfully obtain energy-resolved transmission coefficients using the TDWP method. For the coupled-channels density matrix method, this method of calculating the transmission coefficients was unstable and the results were intangible. The instability is related to the resolution parameter being too small, therefore causing oscillations in the calculations. This transmission coefficient was successfully calculated in Ref. [111] due to the large grid size (1000 fm) and smaller grid spacing used, which was feasible since the TDWP method was used and fewer numerical restrictions on the grid size were in place. Therefore their energy eigenvalues (assuming a free particle in a radial box) were smaller and the energy resolution was sufficient, which was not the case for our calculations.

6.2.2 Extension of the grid size during the calculation of the energy-resolved probability

Through testing, it was shown that using a larger grid size for the whole time propagation of the density matrix was unfeasible numerically, as the computational run time in hours would increase by an order of magnitude. This prompted an attempt to expand the radial grid for the kinetic and potential energy operators only during the calculation of energy-resolved probability. To do this, the radial grid was increased to $300-500$ fm when applying the window operator to the final density matrix. The radial dimensions would then be larger and the energy eigenvalues (again assuming a free particle in a radial box) would be lower, so in theory a smaller energy resolution could be used.

After implementation, the run time increased significantly ($\approx 50\%$) and the energy-resolved fusion probabilities improved for higher energies but did not improve for deep sub-barrier energies. Despite the benefit of using a smaller energy resolution parameter, this extension does not increase the number of grid points where fusion takes place on the grid, and therefore the calculations involving the smallest probabilities did not improve.

6.2.3 Reduction in the size of the radial grid

It was initially thought that reducing the size of the radial grid would decrease the resolution available to the window operator and reduce the accuracy of the results, since the energy eigenvalues are dependent on the size of the system and ϵ would need to be increased for a smaller system. However, it was found that reducing the size of the radial grid from 250 fm to 150 fm but keeping the radial step size dr constant increases the number of grid points and improves the resolution. The radial energy eigenvalues are increased and therefore a larger value of ϵ must be used, but agreement of our results with TISE calculations at lower fusion probabilities can be reached with this smaller grid. However, there was a limit to the reduction of configuration space and decreasing the grid further led to problems assumed to be due to energy eigenvalues that are too large. In addition, the wave packet may interact significantly with the boundaries of the grid because the probabilities of either a minimum uncertainty Gaussian or Coulomb wave packet at the tail could be significant when confined to a smaller grid space causing unwanted effects.

6.3 Model verification results

6.3.1 Model parameters for ^{16}O + ^{144}Sm

The required parameters used to perform the calculations in this chapter are presented in Table 6.1. These parameters are used throughout this thesis unless otherwise stated. Table 6.2 gives the Woods-Saxon potential parameters used for the ^{16}O + ^{144}Sm collision.

6.3.2 Dynamics of the calculation

Previously, the dynamics of the calculations were shown in two dimensions in Fig.4.4, and snapshots of the radial wave packet at key points in time were shown. This can be further developed by including all times within the propagation to understand the variations in wave packet amplitudes for any of the states within the reduced system. This is shown in Fig.6.1, for the elastic and inelastic (3^-, 1.81 MeV) channels of ^{16}O + ^{144}Sm. The ability to follow the dynamics across the whole time propagation is a useful tool to ensure

Table 6.1: The general parameters used for the numerical calculations for the test case collision ^{16}O + ^{144}Sm. These are subsequently used in all other calculations throughout this work unless specifically stated otherwise.

Parameter	Value	Description
N	1024	The number of radial grid points
i	2	The number of states
k_{env}	1	The number of environment states
r_{min}	1.5 fm	Minimum value of the radial grid
r_{max}	150 fm	Maximum value of the radial grid
r_0	70 fm	Initial position of wave packet
σ_0	10 fm	Typical spatial dispersion of wave packet
Δt	1×10^{-22} s	Time step used in propagation
W_{fus}	50 MeV	Γ decay function height
r_{fus}	1.1 fm	Γ decay function radius empirical constant
a_{fus}	0.3 fm	Γ decay function diffusivity

that couplings between states are correctly implemented, and the fusion environment is functioning correctly, i.e., the wave packets are not radially localised beyond the Coulomb barrier. It is worth mentioning that the 2D time propagation figure is still a useful tool since a better view of the wave packet shape can be seen, and it is easier to compare the magnitude of the initial and final wave packets.

6.3.3 Energy-resolved fusion probabilities for ^{16}O + ^{144}Sm

Fig. 6.2 shows the fusion probabilities calculated using optimal initial conditions for the Gaussian and Coulomb wave packets for the test case collision ^{16}O + ^{144}Sm. The height of the Coulomb barrier between these two nuclei is 61.1 MeV, and this was calculated using the São Paulo potential [112]. By adjusting the Woods-Saxon parameters, the Coulomb barrier height of $\hat{U}$ was matched to this value, while retaining an ideal potential shape.

The single channel calculations show the impact of including coupled-channels into the calculations. The difference arises from the apparent distribution of fusion barriers [12] that

Table 6.2: The Woods-Saxon parameters used for the numerical calculations for the ^{16}O + ^{144}Sm collision.

Parameter	Value	Description
V_{WS}	-105.1 MeV	Woods-Saxon potential well depth
r_{WS}	1.1 fm	Woods-Saxon nuclear radius empirical constant
a_{WS}	0.75 fm	Woods-Saxon diffuseness parameter

is created from the coupling between the radial motion and intrinsic nuclear excitations. In turn this increases fusion probabilities as the total potential barrier will be lower for some inelastic channels of the interacting nuclei [11, 12]. Fusion probability is the quantity of choice to display our results instead of fusion cross sections, since cross sections are dependent on the projectile and target of the system and are less comparable between different systems of collision partners.

The Gaussian wave packet calculations clearly provide the best results in terms of energy-resolved fusion probability at deep sub-barrier energies ($E_{\mathrm{c.m.}}/V_B < 0.9$), where they are convergent with the CCFULL calculations to an order of magnitude of 10^{-8}. Having accurate values of fusion probability for low-energy fusion reactions allows us to extend the scope of our calculations and validate interesting effects in these low fusion probability regions. The Coulomb wave packet does not reach the same order of magnitude as the Gaussian wave packet, but the results are reasonable up to $\approx 10^{-6}$, and the broadness of this wave packet in momentum space allows a better global description of energy values near and above the barrier ($E_{\mathrm{c.m.}}/V_B > 0.9$). This could be useful for reducing computational run times if the lowest probability values are not important. Furthermore if the energy-resolved fusion probabilites are unstable, the Coulomb wave packet is more reliable and more likely to give a larger set of accurate results. The calculated points with physical meaning in Fig. 6.2 are the invariant values when the initial mean energies E_0 are changed. The probabilities that lie outside of the trend are likely because of the small error associated with the window function, and are numerically inaccurate.

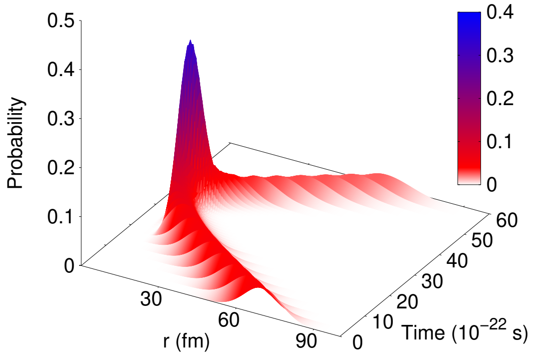

(a) Elastic channel

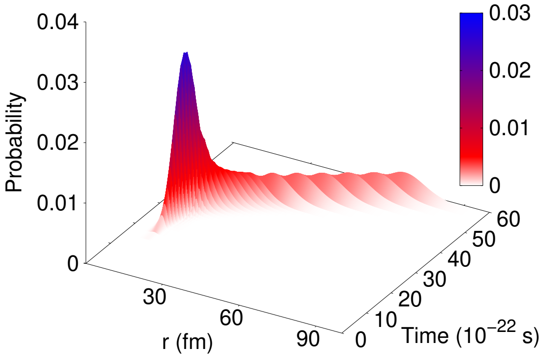

(b) Inelastic channel

Figure 6.1: Radial position probability as a function of internuclear radius and time for a head-on collision of ^{16}O + ^{144}Sm with a mean energy of 60 MeV. The radial probability decreases and increases for (a) the elastic and (b) inelastic channels respectively, as the nuclei approach their Coulomb barrier (r $\approx$ 10 fm). For visualisation, when the mean radius is larger than 20 fm, the time step is 3×10^{-22} s.

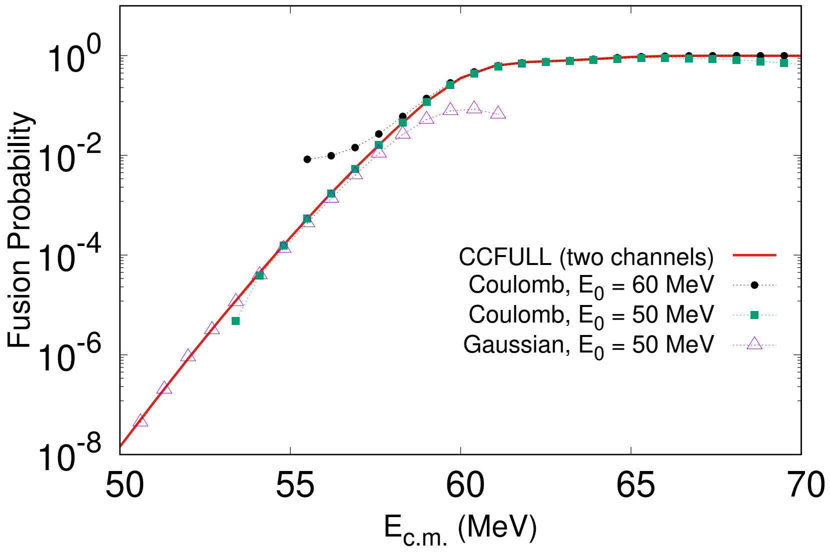

Figure 6.2: The energy-resolved fusion probabilities from the CCDM method for different initial wave packets for a head-on collision of ^{16}O + ^{144}Sm for a range of $E_{c.m}$ values above and below the Coulomb barrier. These probabilities are compared with those from `CCFULL` [31], which were benchmarked by experimental data for this collision [13]. The `CCFULL` results (solid red line) are reproduced by the CCDM method (symbols).

6.3.4 Entropy, energy dissipation and purity

An additional benefit of using a quantum dynamical model is the ability to calculate quantum properties of the heavy-ion collision. These quantities are useful to understand the validity of the model, confirm expected phenomena and help us establish relationships between the calculation outcomes and fundamental quantum mechanical properties.

The von Neumann entropy of a state expresses the degree of 'mixing'. It is the quantum analogue to Gibb's entropy from classical statistical mechanics. The von Neumann entropy is a useful quantity to calculate because it offers us information about the disorder in the system of interest, and with the quantum dynamical model used we are able to sample this at any time step within the propagation. Additionally, from the second law of thermodynamics, we know that the entropy of an isolated, physical thermodynamic system cannot decrease. Calculating the von Neumann entropy of the reduced density matrix has provided some indication of the correctness of the underlying quantum physics of the theoretical framework. The dynamics of quantum coherence can be described by the time-dependent purity, $\mathcal{P}(t)$ and the von Neumann entropy, $\mathcal{S}(t)$, in the reduced-system density matrix, $\rho_s(t) \equiv \{\rho_{ij}^{rs}\}$ given in Eq.(4.12),

$$\mathcal{P}(t) = \mathrm{Tr}\left[\rho_s^2(\mathrm{t})\right], \tag{6.3}$$

$$\mathcal{S}(t) = -\mathrm{Tr}\{\rho_s(\mathrm{t})\ln[\rho_s(t)]\} = -\sum_j \eta_j(t)\ln[\eta_j(t)], \tag{6.4}$$

where $\eta_j(t)$ are the eigenvalues of $\rho_s(t)$, and $\rho_s(t)$ is normalised to unity when calculating these physical quantities.

Fig. 6.3 displays the dynamics of energy dissipation and entropy production for the collision scenario shown in Fig. 6.1. The energy loss is determined by the change of the average energy of the reduced system relative to its initial value, i.e., $E_0 - \mathrm{Tr}\left[\hat{H}_S\rho_S(t)\right]$. It is interesting to observe that the transient, strong interaction of the reduced system with the fusion environment makes the dynamics dissipative and decoherent (the entropy increases and the purity of the reduced-system density matrix decreases) as shown in Fig. 6.4. When the nuclei re-separate, there is a revival of quantum coherence and, asymptotically, the elastic and inelastic channels move in a coherent superposition. A question that comes to mind: Does the transient decoherent phase of the collision affect the fusion probability?

Since CCFULL does not include decoherence, these results indicate that the transient quantum decoherence caused by the fusion environment localised in the nucleus-nucleus potential does not affect fusion probability. The change in purity in Fig. 6.4 (Lindblad) is caused by the effect of the irreversible coupling between the fusion environment and the reduced system. Without the fusion environment, the dynamics of the CCDM model would be Hamiltonian, and would preserve energy, entropy and the purity of the reduced density matrix.

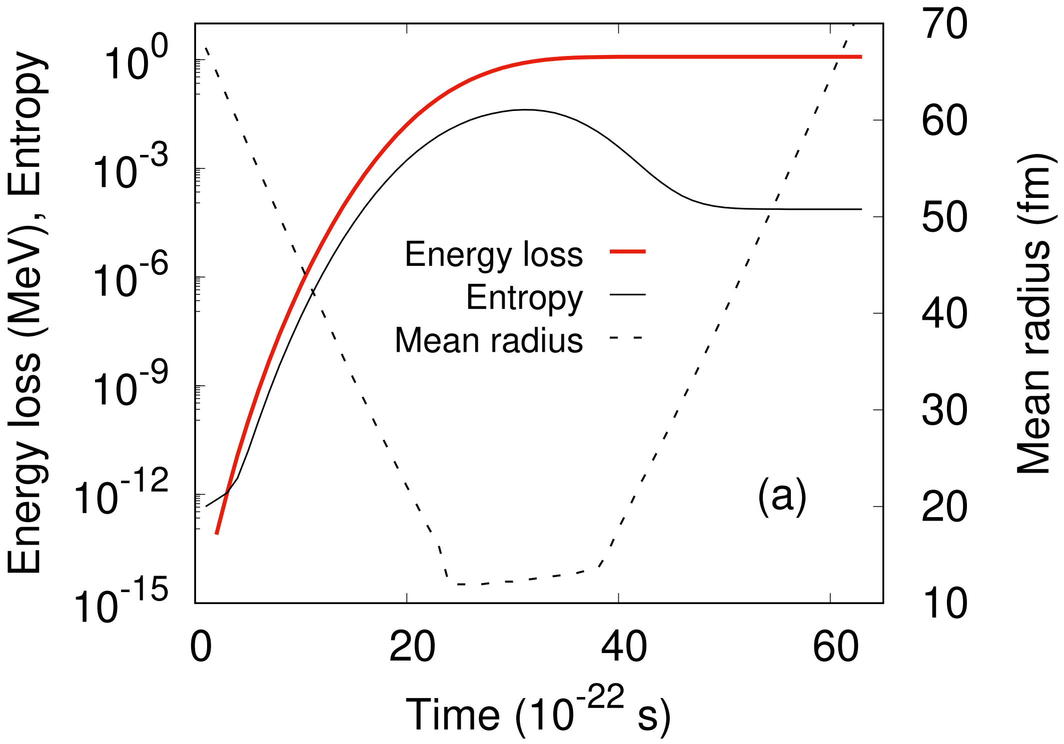

Figure 6.3: The evolution of energy dissipation and entropy during the collision dynamics for ^{16}O + ^{144}Sm. The energy loss (thick solid red line) and entropy (thin solid black line) increase as the nuclei approach their Coulomb barrier, and reach a plateau as the nuclei reseparate. The dotted black line shows the average internuclear radius of the reduced system.

6.4 Model error analysis

Evaluating the errors of a model is essential to understand abnormalities in results, and to ensure the validity of the method. For the error analysis of the Faber propagator, we use Eqs. (3.11) and (3.12) as discussed in Chapter 3. These are the Frobenius norm and local error co-efficient respectively, and the final values for these quantities after using $n = 470$ polynomials for each time step in the calculations are shown in Fig. 6.5 for ^{16}O + ^{144}Sm.

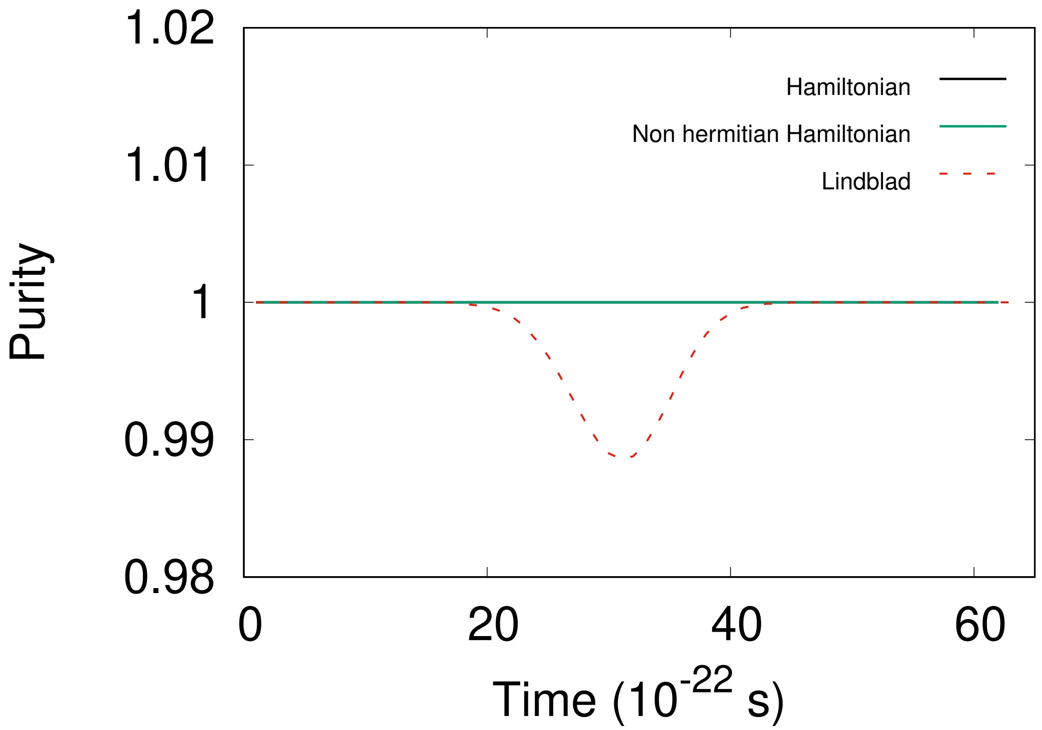

Figure 6.4: The comparison of purity in three different calculations for ^{16}O + ^{144}Sm. The solid black line is calculated using Hamiltonian dynamics with no dissipation, the solid green line is calculated using a non hermitian Hamiltonian, in which an imaginary potential is used to remove flux from the wave packet. Lastly the Lindblad dynamics, which is used in this work, is represented by the dashed red line and shows decoherence as the relative position of the nuclei approach the Coulomb barrier. There is a resurgence of coherence as the nuclei reseparate and the interaction with the fusion environment diminishes. Asymptotically, the elastic and inelastic channels evolve in a coherent superposition.

At the beginning and end of the calculations, the Frobenius norm and local error are stable. It is clear that there is a very minimal increase when the propagation time approaches 35×10^{-22} s, this is the period where the nuclei are localised around the Coulomb barrier. For these calculations, it was found that the local error was stable below 1×10^{-27} and the Frobenius norm should be of the order of unity. Both of these criteria were satisfied for these calculations, and subsequent calculations showed a similar or lower order of error.

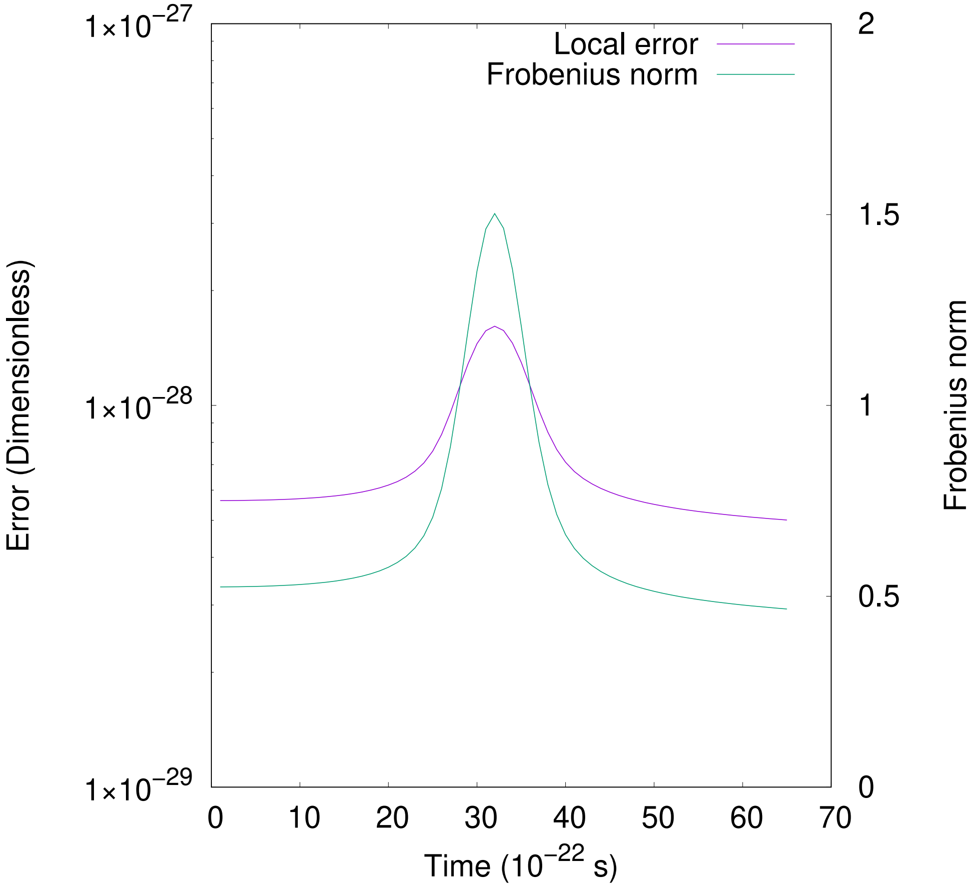

Figure 6.5: The local error, $\epsilon_{loc}(k)$ and Frobenius norm. The local error gives an indication of difference between the polynomial of degree k and exact solution. A stable value for the local error across the entire propagation is shown.

6.5 Summary

The strong agreement between the CCDM and CCFULL calculations demonstrates the reliability of the CCDM approach and shows that it can be successfully used for describing low-energy heavy-ion reactions. The application of the window operator was applied to a density matrix for energy resolving purposes and was crucial for validating the treatment of fusion using the CCDM method. Unexpectedly, the transient decoherence within the fusion pocket does not affect the fusion probability [52]. This method has the advantage of allowing us to study quantities throughout the time propagation of the density matrix, such as coherence dynamics, energy dissipation and entropy. Additionally, we confirm that the formation of a compound nucleus can be represented as an environment as part of the open quantum systems methodology. This chapter sets the foundations for further work such as the involvement of physical environments or couplings to the internal structure of colliding nuclei in the following chapters.

Chapter 7

The effects of plasma on heavy-ion fusion reactions

On Earth, experimental nuclear reactions are often conducted in a vacuum, without an environment. During nucleosynthesis in stars, this is not the case; the fusion reactions take place within a dense, particle-rich plasma. Therefore it is unjustified to assume that the information obtained by experimental reactions conducted in a laboratory setting provide a realistic approximation to stellar environment reactions. In nature, nuclear fusion reactions take place only in hot, dense environments containing a mixture of ions and electrons. These environments are often referred to as high energy density plasmas (HEDPs). These environments are complex and the exact influence on fusion reactions is unknown due to the difficulty of performing experiments under these conditions, and microscopic model calculations are currently impossible due to the many degrees of freedom involved. Hence the CCDM model is employed to provide an intuitive platform for describing the effects of HEDPs on heavy-ion fusion.

We begin with an initial analysis of the well-known plasma effects to understand how fusion reactions are affected by plasma at various temperatures and pressures. In the literature, the primary effects of a plasma on nuclear reactions are said to be dominated by either Coulombic or thermal effects. A first order approximation of their relative importance can be carried out by calculating a Coulomb parameter, Λ, which is essentially a ratio between Coulomb and thermal energies [113–115],

$$\Lambda \equiv \frac{\langle Z_i e\rangle^2}{a_i \mathcal{T}}, \tag{7.1}$$

where $\langle Z_i e\rangle$ is the average ion charge in the plasma, a_i is the average inter-ionic distance and $\mathcal{T}$ is the temperature in MeV. When $\Lambda \ll 1$, the Coulomb energy is insignificant to thermal energy and a Debye-Hückel potential is assumed [116], and for $\Lambda \gg 1$, the Coulomb energy dominates the plasma interaction, and this regime is modeled with an ion-sphere potential. The outcome of a modified version of Eq.(7.1) is given in Section 7.3.

For the calculations in this chapter, a few assumptions were made of the plasma. The plasma is initially in thermal equilibrium and the excited states are populated before the target and projectile interact, due to the long lifetime of the plasma compared to the time of the heavy-ion collision [117, 118]. The plasma temperature and density do not change over the course of the reaction. In open quantum system terms, the plasma is considered a bath and the reduced system does not affect its properties. Temperatures of HEDPs vary between a few eV to a few MeV, and this leads to a wide range of interactions that can alter the outcomes of nuclear collisions. In this work, plasma temperatures around $100-500$ keV are used, which is typical for explosive astrophysical scenarios [119]. The plasma density range was chosen as $(10-10^5$ gcm$^{-3})$. Although there is scope to increase the density to extreme environments such as the crust of a neutron star $(10^8$ gcm$^{-3})$, this is much more complicated since the electrons in the plasma would be highly degenerate and relativistic effects would certainly be non-negligible. For Coulomb screening effects, a choice of the plasma constituents must be made, and this is further discussed in Section 7.3.

Then the lesser-known effects from nuclear plasma interactions (NPIs) were implemented. The term NPIs refers to all the atomic process that can excite or de-excite nuclei. From literature, there are two NPIs that are of interest: nuclear excitation by electron capture (NEEC) or transition (NEET) [120–122]. It is expected that these are likely to change reaction cross sections in HEDPs [123, 124]. One of the purposes of this work is to estimate the contribution that these NPIs have in heavy-ion fusion reactions. The strength of the NPIs are dependent on the plasma conditions, and this will change the excitation and de-excitation rates.

The purpose of this chapter is to review the processes in which a plasma environment can impact a fusion reaction, identify if particular effects of a plasma environment affect fusion probabilities, and to demonstrate that the magnitude of these effects can be quantified. This work builds upon the foundations of the CCDM model, and if it is evident that the effects are significant, then a comprehensive study that includes a list of strong candidate nuclei and known nuclear excited states would be the natural progression to determining the overall effect of HEDPs on stellar fusion reaction rates.

7.1 A note on the target and projectile choice

For plasma effects to be effective, the system must include low-lying excited states, typically below 1 MeV. Although this limits the number of relevant fusion reactions since excited states in the nucleus are typically in the MeV range, the summed effect of all relevant fusion reactions could have a significant impact on fusion reaction rates in stellar environments. Initially, the nucleus of choice to test plasma effects on heavy-ion fusion was ^{237}U. This nucleus has an extremely low nuclear first excited state of 11.5 keV and it is expected that this target nucleus would produce the most pronounced effects for a ground state nucleus. Unfortunately, the required information for the model is not publicly available due to the use of uranium for energy and defence purposes [125]. Additionally, the CCDM model is designed to handle rotational and vibrational excited states, and this requires the use of even-even nuclei.

Hence a ^{188}Os target nucleus is used due to its low-lying 2^+ rotational excited state at 155 keV [126] and a ^{16}O projectile nucleus that has a high 6.13 MeV first excited state. This simplifies the calculations, since the oxygen projectile can be considered inert. The ^{188}Os nucleus has further excited states, as shown in Fig.7.1, but these are ignored since couplings to these channels will be weaker than for the first excited state, and extra channels will increase the computation time significantly as explained in Chapter 3. Therefore we only consider the ground state of ^{16}O and the ground and first excited state of ^{188}Os, and this calculation will serve as a first order approximation.

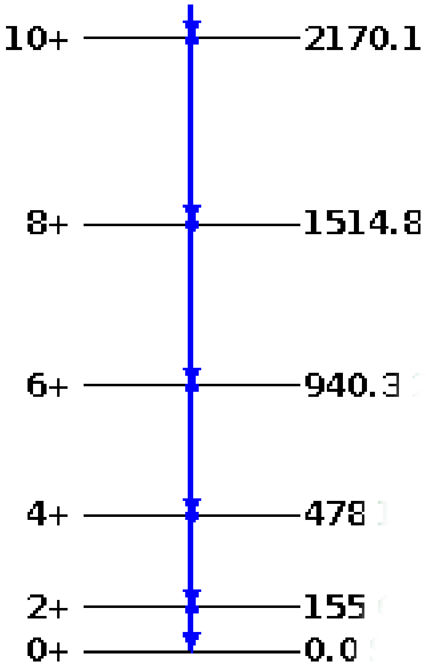

Figure 7.1: A partial ^{188}Os level scheme, showing the ground state rotational band and the respective energy levels in keV. Figure adapted from [127].

7.2 Model parameters for ^{16}O + ^{188}Os

The model parameters for the calculations in this chapter are the same as those in Section 6.3.1. The Woods-Saxon parameters required for the ^{16}O + ^{188}Os collision are given in Table 7.1.

7.3 Coulombic effects

Coulombic effects in a plasma are related to the effective electron screening of the positive target nucleus charge from the incoming projectile nucleus. An overly simplified picture of this is given in Fig.7.2.

For the high temperatures within stars, the atoms are almost completely stripped of their atomic electrons and hence it would be simple to assume that electron screening does not affect nuclear reactions in stars. In fact, the plasma surrounding the nuclei contains a sea of free electrons, in which their arrangement changes depending on the strength of the

Table 7.1: The Woods-Saxon parameters used for the numerical calculations for the ^{16}O + ^{188}Os collision.

Parameter	Value	Description
V_{WS}	-60.64 MeV	Woods-Saxon potential well depth
r_{WS}	1.2 fm	Woods-Saxon nuclear radius empirical constant
a_{WS}	0.63 fm	Woods-Saxon diffuseness parameter

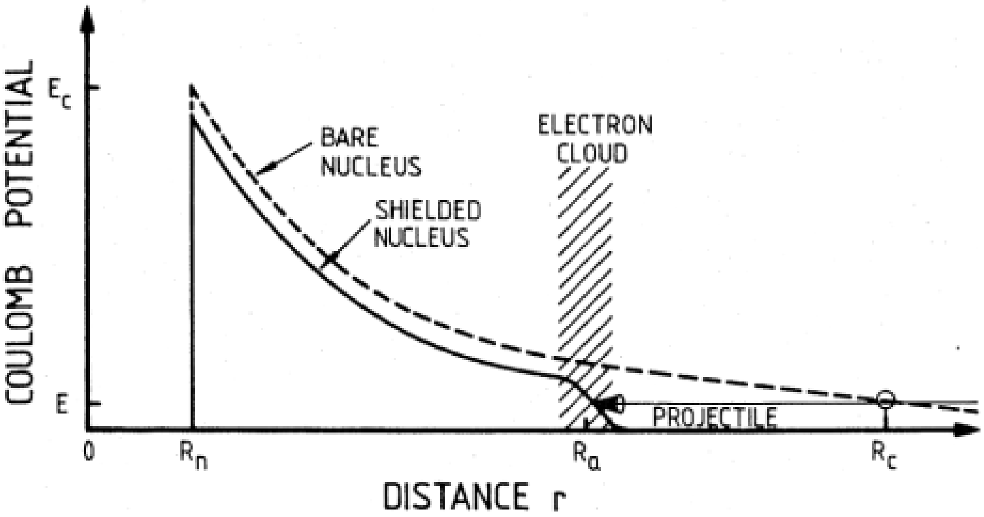

Figure 7.2: An ideal and simplified picture of Coulomb screening, showing an electron cloud reducing the Coulomb potential of a bare nucleus. E_c is the Coulomb potential, and E is the initial energy of the projectile. R_n is the nuclear radius, R_a is the atomic radius and R_c is the classical turning point. Figure from Ref. [116].

screening regime determined in Eq.(7.1). For the weak-screening regime, where temperature is high and/or the density is low, the electrons surround nuclei at the Debye-Hückel radius,

$$R_D = \left(\frac{kT}{4\pi e^2 \rho N_A \xi}\right)^{1/2} \tag{7.2}$$

here $\xi = \sum_i (Z_i^2 + Z_i)\frac{X_i}{A_i}$, where the sum is over the all positive ions and X_i is the mass fraction of each nuclei within the plasma. It is worthy noting that there are many assumptions and conditions that must be fulfilled for this theory to be valid. Firstly, this model for electron screening is based on classical theory, and hence there is a minimum value of r_{min} that is required so that the uncertainty principal is not invalidated. By relating r_{min} to the uncertainty energy, an approximation to the correctness of this theory can be made, as long as the uncertainty energy is small compared to the mean thermal energy of the electrons. It is also assumed that the stellar gas is 'nearly perfect' [116], which leads to the assumption that electrons surround the nuclei in spherical shells.

For the system of nuclei we are investigating, we must choose how to interpret the distribution of mass and charge within the plasma. Since we are using ^{16}O and ^{188}Os as the collision partners, the approximation of a nucleus with large charge and low abundance can be used. Then $Z_1 = 76$ is the charge of ^{188}Os, $Z_2 = 8$ is the charge of ^{16}O and z is the average charge of the plasma, which we can take as either the charge of ^{4}He or ^{16}O. When $Z_1 \gg Z_2$, it can be assumed that only the charge cloud around the much larger nucleus needs to be taken into account [113]. Additionally, the charge cloud around radius R_1 can be assumed constant during a nuclear collision. The low abundance of Z_1 means the distance between these nuclei should be large compared to their charge cloud, and hence only the charge cloud of one nucleus needs to be considered.

We can use another parameter that has a very similar form to Eq.(7.1) to determine the expected strength of screening effects for this special case of plasma,

$$F = \frac{Z_1 z e^2}{R_z kT}, \tag{7.3}$$

where R_z is the Debye radius calculated using only the average charge of the plasma z. When $F \ll 1$, weak screening approximations should be used, and when $F \gg 1$, strong screening approximations should be used. The intermediate region must be approximated between the two screening regimes [113].

Taking the most extreme case, where $z = 8$ and Z_1 and Z_2 are defined above and using the lowest considered temperature in the calculations (100 keV), the maximum effect of electron screening in this approximation is given in Table 7.2. In this case, the plasma screening effects are weak or intermediate until a density of 10^5 g/cm^3, where they become significant relative to the thermal energy. Although Coulomb screening effects could be significant at high, non-degenerate densities for the projectile and target used, these estimates are exaggerated and attempt to maximise the screening effects. Since the conditions stated are ideal for screening, and the effects are in general insignificant, the Coulomb screening effect at these densities are not included in the present calculations.

Table 7.2: A table of maximum values of the F parameter using an extreme environment assuming a plasma consisting of mainly ^{16}O with small amounts of ^{188}Os, for non-degenerate plasma densities.

	Density (g/cm^3)				
Temperature	10	10^2	10^3	10^4	10^5
100 keV	0.0452	0.143	0.453	1.43	4.53

An extensive inclusion of electron screening would include higher density effects such as ion-ion and ion-electron correlations within degenerate electron liquids [114,128], and relativistic effects such as pair production at high temperatures (≈ 1 MeV or higher). The complexity of these effects are better reserved for a comprehensive study solely focused on electron screening and hence they are not elaborated on further in this work. For interested readers, reviews on weak- and strong-screening regimes in HEDPs can be found in Refs. [5,129,130].

7.4 Thermal effects

The temperature of plasma has been known to contribute to stellar nuclear fusion for many years, and this led to many great discoveries and foundations in nuclear astrophysics such as the Gamow window, known to be the region of overlap between the Maxwell-Boltzmann distribution and the rate of quantum tunneling for a system of colliding nuclei at a particular temperature [131]. This was without a doubt, a major discovery due to the understanding that fusion reactions that happen within this window are likely to contribute to stellar fusion reaction rates.

Since then, additional knowledge of environmental temperature effects have not progressed much and the effect of HEDP temperature on fusion reactions has been limited to the thermal distribution of collision energies within stellar environments, and how these directly affect thermonuclear reaction rates [132]. Something that has not been investigated in detail is the presence of low-lying nuclear excited states in heavy-ion fusion reactions that can be populated in these HEDP environments. One case where the thermal population of low-lying excited states has been previously studied was in neutron capture studies using the Hauser-Feshbach statistical model [133,134]. The neutron cross sections were weighted with temperature-dependent population probabilities of the target's excited states, leading to a stellar enhancement factor. However, these effects have been ignored in heavy-ion fusion studies so far and hence it is the focus of this work.

To implement thermal effects into the model, we introduce Boltzmann factors, w_α, into the initial density matrix [55],

$$\rho^{rs}_{\alpha\alpha}(t=0) = w_\alpha \left|r\right\rangle \left\langle s\right| , \tag{7.4}$$

where $|r\rangle$ refers to a Gaussian or Coulomb wave packet describing the internuclear motion on a radial grid [54], and the density matrix is diagonal in the energy eigenstate basis, denoted by $|\alpha\rangle$. The initial population of the energy eigenstates is given as,

$$w_\alpha = \frac{(2I_\alpha + 1)\exp\left\{-\dfrac{e_\alpha}{\mathcal{T}}\right\}}{\displaystyle\sum_{\alpha'=1}^{N} (2I_{\alpha'} + 1)\exp\left\{-\dfrac{e_{\alpha'}}{\mathcal{T}}\right\}} . \tag{7.5}$$

where $2I + 1$ is the spin degeneracy factor. The present calculations only include excited states of the ^{188}Os ground-state rotational band, and hence the spin degeneracy factors are not necessary for the following calculations due to the the use of the isocentrifugal approximation, which does not consider the Coriolis interaction.

Excited states are thermally populated before the target and projectile interact with each other and thermodynamic equilibrium is assumed at $t = 0$. As known from coupled-channels calculations, coupling of the radial motion to energy eigenstates can cause changes in fusion probability. Population of excited states in either the target or projectile nucleus due to surface vibrations or rotational excited states lead to an overall increase in fusion probability due to coherent coupled-channels effects [11].

7.4.1 Fusion probability results and analysis for ^{16}O + ^{188}Os

We construct the coupled-channels fusion probability of a zero temperature, environmentless fusion reaction for an inert ^{16}O projectile and ^{188}Os target with two states (ground and first excited state), given in Fig. 7.3. Multiple wave packets with different initial mean energies (E_0) were used to check that the results converge [54]. This serves as verification of the method and a baseline that allows us to measure the thermal effects of the plasma.

To isolate the effects of temperature on fusion probability, the increase in energy-resolved fusion probability was calculated using the ratio between coupled-channels calculations at either $\mathcal{T} = 0.1$ MeV or $\mathcal{T} = 0.5$ MeV and $\mathcal{T} = 0$ MeV, shown in Fig. 7.4. The fusion probability was calculated by taking the average energy-resolved fusion probability for initial wave packets with varying E_0. For $\mathcal{T} = 0.1$ MeV, the green (square) points were calculated using a Gaussian wave packet with $E_0 = 60$, 63, 65, 67 and 70 MeV, and the blue (circle) points were calculated using a Coulomb wave packet with $E_0 = 65$, 67 and 70 MeV. The same method was used for both $\mathcal{T} = 0$ and $\mathcal{T} = 0.5$ MeV. The error bars are relative errors, due to statistical uncertainties associated with the differences in fusion probability at each value of E_0. Error propagation was used to ensure the resulting error bars considered the error from both the baseline calculations and the calculations with temperature.

We use a Gaussian wave packet for its accuracy at deep sub-barrier energies compared to a Coulomb wave packet. However, a Coulomb wave packet offers a better global description of fusion probability around and above the Coulomb barrier, as discussed in Ref. [54]. Below the Coulomb barrier, the average increase in fusion probability was 15.5% and 36.9% for the

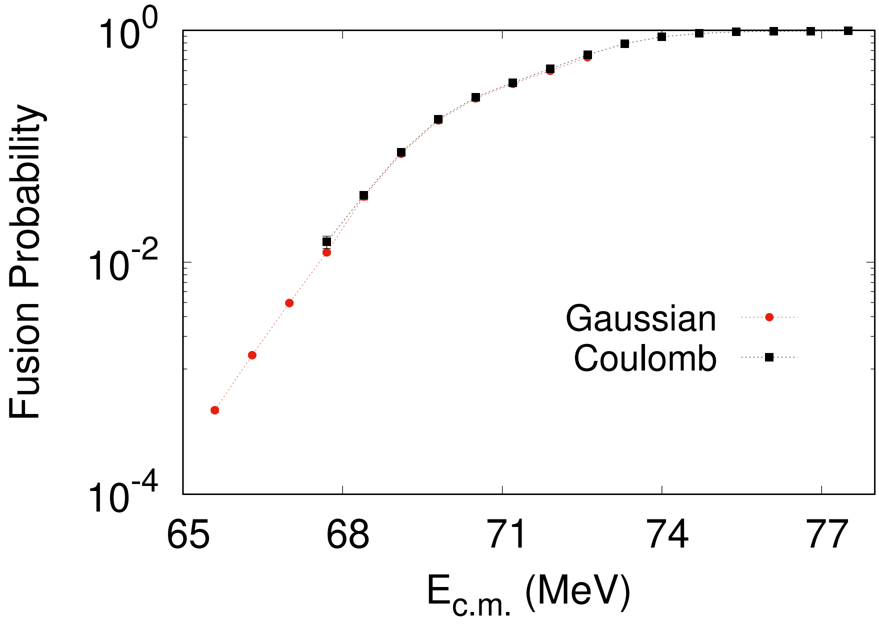

Figure 7.3: A construction of the energy-resolved fusion probability for a ^{16}O projectile and ^{188}Os target with coupled-channels but without a plasma environment ($\mathcal{T} = 0$ MeV). Gaussian and Coulomb wave packets are used, taking the average energy-resolved fusion probability for a range of incident mean energies, E_0. Error bars due to statistical error are included but most are insignificant. The nominal Coulomb barrier between these nuclei is 71.7 MeV.

0.1 MeV and 0.5 MeV temperatures respectively. Above the Coulomb barrier, the increase quickly diminishes to a few percent.

The results in Fig. 7.4 are an advancement on work that showed that sub-barrier fusion is enhanced when channel couplings are included, due to the fusion contribution of excited states [135]. The thermal increase in fusion probability can be explained by studying the initial density matrix of the entrance channel,

$$\rho_0 = (1 - w_2) \left|\psi_1\right\rangle \left\langle\psi_1\right| + w_2 \left|\psi_2\right\rangle \left\langle\psi_2\right|, \tag{7.6}$$

where $\left|\psi_1\right\rangle \left\langle\psi_1\right|$ and $\left|\psi_2\right\rangle \left\langle\psi_2\right|$ are the pure state density matrices of the ground state and excited state respectively. The excited state Boltzmann factor calculated in Eq. (7.5) is

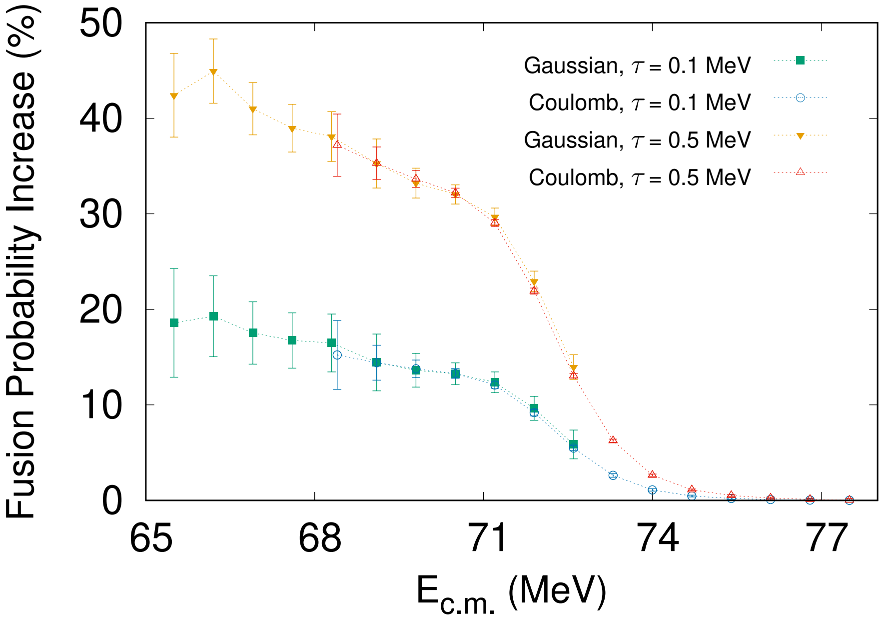

Figure 7.4: The increase in fusion probability for a ^{16}O projectile and ^{188}Os target due to the presence of a thermal plasma environment. For each temperature ($\mathcal{T}$ = 0.1 MeV and 0.5 MeV), the fusion probability increase is calculated using the ratio of averaged thermal environment calculations to averaged baseline calculations with no environment (Fig. 7.3). For the Gaussian wave packet, calculations were initiated with $E_0 = 60$, 63, 65, 67 and 70 MeV and for the Coulomb wavepacket, $E_0 = 65$, 67 and 70 MeV.

denoted by w_2 and this probability corresponds to a statistical ensemble of states. Two effective Coulomb barriers are created from a linear combination of two dynamically coupled state vectors, $|\psi_1\rangle$ and $|\psi_2\rangle$, as shown in Fig. 7.5.

The decoupled symmetric and anti-symmetric eigenchannels, $|\chi_{s,a}\rangle$, are defined as,

$$|\chi_{s,a}\rangle = \frac{1}{\sqrt{2}} \left(|\psi_1\rangle \pm |\psi_2\rangle\right) . \tag{7.7}$$

The height of the Coulomb barrier for the symmetric eigenchannel ($|\chi_s\rangle$) is significantly smaller than that of the anti-symmetric eigenchannel ($|\chi_a\rangle$), leading to an increase of the fusion probability relative to a single channel calculation involving the state $|\psi_1\rangle$ only.

Temperature affects the fraction of the eigenchannels contained in the entrance channel

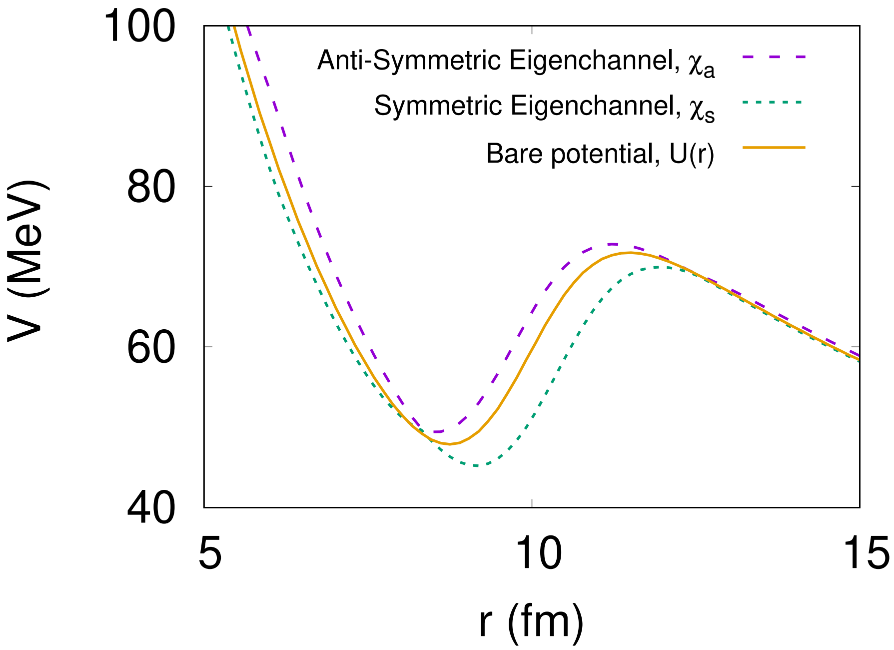

Figure 7.5: The Coulomb barriers of the decoupled eigenchannels. The symmetric barrier is the lowest, dominating the fusion process at energies below the nominal, 71.7 MeV Coulomb barrier of the bare potential, U(r).

configuration in Eq. (7.6),

$$\rho_0 = \frac{1}{2}\Bigg[|\chi_s\rangle \langle\chi_s| + |\chi_a\rangle \langle\chi_a| \Bigg] + \left(\frac{1}{2} - w_2\right) \cdot \Bigg[|\chi_a\rangle \langle\chi_s| + |\chi_s\rangle \langle\chi_a| \Bigg]. \tag{7.8}$$

In Eq.(7.8), ρ_0 represents the thermal ensemble in a mixed state. In a scenario where temperature is zero ($w_2 = 0$), fusion has an equal probability of occurring quantum mechanically (where the symmetric and anti-symmetric states are superimposed) as it does occurring in both of the symmetric and anti-symmetric channels and therefore it is affected by their interference. On the other hand, if temperature is infinite (i.e., $w_2 = 1/2$) then fusion will occur with equal probability (50%) in either the symmetric or anti-symmetric channel, without interference effects. From this deduction, the increase in temperature destroys the interference term and leads to a higher contribution of the symmetric channel – with its lower Coulomb barrier – to the average fusion probability of the initial thermal ensemble. The effect is more prominent with increasing temperature, which is supported by our results in Fig. 7.4

7.5 Atomic effects

The idea of the internal inverse electron conversion process was first published by Goldanskii and Namiot [136] regarding the isomer excitation of ^{235m}U, whereby the temperature of a plasma around the $50 - 100$ eV range should be able to populate the ^{235m}U isomeric state of 73 eV. Soon after, an improved approach was published and changes to nuclear excitation rates due to high temperatures was suggested by Doolen [137]. They investigated the changing lifetimes of nuclei due to the population of their nuclear excited states, and introduced both the equilibrium population of a nucleus with a ground state and first excited state and the inverse internal conversion process which is now referred to as nuclear excitation by electron capture (NEEC). NEEC is a resonant process where a free electron is captured into a bound atomic state and the difference between the kinetic energy and binding energy of the electron causes an excitation in the nucleus. Following the work by Doolen, further studies have been conducted to explore nuclear excitation effects via atomic processes in detail. When nuclear excited states exist slightly above an isomeric state, the nuclear excitation from atomic processes can cause an excitation to the higher energy level and subsequently decay to the ground state [138, 139]. This effectively enhances the decay rate of the isomer. These atomic interactions with a nucleus are called nuclear plasma interactions (NPIs).

Since these NPIs are capable of increasing the population of low-lying nuclear excited states in dense astrophysical plasmas [124], there is an interesting opportunity to investigate whether there are any changes to the fusion probability of heavy-ion fusion reactions due to these effects. NPIs are included in the calculations by introducing new Lindblad operators into Eq.(4.13),

$$\Gamma_{12}^{rr} = \gamma_{12}, \tag{7.9}$$

$$\Gamma_{21}^{rr} = \gamma_{21}, \tag{7.10}$$

where γ_{12} and γ_{21} are the respective excitation and de-excitation rates between the ground state and first excited state of ^{188}Os. These rates are dependent on the temperature and density of the plasma. Relevant excitation and de-excitation rates for this work are shown in Table 7.3, and were calculated using the ISOMEX code [138], which is based on the relativistic average atom model and assumes local thermal equilibrium for the electron and photon populations. The considered excitation processes due to NPIs are: resonant photon absorption, inelastic electron scattering, NEEC and NEET. The de-excitation processes include spontaneous photon emission, induced photon emission, internal conversion, bound internal conversion (BIC) and superelastic electron scattering. Since the 155 keV excited state of ^{188}Os is much greater than the binding energy of the K-shell atomic orbitals, NEET and BIC do not contribute to the plasma induced nuclear transition rates.

Table 7.3: Excitation (γ_{12}, left column) and de-excitation (γ_{21}, right column) rates for NPIs between the ground state and first excited state of a ^{188}Os nucleus for different temperatures and densities, calculated using the ISOMEX code [138].

Density	$\mathcal{T} = 0.01$ MeV	$\mathcal{T} = 0.1$ MeV	$\mathcal{T} = 1$ MeV
10 g/cm^3	$6.0 \cdot 10^2$ / $6.5 \cdot 10^8 \mathrm{s}^{-1}$	$7.3 \cdot 10^8$ / $6.9 \cdot 10^8 \mathrm{s}^{-1}$	$1.6 \cdot 10^{10}$ / $3.8 \cdot 10^9 \mathrm{s}^{-1}$
10^3 g/cm^3	$7.0 \cdot 10^2$ / $7.6 \cdot 10^8 \mathrm{s}^{-1}$	$7.3 \cdot 10^8$ / $6.9 \cdot 10^8 \mathrm{s}^{-1}$	$1.6 \cdot 10^{10}$ / $3.8 \cdot 10^9 \mathrm{s}^{-1}$
10^5 g/cm^3	$8.0 \cdot 10^2$ / $8.6 \cdot 10^8 \mathrm{s}^{-1}$	$7.8 \cdot 10^8$ / $7.3 \cdot 10^8 \mathrm{s}^{-1}$	$1.6 \cdot 10^{10}$ / $3.8 \cdot 10^9 \mathrm{s}^{-1}$

It was found that the effects of NPIs on fusion probability were negligible ($< 10^{-6}$% increase in fusion probability) for the ^{16}O projectile and ^{188}Os target, at all temperatures and densities used in the calculations. Considering that the timescale of the fusion reactions are of the order 10^{-22} s, the effective excitation rates are too low to have an impact on the population of the excited state [139] and therefore the overall effect on fusion is weak.

7.6 Summary

In this chapter, a review of the effect of plasma on heavy-ion fusion reactions was conducted and the effects of temperature and NPIs were implemented into the CCDM model. Applying plasma temperature as an environment surrounding a system of colliding nuclei containing a low-lying excited state was found to enhance fusion, with a larger enhancement induced by higher temperature. From these findings, there is now an opportunity for these effects to be tested on Earth by preparing targets in excited states using x-ray laser fields [140]. A theoretical explanation of why the fusion probabilities are increased was provided.

To improve the theoretical study, firstly an extensive study on Coulomb effects should be conducted to probe these effects in extreme high density environments. A large project could then be started by calculating the cumulative effect of a whole range of fusion processes with low-lying collective states, in a variety of stellar environment conditions. This would improve our understanding stellar evolution and nucleosynthesis.

In terms of improving our knowledge through experiments, it has been theoretically shown that the use of x-ray free electron lasers on a solid state target can create electron holes and plasma conditions suitable for NEEC to take place [141]. An improvement on this work would be to find a nucleus with a lower first excited state, or to find an isomer with a highly deformed excited state just above the isomer energy level. Laser excitation experiments could then be conducted to investigate whether this method is viable for the purpose of understanding NPIs as a fusion cross section enhancement process in a laboratory setting.

Chapter 8

The effects of nuclear friction on heavy-ion fusion reactions

In classical mechanics, friction is often depicted as a resistance force acting in the opposite direction of motion that leads to a irreversible loss of energy, typically in the form of thermal energy. Nuclear friction is analogous to classical friction, except the energy loss mechanism is due to the irreversible flow of energy from collective to intrinsic motion [142]. Friction is relevant in various branches of nuclear physics and nuclear astrophysics, such as nuclear structure, fusion and fission [143]. The study of nuclear friction arose from the need to describe nuclear damping phenomena in the 1950's, which was then built upon when heavy-ion experiments indicated that frictional forces affected processes that occur during heavy-ion collisions, such as deep inelastic collisions (DICs), multinucleon transfer (MNT) and quasi-fission. In particular DICs were investigated since they often resulted in a large loss of energy and small mass transfer, although maximising the mass transfer as a result of these collision has been of interest to those producing superheavy nuclei [144]. The intrinsic structure is thought to be the cause of nuclear friction, and this is due to the excitation of individual nucleons to a high energy density spectrum. These excited states are called non-collective* excitations and they are difficult to model microscopically, due to the lack of information on the occupied excited states and the large number of channels that need to be accounted for. In Ko's paper [145], they provided the first, semi-classical attempt at

---

*These are also described as statistical excitations a unified description of the effects of collective and non-collective excitations on low-energy heavy-ion collisions. Ko's model introduces these collective and non-collective excitations into the framework of the coupled-channels equations, and was important for demonstrating that both of these excitation effects can be treated in DICs. In this chapter, we introduce and calculate the effects of collective and non-collective excitations on heavy-ion fusion.

Understanding the role of nuclear friction is crucial for explaining experimental results in sub-barrier heavy-ion fusion, for which theoretical models do not currently describe well. Missing weak couplings were highlighted in an experiment using ^{20}Ne + ^{90,92}Zr [146]. This projectile-target pair was chosen because the deformation parameters in ^{90,92}Zr are less prevalent than those in ^{20}Ne, and hence calculations show that the quasi-elastic barrier distributions (BDs) should be comparable in both reactions. However, the research showed a discrepancy in the results – the BDs were different and the ^{92}Zr target showed virtually no structure. After comparing inelastic, backscattered Q-value spectra between experiment and theory, it was concluded that a background of non-collective excitations must be present in ^{92}Zr, due to the two valence neutrons outside of the close $N = 50$ neutron shell. This reasoning was supported by Fig. 8.1, due to the higher density of non-collective states in ^{92}Zr compared to ^{90}Zr.

A relatively recent attempt at modelling nuclear friction was conducted by Yusa, Hagino and Rowley [147]. This method used an extension of the TISE coupled-channels equations, with the couplings to the non-collective excitations included using a random matrix model. The excitation energies and spins of the relevant Zr nuclei are known, but the deformation parameters (coupling strengths) are unknown. Hence the coupling matrix elements are estimated in the random matrix model, and they used the level density as a variable to estimate the strength of the coupling form factor. The quasi-elastic BDs inclusive of non-collective excitations were calculated to explain the discrepancy between ^{20}Ne + ^{90,92}Zr. The results were an improvement on solely coupled-channels results, although there were still discrepancies at energies below the barrier.

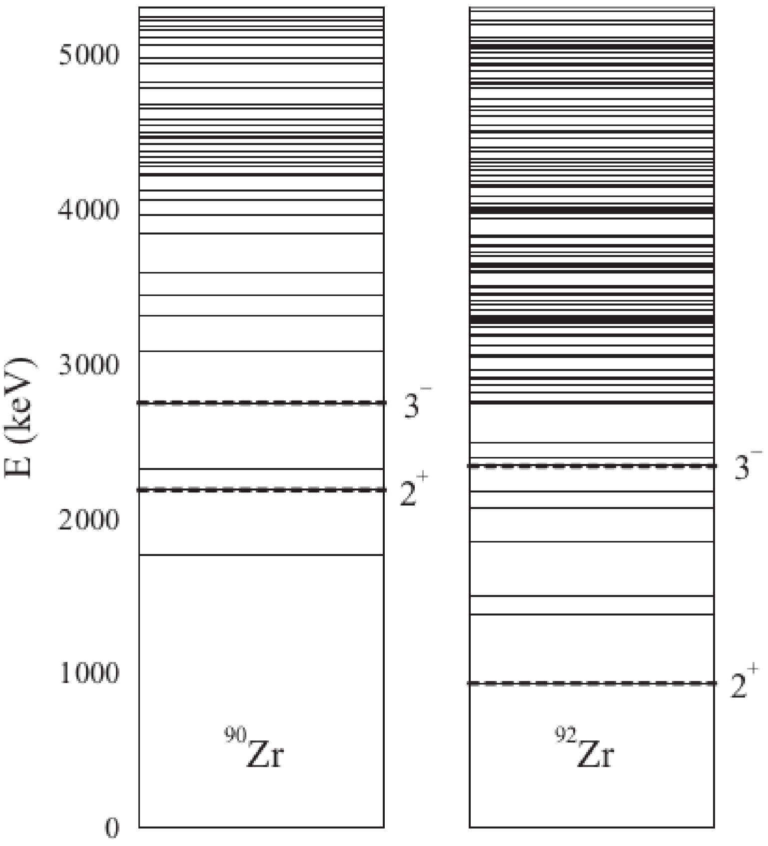

Figure 8.1: Known collective and non-collective states for ^{90,92}Zr up to 5300 keV. Figure adapted from Ref. [146].

8.1 Review of nuclear friction models

Many models testing theoretical approaches to nuclear friction have been published, including classical, quantum, fluid dynamical, and statistical models [148, 149]. This section will give a brief overview of the various models, their application to heavy-ion collisions and how the problem has evolved to the present day.

8.1.1 Classical models

The first models created to describe nuclear friction were based on classical mechanics, since this is merely the application of damped systems to nuclear collisions. Considering a system with a particle of mass m moving in one-dimensional space under the influence of a conservative force $\partial V/\partial q$ and a linear friction force $\gamma_0 m\dot{q}$,

$$m\ddot{q} + \gamma_0 m\dot{q} + \frac{\partial V}{\partial q} = 0, \tag{8.1}$$

where γ_0 is a friction co-efficient. In order to form the EOM for the system, the Lagrange equations were often chosen since it is not limited by the use of Cartesian co-ordinates and they provided a convenient way to include the frictional forces. The Lagrange equations with friction are given as,

$$\frac{d}{dt}\frac{\partial L}{\partial \dot{q}_i} - \frac{\partial L}{\partial q_i} + \frac{\partial F}{\partial \dot{q}_i} = 0, \tag{8.2}$$

where L is the Lagrangian, the generalised coordinates are q_i, and F is the Rayleigh dissipation function. The Lagrange functions are simply found in this case by identifying an integrating factor [150], $I = e^{\gamma_0 t}$, for Eq.(8.1), and hence a suitable Lagrangian is,

$$L = e^{\gamma_0 t}\left(\frac{1}{2}m\dot{q}^2 - V(q)\right). \tag{8.3}$$

Transformation to Hamiltonian mechanics, in which the velocities of the Lagrangian are replaced with momenta, first starts with identifying the total momentum,

$$p = \frac{\partial L}{\partial \dot{q}} = e^{\gamma_0 t} m\dot{q}, \tag{8.4}$$

and hence the classical Hamiltonian in one dimension is,

$$H = \dot{q}p - L = e^{-\gamma_0 t}\frac{p^2}{2m} + e^{\gamma_0 t}V(q). \tag{8.5}$$

Trajectory calculations were popular to model at the time and these initially allowed for a few friction features such as sliding friction and the dissipation of orbital angular momentum via a tangential friction force. A second tangential force named sticking-rolling friction [151] was shown to be important in some cases, although for grazing interactions it can be assumed to be negligible.

Now we can describe the frictional force in Eq.(8.2), which is formed from the sum of forces that oppose the radial motion, and this can be expressed by the Rayleigh dissipation function [152],

$$F = \frac{1}{2}\left(Z_r\dot{r}^2 + r^2 Z_t\dot{\vartheta}^2 + r^2 Z_s\dot{\varphi}^2\right), \tag{8.6}$$

where ϑ is the tangential, and φ is the rolling angle and Z_r, Z_t, Z_s are auxiliary functions of r. As stated, these equations are only applicable for linear velocity-dependent friction. For non-linear frictional forces, an extension to the Rayleigh-Lagrange formalism can be applied [153] or a general dissipation function would be required.

From here, the friction auxiliary functions were separated into scaling factor constants κ_i and form factors $f_i(r)$ that could be determined by the properties of the system,

$$Z_i(r) = \kappa_i f_i(r) \qquad\qquad i = r, t, s. \tag{8.7}$$

The form factor should then be chosen based on the type of approximation used for the collision dynamics. A ‘fast’ approximation assumes that when the nuclei interpenetrate, they do not redistribute and form a compound nucleus. This leads to a greatly increased density in the overlap region, and the frictional force is estimated using the folding integral. In this approximation, all form factors are proportional to the overlap volume. The inability to rearrange and the hard core of the nucleon-nucleon force results in the sudden nuclear potential which is repulsive. Alternatively, after the nuclei are sufficiently close or overlapping, we can assume that they are no longer separate nuclei and they form a compound nucleus. The adiabatic nuclear potential in this case will stay attractive and contribute to the formation of the compound nucleus.

It was soon discovered that these model calculations disagreed with experimental results by underestimating the energy losses by about 30%, and it was speculated that the projectile and target may not be spherical throughout the collision, as assumed in previous model calculations. Deformation degrees of freedom were soon tested in one model [154], however it was the models that used adjusted friction force parameters that were best at reproducing experimental data [155]. The friction force was found to be roughly proportional to the excitation energy and the dissipation is proportional to the square of the nuclear temperature.

An important model for this work is the Gross-Kalinowski (GK) model [57], a semi-classical model used to describe the effects of friction in heavy-ion reactions. It is semi-classical because the radial motion is treated classically, but the intrinsic system is treated with quantum mechanics, and governed by the TDSE. The TDSE was solved for a sum of single particle equations relating to the single particle wave functions. Gross and Kalinowski initially used friction form factors of Woods-Saxon shape, but found that form factors proportional to the square of the derivative of the nuclear potential were better suited to both light and heavy systems, opposed to only light systems. In their model, angular momentum is restricted to only dissipate into the intrinsic structure instead of spins by ignoring the spins of the reaction nuclei about their axes. Additionally, an incoming trajectory can lead to fusion if it is trapped in the potential pocket, or it can leave the range of the nuclear and friction forces ($r \approx 2.5R_0$). The final energy and angular momentum determine the parameters of the final trajectories, which were then plotted against the scattering angle and compared to experimental results.

8.1.2 Quantum models

In classical models, fusion reactions and deep inelastic heavy-ion collisions are well-described when the incident energy is higher than the Coulomb barrier. When the incident energy is near or below the barrier, the agreement is less clear. This is due to quantum tunneling, and this is the primary reason for why quantum mechanical treatment of the problem is necessary in these conditions.

For these models, the TDSE must be used if the considered frictional force is dependent on velocity. Starting with the classical equation of motion in Eq.(8.1) and substituting $p = m\dot{q}$, the energy is defined as,

$$E = T + V = p^2/2m + V(q), \tag{8.8}$$

and the time derivative,

$$\frac{dE}{dt} = \frac{\gamma_0}{m} p^2. \tag{8.9}$$

In a recent attempt by Tokieda and Hagino [156] to quantify the effects of friction on quantum tunneling, three friction models were applied to a one-dimensional tunneling problem. In the Caldirola-Kanai model, they quantise the classical Hamiltonian in Eq.(8.5),

$$\frac{d}{dt}\langle p \rangle + \gamma_0 \langle p \rangle + \langle \frac{\partial V}{\partial q} \rangle = 0, \tag{8.10}$$

where the expectation values are evaluated as such in Eq.(2.3) and p is as defined in Eq.(8.4). The momentum operator in this formalisation is explicitly time-dependent. The energy dissipation reads,

$$\frac{d}{dt}\langle E \rangle = -\frac{\gamma_0}{m}\langle p^2 \rangle, \tag{8.11}$$

where these quantum variables obey Ehrenfest's theorem in the classical limit. An alternative method is to use a non-linear Schrödinger equation with a Hamiltonian containing a quantum friction potential, W,

$$H = \frac{p^2}{2m} + V(q) + \gamma_0 W, \tag{8.12}$$

and here the momentum operator is time independent. This is the method used in the Kostin and Albrecht models [157, 158]. The difference arises in the way the nonlinear potential is defined. Firstly in the Kostin model,

$$W_K = \frac{\hbar}{2i}\left(\ln\frac{\psi}{\psi*} - \left\langle \frac{\psi}{\psi*} \right\rangle\right), \tag{8.13}$$

and then in the Albrecht model,

$$W_A = \langle p \rangle (q - \langle q \rangle). \tag{8.14}$$

To obtain energy-resolved tunneling probabilities, Tokieda and Hagino broaden the spatial distribution of a Gaussian wave packet until the energy distribution is sufficiently narrow and integrate the TDSE to calculate the tunneling probabilities, $T_{wp}(E_i)$. These models are able to produce a reasonable agreement with exact, frictionless tunneling probability calculations down to 10^{-4}. It was found that the linearity of the Caldirola-Kanai equations allowed for more accurate integration than those of Kostin and Albrecht. The friction coefficient strengths were chosen to coincide with weak (5 MeV) or strong (30 MeV) energy loss. Regardless, the three models led to very similar results for their approximation of weak and strong friction, and showed reduced tunneling probability for both, with the latter reducing tunneling probability more greatly.

8.1.3 Non phenomenological models

Naturally there have been attempts to describe nuclear friction without the influence of experimental results, since the predictive power of phenomenological models can be limited [142]. However, the results from these models have been limited and have had less success than the phenomenological models mentioned in the previous section. For completeness, these non phenomenological models are briefly discussed and their strengths and weaknesses highlighted.

A simple relation can be made between nuclear friction and fluid dynamics, since it is thought that under certain extreme conditions nuclei can behave as a strongly interacting fluid [159]. These were based upon the liquid drop model and modified to include viscosity. The complication arises when examining the conditions for fluid dynamics to be applicable, that is the assumption that the mean free path of a nucleon in a nucleus is shorter than the radius of the nucleus, $\ell \ll R_0$. This contradicts the assumptions from the shell model and Fermi gas model. Nevertheless, the fluid dynamics can be described by the Navier-Stokes equation and the inclusion of viscosity is useful when dealing with small oscillations for the purpose of modelling fission. However, heavy-ion dynamics cannot be described well, with some of the key problems being that the transition between two individual nuclei and a compound nucleus during fusion is not necessarily continuous, and high angular momentum is only treatable if the assumption of axially symmetric flow is relaxed.

Statistical models propose the opposite approach in that the Fermi gas model is applied, and implies that the the mean free path is larger than the radius $\ell \gg R_0$ [160]. In the piston model, the dynamics are determined by the collisions of particles with a moving wall that can be thought of as the collective coordinate. In a simple model, a few assumptions are made to simplify the calculations, such as the collisions of the nuclei with the piston being instantaneous so acceleration is ignored and the time between collisions is large compared to the period of the piston. In the gas-kinetic models, these consider the exchange of momentum through either an area of contact or the overlapping volume between the two colliding nuclei. Both of these have their disadvantages in that the former is not useful for describing radial motion due to lack of Galilean invariance and latter suffers from the assumption that the projectile and target are distinguishable.

8.2 Implementation of nuclear friction in the CCDM model

The theory behind this work is based on the semi-classical model developed by Gross and Kalinowski [57]. We chose to base our model calculations on the GK model due to the simple form of the friction form factor and parameters. The GK model used a form factor to mimic the effects of friction, the parameters of which were empirically determined from experimental results. We introduce similar friction form factors into the CCDM model and calculate the effects of friction on fusion probability by implementing friction as an environment within an open quantum system. Additionally, our model shares similar limitations to the GK model and the main improvement in this work is the quantal treatment of the radial motion along with coupled-channels effects, and hence this is a dynamical quantum mechanical model solution to nuclear friction.

There were many challenges to overcome when including friction into the CCDM model. At first, the friction form factor was included using an auxiliary state outside of the reduced system, similar to that of the fusion auxiliary state (see Fig. 8.2). The friction form factor absorbed the probabilities of the wave packet as intended. However, our method of calculating the energy-resolved fusion probabilities involves using the reflected wave packet to calculate the difference in the initial and final wave packets. As a result the absorption to any single potential could not be isolated and the energy-resolved fusion probabilities were overestimated, since these calculations included the absorption to both the friction and fusion auxiliary states. To fix this issue, the easiest and most logical option was to include the friction environment within the reduced system. In this approach, the friction auxiliary state is propagated along the radial co-ordinate axis and is governed by the EOM of the CCDM method. This state is populated due to the coupling of the projectile and target nuclei to the friction auxiliary state, and this is visually represented in Fig.8.3. The strength of this coupling is determined using Eq.(8.15) and this is the friction form factor shown in Fig.8.2. Additionally, the couplings from the explicitly treated collective states of the ions to the friction auxiliary state are irreversible.

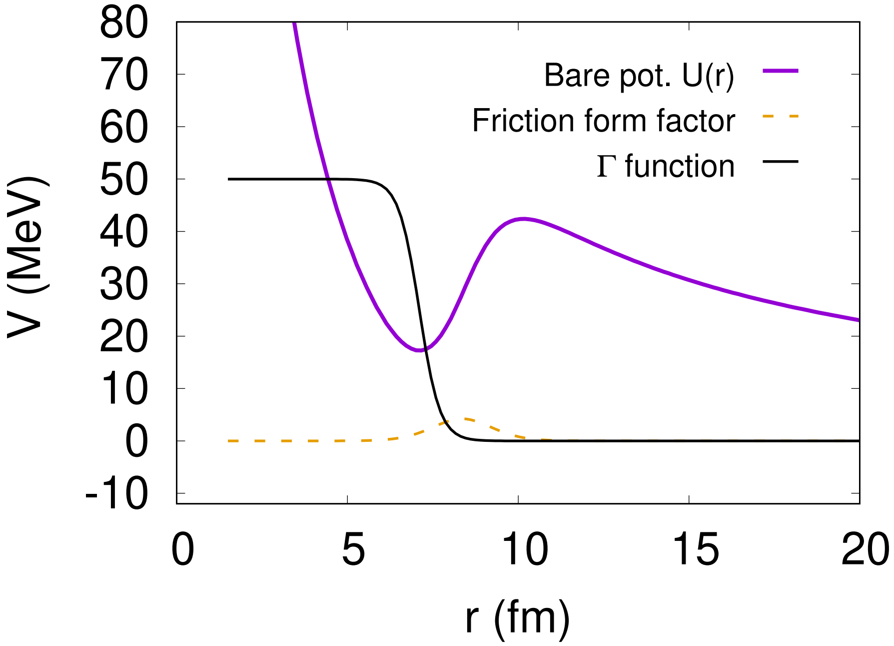

Figure 8.2: The radial position and strength of the implemented friction form factor (orange dashed line). The couplings to the radial wave packet are included in the same manner as the Γ function (fusion environment form factor, black line).

Instead of the bare potential, the friction auxiliary state interacts with a total potential with a barrier height consistent with the GK model (Fig. 8.4). Finally, once the propagation has reached an asymptotic time, the friction auxiliary state is included in the energy filtering method and the correct fusion probability can be obtained. In terms of the underlying physics, this is valid since it is likely that friction occurs at a close distance and then once energy has been dissipated, the elements excited to the high-lying non-collective states would move away from the interaction region.

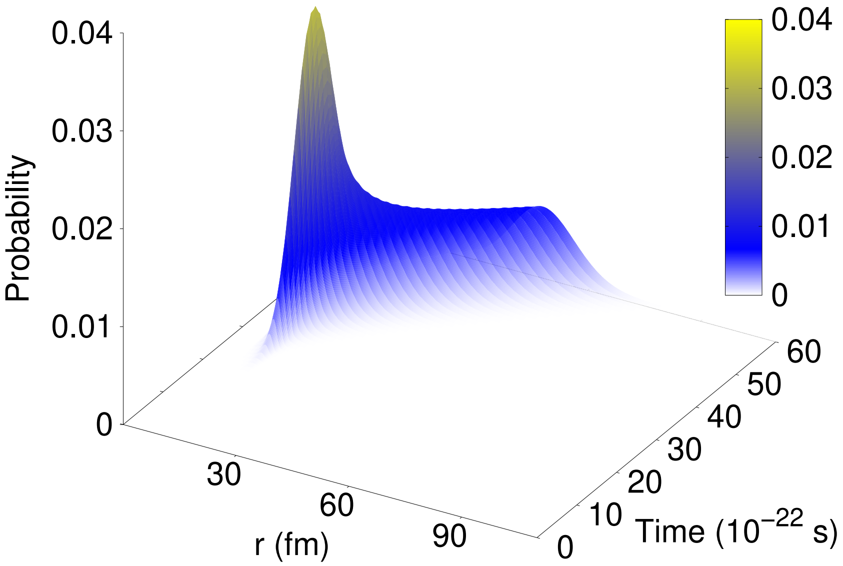

Figure 8.3: The population of the friction auxiliary state as a function of time and radial position. The state is virtually unpopulated until the reduced system wave packet reaches a radial position where the coupling to the friction auxiliary state is significant.

8.2.1 Choice of target and projectile

The choice of the ^{92}Zr target is due to the previously mentioned discrepancy between a ^{90}Zr and ^{92}Zr target. Instead a ^{16}O projectile will be used due to it being inert, and we consider the structure of ^{92}Zr. The excited state parameters used for the following calculations are given in Table 8.1. By coupling the elastic and inelastic channels to the friction environment, the impact on fusion probability can be calculated.

Table 8.1: The excited state parameters for the two considered excited states of ^{92}Zr [161].

Spin Parity	Excited state energy (MeV)	β
2^+	0.93	0.103
3^-	2.34	0.170

8.2.2 Parameters, form factors and potentials

The model parameters for the calculations in this chapter are the same as those in Section 6.3.1, except $k_{env} = 2$ and the number of states $i = 3$. The Woods-Saxon parameters required for the ^{16}O + ^{92}Zr collision are given in Table 8.2.

Table 8.2: The Woods-Saxon parameters used for the numerical calculations for the ^{16}O + ^{92}Zr collision.

Parameter	Value	Description
V_{WS}	-54.2 MeV	Woods-Saxon potential well depth
r_{WS}	1.188 fm	Woods-Saxon nuclear radius empirical constant
a_{WS}	0.63 fm	Woods-Saxon diffuseness parameter

To model the friction form factor, the procedure used in Ref. [57] was followed. Here the friction co-efficient, K_r, was determined with two forms, firstly with a Fermi function and then secondly with a form that is proportional to the square of the nuclear force. The latter is used in this work, due to it being much better at describing a wider range of heavy ion collisions,

$$K_r = K_r^0 (\nabla V_N)^2 \tag{8.15}$$

where the friction free-parameter is phenomenologically determined from experiments, and is given as $K_r^0 = 4 \cdot 10^{-23}$ s / MeV [57]. In terms of choosing the potentials to model friction, we began by using the same potential as the GK model which was a single folding nuclear potential,

$$V_{12}(r) = \int v_{12}(r - r')\rho_1(r')d^3r', \tag{8.16}$$

where v_{12} is the nucleon-nucleus interaction between a nucleon in the projectile with a target nucleus, and ρ_1 is the nucleon density distribution of the projectile, and this can be made symmetric by taking $V_N = \frac{1}{2}(V_{12} + V_{21})$. The parametrised form used by Gross and Kalinowski was,

$$V_{N_{SF}} = -\sum_{n=1}^{5} A_n (r - R)^{n-1} \ln\left[1 + \exp\left(-\frac{r - R}{a}\right)\right], \tag{8.17}$$

where $R = r_0(A_P^{1/3} + A_T^{1/3})$, a and r_0 are fixed nuclear constants, and A_n are fitting coefficients that are chosen give the best fit to the folding potential. A good approximation for these coefficients that was found to be independent of the projectile and target system was $A_1 = 33, A_2 = 2, A_3 = 3, A_4 = A_5 = 0$ [57].

When using this potential in our model, there was no potential pocket in the bare central potential and at very short distances it was not repulsive, as shown in Fig.8.4. In response to this, we instead used a Woods-Saxon nuclear potential and re-scaled the WS parameters so that the friction potential barrier height was consistent with the single folding potential. The rescaled Woods-Saxon parameters required to calculate the friction form factor in Eq.(8.15) are given in Table 8.3.

Furthermore, a proportionality coefficient, η was introduced to Eq.(8.15), and this connects the friction coefficient with a transition probability rate from the explicitly treated elastic and inelastic channels to the friction auxiliary state. Including η leads to a friction form factor that has transition probability rates of the same order as the fusion auxiliary state. In this work, $\eta = 0.04$ fm$^2/s$, and these units are used since it also gives the correct units of MeV for K_r. It is kept constant throughout the dynamics, similarly to calculations performed in literature. Further discussion on the possibility of informed dynamical proportionality coefficients are discussed in Section 8.4.

Table 8.3: The Woods-Saxon parameters used to calculate the friction form factor for the ^{16}O + ^{92}Zr collision.

Parameter	Value	Description
$V_{\rm WS}$	-55.20 MeV	Woods-Saxon potential well depth
$r_{\rm WS}$	1.188 fm	Woods-Saxon nuclear radius empirical constant
$a_{\rm WS}$	0.848 fm	Woods-Saxon diffuseness parameter

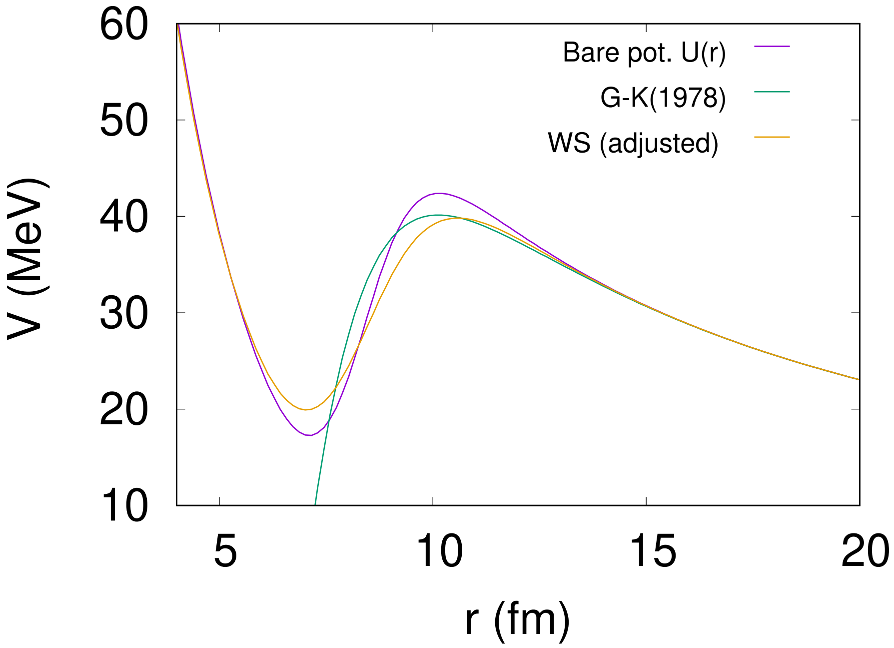

Figure 8.4: The bare potential of the ^{16}O + ^{92}Zr collision compared to the central potential created using the Gross-Kalinowski (GK) nuclear potential and an adjusted Woods-Saxon (WS) nuclear potential that replicates the same Coulomb barrier shape as the GK potential.

8.2.3 Assumptions for friction model calculations

Assumptions must be made for the nuclear friction calculations due to the shear quantity of processes that happen during a nuclear collision. Even today, a comprehensive microscopic theory for nuclear friction in heavy-ion collisions has not been published. By reducing the number of effects within the model, reasonable computational times can be achieved.

In this study, we solely focus on radial friction due to the utilisation of head-on collisions, allowing us to maintain manageable calculation run times by excluding angular momentum considerations. This is justified as the radial friction is considered the main source of energy loss, whereas tangential friction describes the loss of angular momentum and a lesser amount of energy loss ($K_\vartheta = 0.025\, K_r$). Angular momentum is conserved when tangential friction is not considered. This is consistent with the GK model as it inherently considers $Z_r \gg Z_t$ [57]. The calculations are Markovian, and it is assumed that the couplings to the non-collective states are irreversible. Therefore, the transfer of probability from the reduced system to the friction environment is not reversible, and the friction form factors do not vary based on previous time steps.

Lastly, a choice needs to be made for whether friction is considered strong or weak. When friction is strong, the interaction is instantaneous and energy is dissipated immediately when entering the region where friction takes place. If friction is weak, then a nucleus with small angular momentum within the fusion pocket would not lose all of its energy and the fusion cross sections would be altered, as only a window of angular momentum values would contribute to the fusion cross section. Weak friction is difficult to include due to the requirement of additional details about the nuclear potential of intersecting nuclei, which would require more intricate calculations such as using TDHF methods. Since there has been no indication in experiments that friction is weak or strong, the strong friction assumption is used as additional models are not required to calculate complex nuclear potentials.

8.3 The effects of nuclear friction on fusion probability for ^{16}O + ^{92}Zr

The fusion probabilities with friction are compared to the frictionless calculations as a ratio in Fig. 8.5. This figure was created by using the CCDM model with projectile and target parameters as stated in Section 8.2.2 for the ^{16}O + ^{92}Zr collision using a Coulomb wave packet. To obtain results with reasonable error, a range of initial E_0 are used, with the average change in fusion probability of low (34 – 36 MeV), medium (37 – 39 MeV) and high (40 – 45 MeV) plotted. Averaging results around the same E_0 values reduces the number of data points that are unphysical and improves the statistical error.

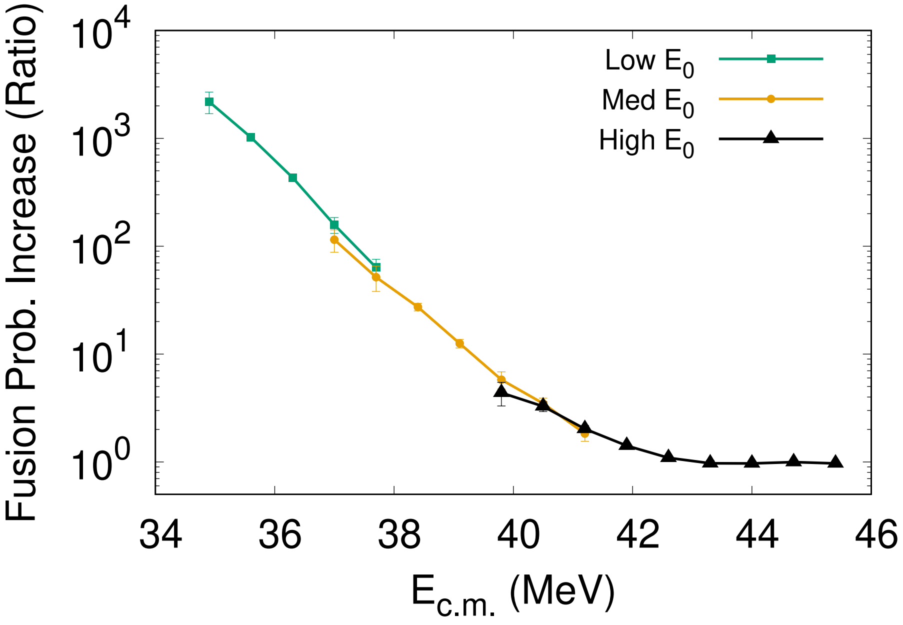

Figure 8.5: Fusion probability calculations using ^{16}O + ^{92}Zr when including the friction environment compared to the fusion calculations without friction. The height of the nominal Coulomb barrier is 42.4 MeV. The figure represents the change in fusion probability as a ratio, and uses sets of initial parameters to ensure soundness of the energy-resolved fusion probabilities for each value of E_0. The low, medium and high sets include initial E_0 values of 34 – 36, 37 – 39 and 40 – 45 MeV respectively.

The results show that fusion probability is increased by a few orders of magnitude for deep-sub barrier energies, and the ratio decreases exponentially (linearly in log scale) as E_0 approaches the Coulomb barrier. Above the barrier, the ratio is stable at values just above unity. The effects of friction on fusion probability are still unknown, with some models predicting both increased and decreased transmission through a barrier [143,162]. Here the large increase due to friction could be due to a number of factors. Firstly, the Coulomb barrier observed by the friction auxiliary state is lower than the Coulomb barrier in the entrance channel, and where there is coupling to the friction auxiliary state, it is easier for fusion to occur due to the lower potential barrier. Another reason for increased fusion probability could be the location of the friction form factor. The location of the friction form factor in shown in Fig. 8.2. It is localised very close to the fusion pocket and therefore the coupling between the friction environment and the fusion environment will be strong. This leads to significant transfer of probability from the friction auxiliary state to the fusion auxiliary state and as a result, fusion is enhanced compared to calculations without friction.

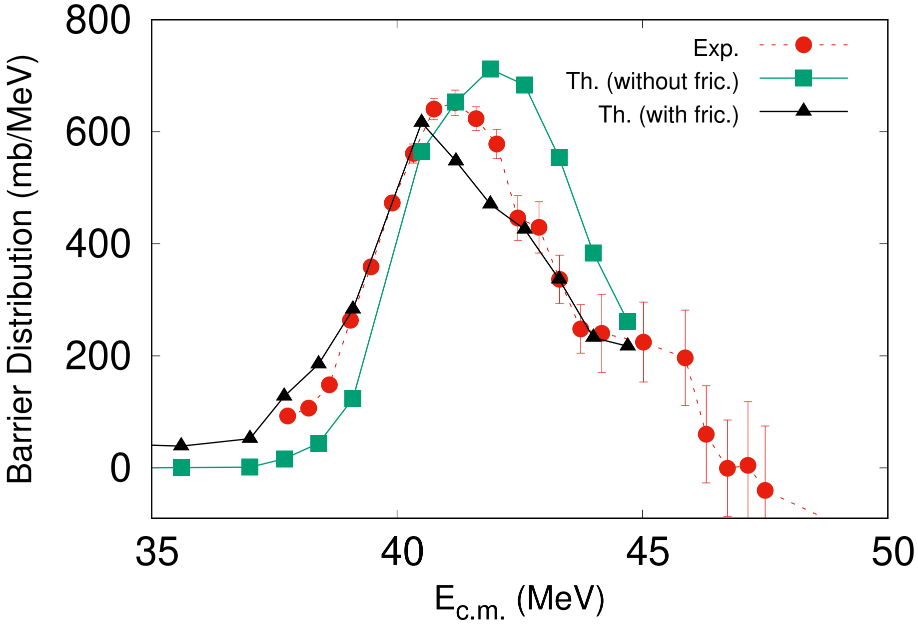

Figure 8.6: The theoretical and experimental BDs for ^{16}O + ^{92}Zr. The calculated theoretical values with friction (black triangles) are an improvement on the same calculations without friction (green squares). The experimental data is taken from Ref. [161].

In order to compare the fusion probability values calculated using the CCDM method with experimental cross sections, it was found that a useful quantity is the second energy derivative of $E\sigma$ [163]. This is called the barrier distribution (BD), and it was found that the first derivative of the transmission probability is related to the BD by the following relation [11],

$$\frac{dT_0(E)}{dE} \approx \frac{1}{\pi R_{CB}^2} \frac{d^2}{dE^2}[E\sigma(E)], \tag{8.18}$$

where $R_{CB} = 10.2$ fm is the radius of the nominal Coulomb barrier for ^{16}O + ^{92}Zr. The LHS of this equation is calculated from the theoretical fusion probability values using a two-point central difference approximation. The second derivative on the RHS is calculated using a three-point central difference approximation from experimental data [161]. The energy step used for these approximations was 1.7 MeV.

The theoretical values with and without friction are plotted together with the experimental data in Fig. 8.6. In general, the theoretical values that include friction effects fit the experimental data better than theoretical values without friction. There are some areas that diverge from the experimental values, around 38 MeV and 41 MeV, and it is hypothesised that too little probability is transferred well-below the Coulomb barrier and too much is transferred near the barrier. A solution to the discrepancy could be an adjustment to the strength or position of the friction form factor. We can further deduce information from two key features of the calculated friction BD. The first is the height of the BD, which is lower than the frictionless BD and provides agreement with the increased fusion probability values. Secondly, the width of the BD decreases when friction is present. This decrease in width could be perceived as the calculations becoming more classical, since classical BDs are essentially a combination of one or more Dirac delta functions, whereas quantum mechanically, these are broader, containing a superposition of bell-shaped functions, owing to the quantum tunneling effect [11].

Whether or not the increase in Fig. 8.5 is realistic is open to debate since details about the scaling of the friction form factor are unknown. Regardless, the implementation of friction in this model indicates that friction causes an increase in fusion probability for $J = 0$ calculations. Furthermore, information about the non-collective excited states is contained purely in the friction form factor. Something that may need to be considered is that the excited states of the non-collective excitations may not fit the approximation that compound nucleus formation occurs immediately when the wave packet is localised in the fusion pocket of the Coulomb barrier. It is possible that nuclei in non-collective states are able to escape the fusion pocket, and other reaction outcomes such as those in Fig.1.2 could occur.

8.4 Summary

We have implemented nuclear friction as an environment as part of an open quantum system within the CCDM model. The inclusion and calculation of collective and non-collective excitations on heavy-ion collisions using coupled-channel equations is an advancement on the work by Ko [145]. Nuclear friction effects on fusion probability are demonstrated using a friction auxiliary environment similar to the fusion environment that was examined in Ref. [54]. It was found that calculations with friction caused a significant increase in the fusion probability for below-barrier energies. The barrier distributions for the theoretical and experimental data were compared, and the calculations that include friction showed a better agreement with experimental data than frictionless calculations.

Despite this progress, there is still a lot of work to do to improve the description of friction in heavy-ion collisions. Currently, a phenomenological friction coefficient is used along with a proportionality coefficient with units of fm^2/s. The next steps to improve on our calculations would be the introduction of techniques that model the neck formation of fusing nuclei. TDHF calculations are a prime example of a viable method that could be used to determine parameters of neck formation, which would then inform the construction of a dynamic friction proportionality coefficient. Additionally, mass and charge transfer could be included by modelling a mass and charge diffusion form factor as an environment that is a function of the contact time between the colliding nuclei. The diffusion potential would be based on the couplings to diffusion equations [164]. It is then simple to include this diffusion form factor as an auxiliary state in the CCDM model and couple to this potential via a coupling matrix. Adjusting the position of the friction form factor is another method that could help bridge the differences between theoretical and experimental data. With further work, these improvements can be made and validated, and it is hoped that the CCDM model could be used to study the effects of nuclear friction on other reaction processes.

Chapter 9

Summary, conclusions and outlook

This chapter starts with a full overview of the thesis, followed by concluding remarks and avenues of further work that may be promising as a result of this research.

9.1 Thesis summary

The contribution of this thesis includes the development of the CCDM method and explores its uses to further our understanding of low-energy heavy-ion fusion reactions. Relevant theoretical background were discussed such as density matrix and open quantum system theory since these concepts were fundamental to this work. Numerical methods and the use of the chosen methods such as Faber polynomials for numerical integration were discussed. This was due to the equations of motion being too complex to solve using exact methods. Fourier transforms for the action of the kinetic energy operator on the density matrix were explained and compared to techniques in literature.

An overview of the CCDM method, details of the time propagation dynamics and the process of including an open quantum systems approach into the model were provided and discussed. This was followed by an introduction to the window operator and its purpose for producing energy-resolved fusion probabilities. Before introducing novel effects, the CCDM method was tested to ensure the validity of the results compared to those of literature. After adjusting the model parameters, the energy-resolved fusion probabilities agreed with TISE calculations up to 10^{-8} for the ^{16}O + ^{144}Sm collision using a Gaussian wave packet. Hence the application of the window operator to a density matrix was successful and this was a key stepping stone that allowed further research to ensue. This method had the added benefit of being able to calculate quantum observables such as entropy, energy dissipation and purity, which allowed for verification that the model was performing as expected and additional insights that classical and semi-classical models cannot provide. Furthermore, the wave packet could be visualised at each time step of the calculation, providing valuable information about the dynamics throughout the time propagation. This work was peer-reviewed and published in Physics Letters B, see Ref. [54]

Next, an investigation into the effects of plasmas on low-energy heavy-ion fusion was conducted, since there was a lack of literature discussing the effects of external environments on these reactions. This involved a review into the potential effects that plasma could have on these fusion reactions, in which electron screening, thermal effects and NPIs were discussed. It was found that fusion reactions that are initiated in hot environments (where the plasma temperature is of the order of the first excited state energy) are enhanced when low-lying excited states are present. These results were obtained from the ^{16}O + ^{188}Os collision, and this work was peer-reviewed and published in Physical Review C, see Ref. [55]. Further research on the effect of electron shielding, which is expected to be significant at high densities, is required to understand the full extent of plasma effects on heavy-ion fusion. Nuclear-plasma interactions would benefit from further studies using a target with a lower first excited state, of the order of keV. In addition, the use of x-ray free electron lasers on solid state targets could be a good approach to exploring these effects experimentally.

Finally, a study on nuclear friction was conducted, which started with a review of relevant nuclear models that have been used to estimate the effects of nuclear friction. In this work, nuclear friction was implemented as an environment as part of an open quantum system within the CCDM model. To do this, the method used within the Gross-Kalinowski model to calculate nuclear friction was implemented into the CCDM model as a friction auxiliary environment similar to the fusion environment that was examined in Ref. [54]. The inclusion and calculation of collective and non-collective excitations on heavy-ion collisions using coupled-channel equations is an advancement on the work by Ko [145]. Using the CCDM model allowed for the fully quantum mechanical treatment of nuclear friction, in addition to including quantum coherence effects of the coupled-channels. The ^{16}O + ^{92}Zr collision was used for this study, and the results showed that friction increased the fusion probabilities until $E_{c.m}$ reaches the nominal Coulomb barrier. A comparison between theory and experiment was conducted by creating barrier distributions, and the theoretical results including friction were found to be an improvement on frictionless calculations.

9.2 Concluding remarks

The primary aim of this thesis was to extend our theoretical knowledge of low-energy heavy-ion fusion reactions. To do this, the idea was to take an existing fully quantum model, the coupled-channels density matrix, and make improvements to the model which would allow for research into plasma and nuclear friction effects on low-energy heavy-ion fusion reactions. Much of the early work focused on improving the speed of calculations and making use of parallelisation, to ensure that testing the model would be efficient and that any future calculations would be done in a reasonable time. The addition of the window operator for energy-resolution purposes was a key milestone that allowed for the novel plasma and nuclear friction effects to be calculated. The model verification was successful and found that the CCDM method was able to produce results that matched experimentally-benchmarked code. In terms of code improvements, further incremental changes could be done to improve the convergence of the fusion probability results at deep sub-barrier energies.

Of the three plasma effects, temperature was shown to be prominent when using an ideal projectile and target pair (^{16}O + ^{188}Os) and has potential to be significant in astrophysical environments. This was good evidence that heavy-ion fusion reactions are affected by temperature, and environmental effects may be important for certain reactions. From the research into plasma effects, the contributions from electron screening were not significant in this study, but it is acknowledged that electron screening can quickly become significant under the right conditions (low temperature and high density). Additionally, although nuclear plasma interactions did not make significant changes to the fusion probability when their effects were included in the CCDM model, the ability to include the effects of NPIs into the calculations is a significant step to introducing them if suitable conditions are found.

This chapter showed that plasma effects are non-negligible when investigating low-energy heavy-ion fusion reactions, however more research is needed to understand how much this affects the bigger picture i.e., stellar nucleosynthesis.

It was interesting to apply nuclear friction to the model, and use an open quantum systems approach with a fully quantum dynamical model to extract meaningful results. Nuclear friction was applied successfully by including an auxiliary state that was propagated within the EOM and the phenomenological approach worked well. The results from the ^{16}O + ^{92}Zr collision moderately agreed with experimental data and demonstrated an improvement over calculations that did not include any nuclear friction effects. Of course, further refinements would have improved the results, such as implementing a dynamic proportionality coefficient and adjusting the radial position of the friction form factor which would be expected to improve the theoretical barrier distributions.

Overall, the CCDM model showed great promise throughout all the calculations, with its ability to adapt being one of its greatest strengths. Implementing new effects was a challenge, but the lack of restrictions meant that creative techniques could be used to achieve the implementations neccessary. With additional resources, the model could be tested further to find out the range of projectile and target pairs that could be handled. Comparisons to a larger range of experimental results would benefit the theoretical study greatly. Once an extensive testing has been completed, the usability to new users could then be improved to make the code accessible to a wider audience.

9.3 Further work

In terms of further developments for this work, there are three promising ideas that could be explored further:

1. The inclusion of relevant orbital angular momenta to fully understand the range of effects included into the calculation. An improvement would be the implementation of an energy-shifting formula [165] that approximates the rotational energy for a given J and is used in conjunction with $J = 0$ calculations, to avoid time-consuming angular momentum calculations.

2. An investigation of thermal effects on neutron capture reactions that are of relevance for the r-process in nucleosynthesis. These occur in explosive, high temperature environments and thermal excitation of nuclear excited states may have an influence on neutron capture reaction rates.
3. Introducing the capability within the CCDM approach to include MNT reactions, since friction is expected to be relevant there. MNT reactions are promising pathways for producing new heavy and superheavy isotopes.

In addition, if astrophysically relevant nuclei are identified that contain low-lying excited states populated thermally, an exciting prospect would be to calculate fusion cross sections of these nuclei to examine if this mechanism is significant in nucleosynthesis. Ultimately, it is hoped that the research presented in this thesis inspires further fruitful research that will contribute to the understanding of heavy-ion fusion reactions and nucleosynthesis in stellar environments.

Bibliography

[1] A. S. Eddington. The Internal Constitution of the Stars. *The Scientific Monthly*, 11(4):297–303, 1920.

[2] E. Merzbacher. The Early History of Quantum Tunneling. *Physics Today*, 55(8):44–49, 2002.

[3] G. Gamow. The Quantum Theory of Nuclear Disintegration. *Nature*, 122(3082):805–806, 1928.

[4] G. Gamow. Zur Quantentheorie des Atomkernes. *Zeitschrift für Physik*, 51(3-4):204–212, 1928.

[5] E. G. Adelberger et al. Solar fusion cross sections. II. The *pp* chain and CNO cycles. *Rev. Mod. Phys.*, 83:195–245, 2011.

[6] E. M. Burbidge, G. R. Burbidge, W. A. Fowler, and F. Hoyle. Synthesis of the Elements in Stars. *Rev. Mod. Phys.*, 29:547–650, 1957.

[7] M. Wiescher, F. Käppeler, and K. Langanke. Critical reactions in contemporary nuclear astrophysics. *Annual Review of Astronomy and Astrophysics*, 50(1):165–210, 2012.

[8] G. Baur, C.A. Bertulani, and H. Rebel. Coulomb dissociation as a source of information on radiative capture processes of astrophysical interest. *Nuclear Physics A*, 458(1):188–204, 1986.

[9] C. Broggini, D. Bemmerer, A. Guglielmetti, and R. Menegazzo. LUNA: Nuclear

Astrophysics Deep Underground. *Annual Review of Nuclear and Particle Science*, 60(1):53–73, 2010.

[10] C. Spitaleri, M. La Cognata, L. Lamia, R. G. Pizzone, and A. Tumino. Astrophysics studies with the Trojan Horse Method. *The European Physical Journal A*, 55(9), 2019.

[11] A. B. Balantekin and N. Takigawa. Quantum tunneling in nuclear fusion. *Rev. Mod. Phys.*, 70:77–100, 1998.

[12] M. Dasgupta, D. J. Hinde, N. Rowley, and A. M. Stefanini. Measuring barriers to fusion. *Annual Review of Nuclear and Particle Science*, 48(1):401–461, 1998.

[13] K. Hagino and N. Takigawa. Subbarrier Fusion Reactions and Many-Particle Quantum Tunneling. *Progress of Theoretical Physics*, 128(6):1061–1106, 2012.

[14] P. Descouvemont. Nuclear Reactions of Astrophysical Interest. *Frontiers in Astronomy and Space Sciences*, 7:9, 2020.

[15] W. Reisdorf. Heavy-ion reactions close to the Coulomb barrier. *Journal of Physics G: Nuclear and Particle Physics*, 20(9):1297, 1994.

[16] R. Bass. Fusion of heavy nuclei in a classical model. *Nuclear Physics A*, 231(1):45–63, 1974.

[17] S. K. Samaddar, D. Sperber, M. Zielińska-Pfabe, M. I. Sobel, and S. I. A. Garpman. Thermal flucatuations in a classical theory with shape degrees of freedom for heavy ion collisions. *Phys. Rev. C*, 23:760–771, 1981.

[18] W.J. Swiatecki. The dynamics of the fusion of two nuclei. *Nuclear Physics A*, 376(2):275–291, 1982.

[19] P. Fröbrich and I.I. Gontchar. Langevin description of fusion, deep-inelastic collisions and heavy-ion-induced fission. *Physics Reports*, 292(3):131–237, 1998.

[20] P. Bonche, S. Koonin, and J. W. Negele. One-dimensional nuclear dynamics in the time-dependent Hartree-Fock approximation. *Phys. Rev. C*, 13:1226–1258, 1976.

[21] P. Bonche, B. Grammaticos, and S. Koonin. Three-dimensional time-dependent Hartree-Fock calculations of ^{16}O + ^{16}O and ^{40}Ca + ^{40}Ca fusion cross sections. *Phys. Rev. C*, 17:1700–1705, 1978.

[22] S. E. Koonin. The time-dependent Hartree-Fock description of heavy-ion collisions. *Progress in Particle and Nuclear Physics*, 4:283–321, 1980.

[23] J. R. Birkelund and J. R. Huizenga. Fusion Reactions Between Heavy Nuclei. *Annual Review of Nuclear and Particle Science*, 33(1):265–322, 1983.

[24] R. Vandenbosch. Angular momentum distributions in subbarrier fusion reactions. *Annual Review of Nuclear and Particle Science*, 42(1):447–481, 1992.

[25] W. Greiner, J.Y. Park, and W. Scheid. *Nuclear Molecules*. World Scientific Publishing Company, 1995.

[26] T. Tamura. Analyses of the Scattering of Nuclear Particles by Collective Nuclei in Terms of the Coupled-Channel Calculation. *Rev. Mod. Phys.*, 37:679–708, 1965.

[27] I. J. Thompson. Coupled reaction channels calculations in nuclear physics. *Computer Physics Reports*, 7(4):167–212, 1988.

[28] G. R. Satchler. *Introduction to Nuclear Reactions*. Palgrave Macmillan UK, 1990.

[29] P.M. Jacobs and U. Smilansky. Comments on the description of sub-barrier fusion in terms of dissipative tunneling. *Physics Letters B*, 127(5):313–316, 1983.

[30] O. Tanimura. Reduction of coupled equations for heavy ion reactions. *Phys. Rev. C*, 35:1600–1602, 1987.

[31] K. Hagino, N. Rowley, and A.T. Kruppa. A program for coupled-channel calculations with all order couplings for heavy-ion fusion reactions. *Computer Physics Communications*, 123(1):143 – 152, 1999.

[32] S. Mitsuoka, H. Ikezoe, K. Nishio, K. Tsuruta, S. C. Jeong, and Y. Watanabe. Barrier Distributions Derived from Quasielastic Backscattering of ^{48}Ti, ^{54}Cr, ^{56}Fe, ^{64}Ni, and ^{70}Zn Projectiles on a ^{208}Pb Target. *Phys. Rev. Lett.*, 99:182701, 2007.

[33] S.S. Ntshangase et al. Barrier distribution for a 'superheavy' nucleus–nucleus collision. *Physics Letters B*, 651(1):27–32, 2007.

[34] T. Tanaka et al. Study of Quasielastic Barrier Distributions as a Step towards the Synthesis of Superheavy Elements with Hot Fusion Reactions. *Phys. Rev. Lett.*, 124:052502, 2020.

[35] G.G. Adamian, N.V. Antonenko, W. Scheid, and V.V. Volkov. Fusion cross sections for superheavy nuclei in the dinuclear system concept. *Nuclear Physics A*, 633(3):409–420, 1998.

[36] A. Diaz-Torres. Modeling of compound nucleus formation in the fusion of heavy nuclei. *Phys. Rev. C*, 69:021603, 2004.

[37] X.J. Bao. Fusion Dynamics of Low-Energy Heavy-Ion Collisions for Production of Superheavy Nuclei. *Frontiers in Physics*, 8, 2020.

[38] T. Vockerodt and A. Diaz-Torres. Describing heavy-ion fusion with quantum coupled-channels wave-packet dynamics. *Phys. Rev. C*, 100:034606, 2019.

[39] T. Serwatka and J. C. Tremblay. Stochastic wave packet approach to nonadiabatic scattering of diatomic molecules from metals. *The Journal of Chemical Physics*, 150(18):184105, 2019.

[40] M. Nest, R. Padmanaban, and P. Saalfrank. Time-dependent approach to electronically excited states of molecules with the multiconfiguration time-dependent hartree-fock method. *The Journal of Chemical Physics*, 126(21):214106, 2007.

[41] M. Berman, R. Kosloff, and H. Tal-Ezer. Solution of the time-dependent Liouville-von Neumann equation: dissipative evolution. *Journal of Physics A: Mathematical and General*, 25(5):1283–1307, 1992.

[42] I. Kondov, U. Kleinekathöfer, and M. Schreiber. Efficiency of different numerical methods for solving Redfield equations. *The Journal of Chemical Physics*, 114(4):1497–1504, 2001.

[43] L. Pesce and P. Saalfrank. "Free" nuclear density propagation in two dimensions the coupled-channel density matrix method and its application to inelastic molecule-surface scattering. *Chemical Physics*, 219(1):43–55, 1997.

[44] L. Pesce and P. Saalfrank. The coupled channel density matrix method for open quantum systems: Formulation and application to the vibrational relaxation of molecules scattering from nonrigid surfaces. *The Journal of Chemical Physics*, 108(7):3045–3056, 1998.

[45] S. Monturet and P. Saalfrank. Role of electronic friction during the scattering of vibrationally excited nitric oxide molecules from Au(111). *Phys. Rev. B*, 82:075404, 2010.

[46] R. Kosloff. Propagation Methods for Quantum Molecular Dynamics. *Annual Review of Physical Chemistry*, 45(1):145–178, 1994.

[47] E. Davidsson and M. Kowalewski. Simulating photodissociation reactions in bad cavities with the Lindblad equation. *The Journal of Chemical Physics*, 153(23):234304, 2020.

[48] C. Scheurer and P. Saalfrank. Hydrogen transfer in vibrationally relaxing benzoic acid dimers: Time-dependent density matrix dynamics and infrared spectra. *The Journal of Chemical Physics*, 104(8):2869–2882, 1996.

[49] P. Nalbach, J. Eckel, and M. Thorwart. Quantum coherent biomolecular energy transfer with spatially correlated fluctuations. *New Journal of Physics*, 12(6):065043, 2010.

[50] A. Diaz-Torres, D. J. Hinde, M. Dasgupta, G. J. Milburn, and J. A. Tostevin. Dissipative quantum dynamics in low-energy collisions of complex nuclei. *Phys. Rev. C*, 78:064604, 2008.

[51] A. Diaz-Torres. Coupled-channels density-matrix approach to low-energy nuclear collision dynamics: A technique for quantifying quantum decoherence effects on reaction observables. *Phys. Rev. C*, 82:054617, 2010.

[52] M. Dasgupta, D. J. Hinde, A. Diaz-Torres, B. Bouriquet, Catherine I. Low, G. J. Milburn, and J. O. Newton. Beyond the Coherent Coupled Channels Description of Nuclear Fusion. *Phys. Rev. Lett.*, 99:192701, 2007.

[53] W. Huisinga, L. Pesce, R. Kosloff, and P. Saalfrank. Faber and Newton polynomial integrators for open-system density matrix propagation. *The Journal of Chemical Physics*, 110(12):5538–5547, 1999.

[54] I. Lee and A. Diaz-Torres. Coherence dynamics in low-energy nuclear fusion. *Physics Letters B*, 827:136970, 2022.

[55] I. Lee, G. Gosselin, and A. Diaz-Torres. Thermal and atomic effects on coupled-channels heavy-ion fusion. *Phys. Rev. C*, 107:054609, 2023.

[56] E. Rutherford F.R.S. LXXIX. The scattering of α and β particles by matter and the structure of the atom. *The London, Edinburgh, and Dublin Philosophical Magazine and Journal of Science*, 21(125):669–688, 1911.

[57] D.H.E. Gross and H. Kalinowski. Friction model of heavy-ion collisions. *Physics Reports*, 45(3):175–210, 1978.

[58] N. Bohr and J. A. Wheeler. The Mechanism of Nuclear Fission. *Phys. Rev.*, 56:426–450, 1939.

[59] W. Greiner. *Quantum Mechanics - An Introduction*, chapter 4. Springer Berlin Heidelberg, 2001.

[60] H.P. Breuer and F. Petruccione. *The Theory of Open Quantum Systems*, chapter 3, pages 110–125. Oxford University Press, 2002.

[61] U. Fano. Description of States in Quantum Mechanics by Density Matrix and Operator Techniques. *Rev. Mod. Phys.*, 29:74–93, 1957.

[62] U. Weiss. *Quantum Dissipative Systems*, chapter 3. Series in modern condensed matter physics. World Scientific, 1999.

[63] H.P. Breuer and F. Petruccione. *The Theory of Open Quantum Systems*, chapter 4, page 239. Oxford University Press, 2002.

[64] G. Lindblad. On the generators of quantum dynamical semigroups. *Communications in Mathematical Physics*, 48(2):119–130, 1976.

[65] V. Gorini, A. Kossakowski, and E. C. G. Sudarshan. Completely positive dynamical semigroups of N-level systems. *Journal of Mathematical Physics*, 17(5):821–825, 1976.

[66] R. Alicki. Invitation to quantum dynamical semigroups. In *Dynamics of Dissipation*, pages 239–264. Springer, 2002.

[67] A.G. Redfield. The Theory of Relaxation Processes. In *Advances in Magnetic Resonance*, volume 1 of *Advances in Magnetic and Optical Resonance*, pages 1–32. Academic Press, 1965.

[68] M. Schröder, U. Kleinekathöfer, and M. Schreiber. Calculation of absorption spectra for light-harvesting systems using non-Markovian approaches as well as modified Redfield theory. *The Journal of Chemical Physics*, 124(8):084903, 2006.

[69] T. Renger and R. A. Marcus. On the relation of protein dynamics and exciton relaxation in pigment–protein complexes: An estimation of the spectral density and a theory for the calculation of optical spectra. *The Journal of Chemical Physics*, 116(22):9997–10019, 2002.

[70] W. T. Pollard and R. A. Friesner. Solution of the redfield equation for the dissipative quantum dynamics of multilevel systems. *The Journal of Chemical Physics*, 100(7):5054–5065, 1994.

[71] A.O. Caldeira and A.J. Leggett. Path integral approach to quantum Brownian motion. *Physica A: Statistical Mechanics and its Applications*, 121(3):587–616, 1983.

[72] A. Săndulescu, H. Scutaru, and W. Scheid. Open quantum system of two coupled harmonic oscillators for application in deep inelastic heavy ion collisions. *J. Phys. A*, 20(8):2121–2131, 1987.

[73] A. Isar, A. Săndulescu, and W. Scheid. Density matrix for the damped harmonic oscillator within the Lindblad theory. *Journal of Mathematical Physics*, 34(9):3887–3900, 1993.

[74] E. Stefanescu, W. Scheid, A. Săndulescu, and W. Greiner. Cold fission as cluster decay with dissipation. *Phys. Rev. C*, 53:3014–3021, 1996.

[75] M. Genkin and W. Scheid. A two-dimensional inverse parabolic potential within the lindblad theory for application in nuclear reactions. *Journal of Physics G: Nuclear and Particle Physics*, 34(3):441, 2007.

[76] E. Stefanescu, R. J. Liotta, and A. Săndulescu. Giant resonances as collective states with dissipative coupling. *Phys. Rev. C*, 57:798–805, 1998.

[77] G.G. Adamian, N.V. Antonenko, and W. Scheid. Friction and diffusion coefficients in coordinate in nonequilibrium nuclear processes. *Nuclear Physics A*, 645(3):376–398, 1999.

[78] M. Elliott and E. Ginossar. Applications of the Fokker-Planck equation in circuit quantum electrodynamics. *Phys. Rev. A*, 94:043840, 2016.

[79] P. Brookes et al. Critical slowing down in circuit quantum electrodynamics. *Science Advances*, 7(21):eabe9492, 2021.

[80] A. Burgess and M. Florescu. Modelling non-Markovian dynamics in photonic crystals with recurrent neural networks. *Opt. Mater. Express*, 11(7):2037–2048, 2021.

[81] A. D. Godbeer, J. S. Al-Khalili, and P. D. Stevenson. Modelling proton tunnelling in the adenine–thymine base pair. *Phys. Chem. Chem. Phys.*, 17:13034–13044, 2015.

[82] M. Riesch and C. Jirauschek. Analyzing the positivity preservation of numerical methods for the Liouville-von Neumann equation. *Journal of Computational Physics*, 390:290–296, 2019.

[83] W. Verstraelen. *Gaussian Quantum Trajectories for the variational simulation of Open Quantum Systems, with Photonic applications.* PhD thesis, University of Antwerp, 2020.

[84] A. Vijay and H. Metiu. A polynomial expansion of the quantum propagator, the Green's function, and the spectral density operator. *The Journal of Chemical Physics*, 116(1):60–68, 2002.

[85] M. R. Hermann and J. A. Fleck. Split-operator spectral method for solving the time-dependent Schrödinger equation in spherical coordinates. *Phys. Rev. A*, 38:6000–6012, 1988.

[86] K. Yeter-Aydeniz, R. C. Pooser, and G. Siopsis. Practical quantum computation of chemical and nuclear energy levels using quantum imaginary time evolution and Lanczos algorithms. *npj Quantum Inf*, 6(1), 2020.

[87] H.O. Karlsson. Accelerating the convergence of the Lanczos algorithm by the use of a complex symmetric Cholesky factorization: application to correlation functions in quantum molecular dynamics. *J. Phys. B: At. Mol. Opt. Phys*, 44(20):205102, 2011.

[88] B. M. Garraway and P. L. Knight. Comparison of quantum-state diffusion and quantum-jump simulations of two-photon processes in a dissipative environment. *Phys. Rev. A*, 49:1266–1274, 1994.

[89] M. Li. Simulation of Quantum Dynamics Based on the Quantum Stochastic Differential Equation. *The Scientific World Journal*, 2013:424137, 2013.

[90] V. Karas, D. Vokrouhlický, and A. G. Polnarev. In the vicinity of a rotating black hole: a fast numerical code for computing observational effects. *Monthly Notices of the Royal Astronomical Society*, 259(3):569–575, 1992.

[91] D. Varsamis and N. Karampetakis. On a special case of the two-variable Newton interpolation polynomial. In *CCCA12*, pages 1–6, 2012.

[92] T. Gerdts and U. Manthe. A wave packet approach to the Liouville–von Neumann equation for dissipative systems. *The Journal of Chemical Physics*, 106(8):3017–3023, 1997.

[93] J. Dalibard, Y. Castin, and K. Mølmer. Wave-function approach to dissipative processes in quantum optics. *Phys. Rev. Lett.*, 68:580–583, 1992.

[94] G. Katz, D. Gelman, M. A. Ratner, and R. Kosloff. Stochastic surrogate Hamiltonian. *The Journal of Chemical Physics*, 129(3):034108, 2008.

[95] M. Berman and R. Kosloff. Time-dependent solution of the Liouville-von Neumann equation: non-dissipative evolution. *Computer Physics Communications*, 63(1):1–20, 1991.

[96] D.T. Colbert and W.H. Miller. A novel discrete variable representation for quantum mechanical reactive scattering via the S-matrix Kohn method. *The Journal of Chemical Physics*, 96(3):1982–1991, 1992.

[97] D. Baye. The Lagrange-mesh method. *Physics Reports*, 565:1–107, 2015. The Lagrange-mesh method.

[98] J.M. Jauch. *Foundations of Quantum Mechanics*, chapter 10. A-W series in advanced physics. Addison-Wesley Publishing Company, 1968.

[99] K. Blum. *Density Matrix Theory and Applications*. Springer Berlin Heidelberg, 2012.

[100] B. S. Ishkhanov and I. M. Kapitonov. Giant dipole resonance of atomic nuclei. Prediction, discovery, and research. *Physics-Uspekhi*, 64(2):141–156, 2021.

[101] F. E. Bertrand. Excitation of Giant Multipole Resonances through Inelastic Scattering. *Annual Review of Nuclear Science*, 26(1):457–509, 1976.

[102] R.A. Broglia, C.H. Dasso, and Aa. Winther. The role of the giant resonances in deep inelastic collisions between heavy ions. *Physics Letters B*, 61(2):113–116, 1976.

[103] R. A. Bertlmann, W. Grimus, and B. C. Hiesmayr. Open-quantum-system formulation of particle decay. *Phys. Rev. A*, 73:054101, 2006.

[104] M. Tokieda and K. Hagino. Time-Dependent Approaches to Open Quantum Systems. *Frontiers in Physics*, 8:8, 2020.

[105] J. Schneider and H. Wolter. Multi-dimensional tunneling description of subbarrier fusion including neck degree of freedom. *Zeitschrift für Physik A Hadrons and Nuclei*, 339:177–188, 1991.

[106] F. L. Yost, J. A. Wheeler, and G. Breit. Coulomb Wave Functions in Repulsive Fields. *Phys. Rev.*, 49:174–189, 1936.

[107] K.J. Schafer. The energy analysis of time-dependent numerical wave functions. *Computer Physics Communications*, 63(1):427–434, 1991.

[108] B. Fetić and D. B. Milošević. Numerical solution of the time-dependent Schrödinger equation for molecular hydrogen ion in linearly polarized laser field. *AIP Conference Proceedings*, 1722(1):200006, 2016.

[109] D. Younis and J. H. Eberly. Benchmark of few-level quantum theory vs ab initio numerical solutions for the strong-field Autler–Townes effect in photoionization of hydrogen. *Journal of Physics B: Atomic, Molecular and Optical Physics*, 55(16):164001, 2022.

[110] W. Gropp, E. Lusk, and A. Skjellum. *Using MPI: Portable Parallel Programming with the Message-passing Interface.* Number v.1 in Scientific and engineering computation. MIT Press, 1999.

[111] A. Diaz-Torres and M. Wiescher. Characterizing the astrophysical S factor for ^{12}C+^{12} C fusion with wave-packet dynamics. *Phys. Rev. C*, 97:055802, 2018.

[112] L.C. Chamon. The São Paulo Potential. *Nuclear Physics A*, 787(1):198–205, 2007. Proceedings of the Ninth International Conference on Nucleus-Nucleus Collisions.

[113] E.E. Salpeter. Electrons Screening and Thermonuclear Reactions. *Australian Journal of Physics*, 7:373, 1954.

[114] S. Ichimaru. Strongly coupled plasmas: high-density classical plasmas and degenerate electron liquids. *Rev. Mod. Phys.*, 54:1017–1059, 1982.

[115] B. L. Whitten, N. F. Lane, and J. C. Weisheit. Plasma-screening effects on electron-impact excitation of hydrogenic ions in dense plasmas. *Phys. Rev. A*, 29:945–952, 1984.

[116] C. E. Rolfs and W. S. Rodney. *Cauldrons in the cosmos.* Theoretical Astrophysics. University of Chicago Press, Chicago, IL, 2006.

[117] A. A. Dzhioev, A. I. Vdovin, G. Martínez-Pinedo, J. Wambach, and Ch. Stoyanov. Thermal quasiparticle random-phase approximation with Skyrme interactions and supernova neutral-current neutrino-nucleus reactions. *Phys. Rev. C*, 94:015805, 2016.

[118] A. A. Dzhioev, K. Langanke, G. Martínez-Pinedo, A. I. Vdovin, and Ch. Stoyanov. Unblocking of stellar electron capture for neutron-rich $n = 50$ nuclei at finite temperature. *Phys. Rev. C*, 101:025805, 2020.

[119] T. Rauscher. Stellar neutron capture reactions at low and high temperature. *The European Physical Journal A*, 58(11), 2022.

[120] A. Pálffy, W. Scheid, and Z. Harman. Theory of nuclear excitation by electron capture for heavy ions. *Phys. Rev. A*, 73:012715, 2006.

[121] C. J. Chiara et al. Isomer depletion as experimental evidence of nuclear excitation by electron capture. *Nature*, 554(7691):216–218, 2018.

[122] M. Morita. Nuclear Excitation by Electron Transition and Its Application to Uranium 235 Separation. *Progress of Theoretical Physics*, 49(5):1574–1586, 1973.

[123] D. L. Bleuel et al. Method for Detection of Nuclear-Plasma Interactions in a ^{134}Xe-Doped Exploding Pusher at the National Ignition Facility. *Plasma and Fusion Research*, 11:3401075–3401075, 2016.

[124] S. Helmrich, K. Spenneberg, and A. Pálffy. Coupling highly excited nuclei to the atomic shell in dense astrophysical plasmas. *Phys. Rev. C*, 90:015802, 2014.

[125] G. Gosselin. Private Communication, 2020.

[126] R. Thompson, A. Ikeda, R.K. Sheline, J.C. Cunnane, S.W. Yates, and P.J. Daly. Levels of ^{188}Os populated in the ^{189}Os(d, t)^{188}Os reaction and in the decay of 41h ^{188}Ir. *Nuclear Physics A*, 245(3):444–460, 1975.

[127] National Nuclear Data Center, information extracted from the NuDat database. `https://www.nndc.bnl.gov/nudat/`.

[128] B. Jancovici. Pair correlation function in a dense plasma and pycnonuclear reactions in stars. *Journal of Statistical Physics*, 17(5):357–370, 1977.

[129] M. Aliotta and K. Langanke. Screening Effects in Stars and in the Laboratory. *Frontiers in Physics*, 10, 2022.

[130] N. Itoh, H. Totsuji, S. Ichimaru, and H. E. Dewitt. Enhancement of thermonuclear reaction rate due to strong screening. II - Ionic mixtures. *Astrophysical Journal*, 234:1079–1084, 1979.

[131] W. A. Fowler. Experimental and theoretical nuclear astrophysics: the quest for the origin of the elements. *Rev. Mod. Phys.*, 56:149–179, 1984.

[132] W A. Fowler, G. R. Caughlan, and B. A. Zimmerman. Thermonuclear Reaction Rates. *Annual Review of Astronomy and Astrophysics*, 5(1):525–570, 1967.

[133] M. Mosconi, M. Heil, F. Käppeler, R. Plag, and A. Mengoni. Neutron physics of the Re/Os clock. II. The $(n, n^{'})$ cross section of ^{187}Os at 30 keV neutron energy. *Phys. Rev. C*, 82:015803, 2010.

[134] K. Fujii et al. Neutron physics of the Re/Os clock. III. Resonance analyses and stellar (n, γ) cross sections of ^{186,187,188}Os. *Phys. Rev. C*, 82:015804, 2010.

[135] C.H. Dasso, S. Landowne, and A. Winther. Channel-coupling effects in heavy-ion fusion reactions. *Nuclear Physics A*, 405(2):381–396, 1983.

[136] V.I. Goldanskii and V.A. Namiot. On the excitation of isomeric nuclear levels by laser radiation through inverse internal electron conversion. *Physics Letters B*, 62(4):393–394, 1976.

[137] G. D. Doolen. Nuclear Excitation Rate. *Phys. Rev. Lett.*, 40:1695–1698, 1978.

[138] G. Gosselin and P. Morel. Enhanced nuclear level decay in hot dense plasmas. *Phys. Rev. C*, 70:064603, 2004.

[139] G. Gosselin, V. Méot, and P. Morel. Modified nuclear level lifetime in hot dense plasmas. *Phys. Rev. C*, 76:044611, 2007.

[140] T. J. Bürvenich, J. Evers, and C. H. Keitel. Nuclear Quantum Optics with X-Ray Laser Pulses. *Phys. Rev. Lett.*, 96:142501, 2006.

[141] J. Gunst, Y. A. Litvinov, C. H. Keitel, and A. Pálffy. Dominant Secondary Nuclear Photoexcitation with the X-Ray Free-Electron Laser. *Phys. Rev. Lett.*, 112:082501, 2014.

[142] R. W. Hasse. Approaches to nuclear friction. *Reports on Progress in Physics*, 41(7):1027, 1978.

[143] G. G. Adamian, N. V. Antonenko, and W. Scheid. Tunneling with dissipation in open quantum systems. *Physics Letters A*, 244(6):482–488, 1998.

[144] K.E. Rehm et al. Dissipative collisions of heavy ions at energies close to the Coulomb barrier. *Nuclear Physics A*, 366(3):477–519, 1981.

[145] C. M. Ko. Unified model of deep inelastic heavy ion collisions: Collectivity and statistics. *Zeitschrift für Physik A: Atoms and Nuclei*, 286(4):405–409, 1978.

[146] E. Piasecki et al. Effects of weakly coupled channels on quasielastic barrier distributions. *Phys. Rev. C*, 80:054613, 2009.

[147] S. Yusa, K. Hagino, and N. Rowley. Quasi-elastic scattering in the ^{20}Ne+^{90,92}Zr reactions: Role of noncollective excitations. *Phys. Rev. C*, 88:054621, 2013.

[148] D. Glas and U. Mosel. Microscopic description of nuclear friction in heavy ion collisions. *Nuclear Physics A*, 264(2):268–290, 1976.

[149] P. Fröbrich and I.I. Gontchar. What are sensitive probes for nuclear friction in heavy-ion induced fission? *Nuclear Physics A*, 563(2):326–348, 1993.

[150] P. Havas. The range of application of the lagrange formalism — i. *Il Nuovo Cimento*, 5(S3):363–388, 1957.

[151] C. F. Tsang. Nuclear Collisions with Friction. *Physica Scripta*, 10(A):90, 1974.

[152] J. W. Strutt. Some General Theorems relating to Vibrations. *Proceedings of the London Mathematical Society*, s1-4(1):357–368, 1871.

[153] E. G. Virga. Rayleigh-Lagrange formalism for classical dissipative systems. *Phys. Rev. E*, 91:013203, 2015.

[154] H.H. Deubler and K. Dietrich. A classical phenomenological description of strongly damped collisions. *Nuclear Physics A*, 277(3):493–508, 1977.

[155] K. Siwek-Wilczyǹska and J. Wilczyǹski. A phenomenological model of deep-inelastic collisions between complex nuclei. *Nuclear Physics A*, 264(1):115–131, 1976.

[156] M. Tokieda and K. Hagino. Quantum tunneling with friction. *Phys. Rev. C*, 95:054604, 2017.

[157] M. D. Kostin. On the Schrödinger-Langevin Equation. *The Journal of Chemical Physics*, 57(9):3589–3591, 1972.

[158] K. Albrecht. A new class of Schrödinger operators for quantized friction. *Physics Letters B*, 56(2):127–129, 1975.

[159] G. Holzwarth and G. Eckart. Fluid-dynamical approximation for finite Fermi systems. *Nuclear Physics A*, 325(1):1–30, 1979.

[160] H. Hofmann and P. J. Siemens. On the dynamics of statistical fluctuations in heavy ion collisions. *Nuclear Physics A*, 275(2):464–486, 1977.

[161] J. O. Newton, C. R. Morton, M. Dasgupta, J. R. Leigh, J. C. Mein, D. J. Hinde, H. Timmers, and K. Hagino. Experimental barrier distributions for the fusion of ^{12}C, ^{16}O, ^{28}Si, and ^{35}Cl with ^{92}Zr and coupled-channels analyses. *Phys. Rev. C*, 64:064608, 2001.

[162] B. J. McCoy and R. G. Carbonell. Schrödinger-Langevin theory for quantum tunneling through a barrier. *Phys. Rev. A*, 29:399–400, 1984.

[163] N. Rowley, G.R. Satchler, and P.H. Stelson. On the "distribution of barriers" interpretation of heavy-ion fusion. *Physics Letters B*, 254(1):25–29, 1991.

[164] C. Ngô and H. Hofmann. Mass exchange and angular distribution in a dynamical treatment of heavy ion collisions. *Zeitschrift für Physik A Atoms and Nuclei*, 282(1):83–92, 1977.

[165] A. Diaz-Torres, G.G. Adamian, V.V. Sargsyan, and N.V. Antonenko. Energy-shifting formulae yield reliable reaction and capture probabilities. *Physics Letters B*, 739:348–351, 2014.

Appendices

A Derivation of the nondissipative Liouvillian

The nondissipative Liouvillian of a density matrix is formulated from the substitution of a unitary time-evolution operator $U(t, t_0)$ into the Schrodinger equation [60] and is defined as

$$i\hbar \frac{\partial \rho(t)}{\partial t} = \left[\hat{H}_S, \hat{\rho}(t) \right] \tag{A.1}$$

where the system Hamiltonian $\hat{H}_S$ and density operator $\hat{\rho}$ are given as

$$\begin{aligned} \hat{H}_S &= \hat{H}_1(R) + \hat{H}_0(\zeta) + V(R,\zeta) && \text{(A.2)} \\ \hat{\rho} &= \sum_{nm} |m\rangle \langle m| \, \hat{\rho} \, |n\rangle \langle n| && \text{(A.3)} \\ &= \sum_{nm} \rho_{nm} |m\rangle \langle n| \, . && \text{(A.4)} \end{aligned}$$

The system Hamiltonian is composed of the nuclear and Coulomb interactions between the two nuclei, $\hat{H}_1(R)$, the intrinsic Hamiltonian determined from the considered excited states of the target or projectile, $\hat{H}_0(\zeta)$, and the coupling potential which determines how the radial motion affects the population of excited states, $V(R, \zeta)$.

The individual components of the Hamiltonian must be calculated,

$$\left[\hat{H}_1, \hat{\rho}\right] = \sum_{mn} \left[\hat{H}_1, \hat{\rho}_{mn}\right] |m\rangle \langle n| \tag{A.5}$$

$$= \sum_{mn} \{\hat{H}_1 \hat{\rho}_{mn} - \hat{\rho}_{mn} \hat{H}_1\} |m\rangle \langle n| \tag{A.6}$$

$$\left[\hat{H}_0, \hat{\rho}\right] = \sum_{mn} \hat{\rho}_{mn} \left[\hat{H}_0, |m\rangle \langle n|\right] \tag{A.7}$$

$$= \sum_{mn} \hat{\rho}_{mn} \{\mathrm{e}_m |m\rangle \langle n| - |m\rangle \langle n| \mathrm{e}_n\} \tag{A.8}$$

$$= \sum_{mn} \hat{\rho}_{mn} (\mathrm{e}_m - \mathrm{e}_n) |m\rangle \langle n| \tag{A.9}$$

$$\left[\hat{V}, \hat{\rho}\right] = \sum_{mn} \left[\hat{V}, \hat{\rho}_{mn} |m\rangle \langle n|\right] \tag{A.10}$$

using the relation $[A, B \cdot C] = [A, B] \cdot C + B \cdot [A, C]$, this equation is expanded to

$$[A, B] \cdot C = [\hat{V}, \hat{\rho}_{mn}] = \{\hat{V} \hat{\rho}_{mn} - \hat{\rho}_{mn} \hat{V}\} |m\rangle \langle n| \tag{A.11}$$

$$B \cdot [A, C] = \hat{\rho}_{mn} [\hat{V}, |m\rangle \langle n|] = \hat{\rho}_{mn} \{\hat{V} |m\rangle \langle n| - |m\rangle \langle n| \hat{V}\}. \tag{A.12}$$

Bringing together all parts of the Hamiltonian and substituting into Eq.(A.1),

$$\sum_{mn} \left\{ i\hbar \dot{\hat{\rho}}_{mn} - \hat{H}_1 \hat{\rho}_{mn} - \hat{\rho}_{mn} \hat{H}_1 - \hat{\rho}_{mn} (\mathrm{e}_m - \mathrm{e}_n) - \hat{V} \hat{\rho}_{mn} \right\} |m\rangle \langle n|$$

$$= - \sum_{mn} \hat{\rho}_{mn} |m\rangle \langle n| \hat{V} \tag{A.13}$$

when the dot represents a partial derivative with respect to time. Then looking at the matrix element "ij", which includes the energy eigenstates,

$$i\hbar \dot{\hat{\rho}}_{ij} = \hat{\rho}_{ij} (\mathrm{e}_k - \mathrm{e}_l) + \hat{H}_1 \hat{\rho}_{ij} - \hat{\rho}_{ij} \hat{H}_1 + \sum_n \left(-\hat{\rho}_{in} \hat{V}_{nj} + \hat{V}_{in} \hat{\rho}_{nj} \right) \tag{A.14}$$

and adding in the radial basis states $|r\rangle$ and $|s\rangle$,

$$i\hbar\dot{\hat{\rho}}_{ij}^{rs} = \hat{\rho}_{ij}^{rs}(\mathrm{e}_i - \mathrm{e}_j) + \langle r|\,\hat{H}_1\hat{\rho}_{ij} - \hat{\rho}_{ij}\hat{H}_1\,|s\rangle + \sum_n \langle r|\,\hat{\rho}_{in}\hat{V}_{nj} + \hat{V}_{in}\hat{\rho}_{nj}\,|s\rangle\,. \tag{A.15}$$

Introducing a new matrix index by inserting $\sum_t |t\rangle\langle t|$ into the 2$^{\mathrm{nd}}$ and 3$^{\mathrm{rd}}$ terms on the right-hand side of Eq (A.15) is necessary for the kinetic energy matrix calculations and therefore,

$$\begin{aligned}
\text{2nd term of RHS} &= \sum_t \langle r|\,\hat{H}_1\,|t\rangle\langle t|\,\hat{\rho}_{ij}\,|s\rangle - \langle r|\,\hat{\rho}_{ij}\,|t\rangle\langle t|\,\hat{H}_1\,|s\rangle && \text{(A.16)}\\
&= \sum_t \left(H_1^{rt}\rho_{ij}^{ts} - \rho_{ij}^{rt}H_1^{ts}\right) && \text{(A.17)}\\
&= \sum_t \left(T^{rt}\rho_{ij}^{ts} - \rho_{ij}^{rt}T^{ts}\right) + \left(U^{rr}\rho_{ij}^{rs} - \rho_{ij}^{rs}U^{ss}\right) && \text{(A.18)}
\end{aligned}$$

$$\begin{aligned}
\text{3rd term of RHS} &= \sum_n\sum_t \langle r|\,\hat{\rho}_{in}\,|t\rangle\langle t|\,\hat{V}_{nj}\,|s\rangle + \langle r|\,\hat{V}_{in}\,|t\rangle\langle t|\,\hat{\rho}_{nj}\,|s\rangle && \text{(A.19)}\\
&= \sum_n\sum_t \left(V_{in}^{rt}\rho_{ij}^{ts} - \rho_{in}^{rt}V_{nj}^{ts}\right) && \text{(A.20)}\\
&= \sum_n \left(V_{in}^{rr}\rho_{nl}^{rs} - \rho_{in}^{rs}V_{nl}^{ss}\right) && \text{(A.21)}
\end{aligned}$$

where T and U are as described in Section 4.2.1. Bringing these equations together and simplifying, the nondissipative Liouvillian is given below

$$\begin{aligned}
(\hat{\mathcal{L}}_H\hat{\rho})_{ij}^{rs} = \dot{\rho}_{ij}^{rs} = -\frac{i}{\hbar}\Bigg\{\ &\rho_{ij}^{rs}\,(\mathrm{e}_i - \mathrm{e}_j) + \rho_{ij}^{rs}\,(U^{rr} - U^{ss}) + \\
&+ \sum_t \left(T^{rt}\rho_{ij}^{ts} - \rho_{ij}^{rt}\,T^{ts}\right) + \sum_n \left(V_{in}^{rr}\rho_{nj}^{rs} - \rho_{in}^{rs}V_{nj}^{ss}\right)\Bigg\}.
\end{aligned} \tag{A.22}$$

B Derivation of the dissipative Liouvillian

The dissipative part of the Liouville von-Neumann equation is given below,

$$\hat{\mathcal{L}}_D\hat{\rho} = \sum_\alpha \left(\hat{\mathcal{C}}_\alpha \, \hat{\rho} \, \hat{\mathcal{C}}_\alpha^\dagger - \frac{1}{2} \left[\hat{\mathcal{C}}_\alpha^\dagger \hat{\mathcal{C}}_\alpha, \hat{\rho} \right]_+ \right) \tag{B.1}$$

where $\hat{\mathcal{C}}_\alpha$ are Lindblad operators, with $\alpha = ij$ being the index for each of the ordered pairs (ij). This is determined using the following equation

$$\hat{\mathcal{C}}_\alpha = \sqrt{\Gamma_{ij}(r)} \, |i\rangle \, \langle j| \, . \tag{B.2}$$

As per usual, Lindblad operators are phenomenologically determined and the ones used in this study are described by the transition rates, $\sqrt{\Gamma_{ij}(r)}$, from the $|j\rangle$ states to the $|i\rangle$ states.

The dissipative Liouvillian can then be written as

$$\begin{aligned} \hat{\mathcal{L}}_D\hat{\rho} = \sum_{ij} \sqrt{\Gamma_{ij}(r)} \, |i\rangle \, \langle j| \, \hat{\rho} \, |j\rangle \, \langle i| \, \sqrt{\Gamma_{ij}(r)} \\ - \frac{1}{2} \Big(\Gamma_{ij}(r) \, |j\rangle \, \langle i|i\rangle \, \langle j| \, \hat{\rho} + \hat{\rho} \, |j\rangle \, \langle i|i\rangle \, \langle j| \, \Gamma_{ij}(r) \Big) \end{aligned} \tag{B.3}$$

and after taking the expectation value of $\hat{\rho}$ within the $|j\rangle$ basis, and removing the inner products, $\langle i|i\rangle = 1$, a simplified equation is obtained

$$\hat{\mathcal{L}}_D\hat{\rho} = \sum_{ij} \sqrt{\Gamma_{ij}(r)} \, |i\rangle \, \hat{\rho}_{jj} \, \langle i| \, \sqrt{\Gamma_{ij}(r)} - \frac{1}{2} \Big(\Gamma_{ij}(r) \, |j\rangle \, \langle j| \, \hat{\rho} + \hat{\rho} \, |j\rangle \, \langle j| \, \Gamma_{ij}(r) \Big) \tag{B.4}$$

and then looking at the elements "kl", which are the extended basis states,

$$\left(\hat{\mathcal{L}}_D\hat{\rho} \right)_{kl} = \sum_{ij} \sqrt{\Gamma_{ij}(r)} \, \delta_{ki} \, \hat{\rho}_{jj} \, \delta_{il} \sqrt{\Gamma_{ij}(r)} - \frac{1}{2} \Big(\Gamma_{ij}(r) \, \delta_{kj} \, \hat{\rho}_{jl} + \hat{\rho}_{kj} \, \delta_{jl} \, \Gamma_{ij}(r) \Big). \tag{B.5}$$

Projecting Eq.(B.5) onto the radial basis states rs, the dissipative Liouvillian is expressed as

$$(\mathcal{L}_D\hat{\rho})^{rs}_{kl} = \delta_{kl} \sum_\nu \sqrt{\Gamma^{rr}_{k\nu}} \, \rho^{rs}_{\nu\nu} \sqrt{\Gamma^{ss}_{k\nu}} - \frac{1}{2} \sum_\nu (\Gamma^{rr}_{\nu k} + \Gamma^{ss}_{\nu l}) \rho^{rs}_{kl}. \tag{B.6}$$

C Profile of CCDM code

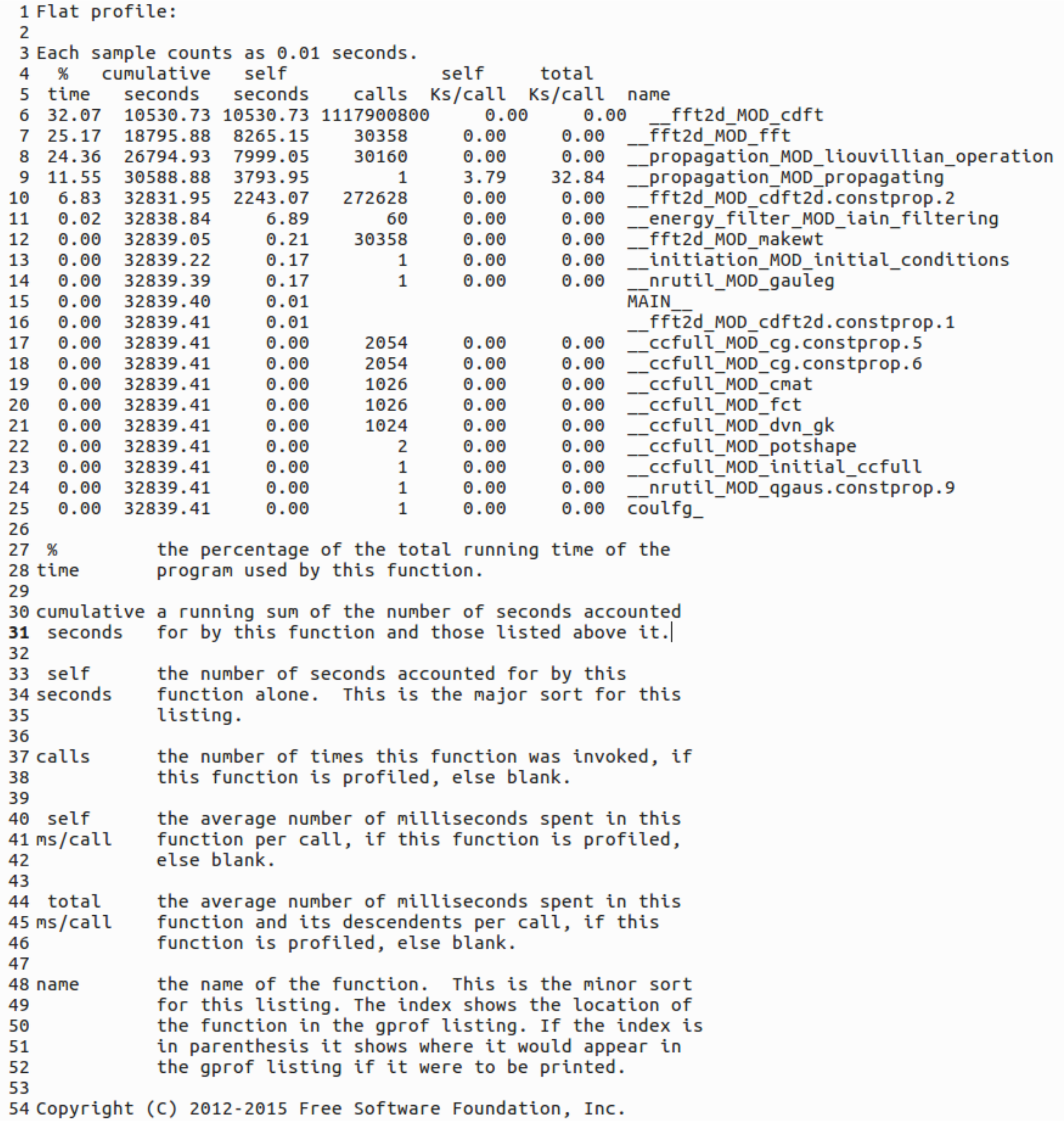

```
Flat profile:

Each sample counts as 0.01 seconds.
  %   cumulative   self              self     total
 time   seconds   seconds    calls  Ks/call  Ks/call  name
 32.07  10530.73 10530.73 1117900800     0.00     0.00  __fft2d_MOD_cdft
 25.17  18795.88  8265.15    30358     0.00     0.00  __fft2d_MOD_fft
 24.36  26794.93  7999.05    30160     0.00     0.00  __propagation_MOD_liouvillian_operation
 11.55  30588.88  3793.95        1     3.79    32.84  __propagation_MOD_propagating
  6.83  32831.95  2243.07   272628     0.00     0.00  __fft2d_MOD_cdft2d.constprop.2
  0.02  32838.84     6.89       60     0.00     0.00  __energy_filter_MOD_iain_filtering
  0.00  32839.05     0.21    30358     0.00     0.00  __fft2d_MOD_makewt
  0.00  32839.22     0.17        1     0.00     0.00  __initiation_MOD_initial_conditions
  0.00  32839.39     0.17        1     0.00     0.00  __nrutil_MOD_gauleg
  0.00  32839.40     0.01                             MAIN__
  0.00  32839.41     0.01                             __fft2d_MOD_cdft2d.constprop.1
  0.00  32839.41     0.00     2054     0.00     0.00  __ccfull_MOD_cg.constprop.5
  0.00  32839.41     0.00     2054     0.00     0.00  __ccfull_MOD_cg.constprop.6
  0.00  32839.41     0.00     1026     0.00     0.00  __ccfull_MOD_cmat
  0.00  32839.41     0.00     1026     0.00     0.00  __ccfull_MOD_fct
  0.00  32839.41     0.00     1024     0.00     0.00  __ccfull_MOD_dvn_gk
  0.00  32839.41     0.00        2     0.00     0.00  __ccfull_MOD_potshape
  0.00  32839.41     0.00        1     0.00     0.00  __ccfull_MOD_initial_ccfull
  0.00  32839.41     0.00        1     0.00     0.00  __nrutil_MOD_qgaus.constprop.9
  0.00  32839.41     0.00        1     0.00     0.00  coulfg_

 %         the percentage of the total running time of the
time       program used by this function.

cumulative a running sum of the number of seconds accounted
 seconds   for by this function and those listed above it.

 self      the number of seconds accounted for by this
seconds    function alone.  This is the major sort for this
           listing.

calls      the number of times this function was invoked, if
           this function is profiled, else blank.

 self      the average number of milliseconds spent in this
ms/call    function per call, if this function is profiled,
           else blank.

 total     the average number of milliseconds spent in this
ms/call    function and its descendents per call, if this
           function is profiled, else blank.

name       the name of the function.  This is the minor sort
           for this listing. The index shows the location of
           the function in the gprof listing. If the index is
           in parenthesis it shows where it would appear in
           the gprof listing if it were to be printed.

Copyright (C) 2012-2015 Free Software Foundation, Inc.
```

Figure 1: The profile of the CCDM code for $^{16}O + ^{144}Sm$, created using `gprof`.